ISSN 8755-6839

SCIENCE OF TSUNAMI HAZARDS

Journal of Tsunami Society International

Volume 36 Number 3 2017

REVIEW OF EARTHQUAKES AND TSUNAMI RECORDS AND CHARACTERIZATION OF CAPABLE FAULTS ON THE NORTHWESTERN COAST OF ECUADOR 100

Kervin Chunga[1]*, TheofilosToulkeridis[2]*, Xavier Vera-Grunauer[3-4], Marllelis Gutierrez[1], Nestor Cahuana[4], Alamir Alvarez[1]

[1]Universidad Estatal Península Santa Elena, Facultad de Ciencias de la Ingeniería. **ECUADOR**
[2]Universidad de las Fuerzas Armadas ESPE, Sangolquí, Quito, **ECUADOR**.
[3]Universidad Católica de Santiago de Guayaquil, Facultad de Ingeniería, **ECUADOR**.
[4]Geoestudios S.A., Guayaquil, Ecuador

THE MISSING LINK IN EL NIÑO'S PHENOMENON GENERATION 128

Fernando Mato[1]*, TheofilosToulkeridis[2]

[1] Universidad de las Fuerzas Armadas ESPE, Sangolquí, Quito, **ECUADOR**

MANIFESTATION OF THE 1963 URUP TSUNAMI ON SAKHALIN: OBSERVATIONS AND MODELING 145

Andrey Zaytsev[1,2)], Irina Kostenko[1)], Andrey Kurkin[2,3)], Efim Pelinovsky[2,4,5)] & George Pararas-Carayannis [6]

[1,]Special Research Bureau for Automation of Marine Researches, Yuzhno-Sakhalinsk, **RUSSIA**
[2] Nizhny Novgorod State Technical University n.a. R. Alekseev, Nizhny Novgorod, **RUSSIA**
[3] Institute of Space Technologies, Peoples' Friendship University of Russia (RUDN University), Moscow, **RUSSIA**
[4]Institute of Applied Physics, Nizhny Novgorod, **RUSSIA**
[5]National Research University – Higher School of Economics, Moscow, **RUSSIA**
[6]Tsunami Society International, Honolulu, Hawaii, **USA**.

COMPARISON OF METHODS FOR SIMULATING TSUNAMI RUN-UP THROUGH COASTAL FORESTS 167

Benazir[1], Radianta Triatmadja[2*], Adam Pamudji Rahardjo[2], and Nur Yuwono[2]

[1]Ph.D Student at Department of Civil and Environmental Engineering, Faculty of Engineering Universitas Gadjah Mada, **INDONESIA**
[2]Department of Civil and Environmental Engineering, Faculty of Engineering Universitas Gadjah Mada, **INDONESIA**.

WWW.TSUNAMISOCIETY.ORG

TSUNAMI SOCIETY INTERNATIONAL, 1741 Ala Moana Blvd. #70, Honolulu, HI 96815, USA.

SCIENCE OF TSUNAMI HAZARDS is a CERTIFIED OPEN ACCESS Journal included in the prestigious international academic journal database DOAJ, maintained by the University of Lund in Sweden with the support of the European Union. SCIENCE OF TSUNAMI HAZARDS is also preserved, archived and disseminated by the National Library, The Hague, NETHERLANDS, the Library of Congress, Washington D.C., USA, the Electronic Library of Los Alamos, National Laboratory, New Mexico, USA, the EBSCO Publishing databases and ELSEVIER Publishing in Amsterdam. The vast dissemination gives the journal additional global exposure and readership in 90% of the academic institutions worldwide, including nation-wide access to databases in more than 70 countries.

OBJECTIVE: Tsunami Society International publishes this interdisciplinary journal to increase and disseminate knowledge about tsunamis and their hazards.

Submit manuscripts of research papers, notes or letters to the Editor. If a research paper is accepted for publication the author(s) must submit a scan-ready manuscript, a Doc, TeX or a PDF file in the journal format. Issues of the journal are published electronically in PDF format. There is a minimal publication fee for authors who are members of Tsunami Society International for three years and slightly higher for non-members. Tsunami Society International members are notified by e-mail when a new issue is available. Permission to use figures, tables and brief excerpts from this journal in scientific and educational works is granted provided that the source is acknowledged.

Recent and all past journal issues are available at: http://www.TsunamiSociety.org CD-ROMs of past volumes may be purchased by contacting Tsunami Society International at postmaster@tsunamisociety.org Issues of the journal from 1982 thru 2005 are also available in PDF format at the U.S. Los Alamos National Laboratory Library http://epubs.lanl.gov/tsunami/

ISSN 8755-6839

SCIENCE OF **TSUNAMI HAZARDS**

Journal of Tsunami Society International

Volume 36 **Number 3** **2017**

REVIEW OF EARTHQUAKES AND TSUNAMI RECORDS AND CHARACTERIZATION OF CAPABLE FAULTS ON THE NORTHWESTERN COAST OF ECUADOR

Kervin Chunga[1]*, TheofilosToulkeridis[2]*, Xavier Vera-Grunauer[3-4], Marllelis Gutierrez[1], Nestor Cahuana[4], Alamir Alvarez[1]

[1]Universidad Estatal Península Santa Elena, Facultad de Ciencias de la Ingeniería. Ecuador
[2]Universidad de las Fuerzas Armadas ESPE, Sangolquí, Quito, Ecuador.
[3]Universidad Católica de Santiago de Guayaquil, Facultad de Ingeniería, Ecuador.
[4]Geoestudios S.A., Guayaquil, Ecuador
*Corresponding authors: kchunga@upse.edu.ec; ttoulkeridis@espe.edu.ec

ABSTRACT

There are only few documented moderate to strong earthquakes associated with active tectonics of capable crustal faults in Ecuador's northwestern coastal region. The short seismic record begins with the great earthquake and tsunami on January 31, 1906 (Mw 8.8), followed by other destructive earthquakes and tsunamis in the subduction zone, which are recorded on January 19, 1958 (Mw 7.6) and December 12, 1979 (Mw 7.7). Furthermore, modest earthquakes from capable faults have been registered on April 9, 1976 (Mw 6.7), January 2, 1981 (Mw 5.9), June 25, 1989 (Mw 6.3), April 20, 2016 (Mw 6.0) and January 31, 2017 (Mw 5.5, MLv 5.7). Earthquakes of minor magnitude have not been considered in this study, as they lack to cause coseismic ground effects. In this study, a catalog of geological fault has been delineated with 41 segments of capable and active faults on the sea floor and inland segments of Esmeraldas and Manabí provinces, as the instrumental seismic record does not provide sufficient information to evaluate the seismic risk due to faults capable of generating earthquakes larger than Mw≥6. This methodological approach allowed to estimate the seismicity levels in the order of 6.0≤Mw≤7.3 and rock peak ground accelerations in the order of 0.42g 0.26g. These values have been obtained from empirical regression equations applied to the length of capable geological faults.

The seismogenic structure of the subduction zone is able to generate earthquakes and subsequently tsunamis in the order of 8.2≤Mw≤9.0, and may cause coseismic ground damage to the close-by (82km), highly-populated city of Esmeraldas. This structural geological analysis is able to provide new insights, which need to be considered in studies of seismic hazards and particularly in the generation of control spectra for vertical as well as horizontal components from capable faults.

Keywords: Earthquake and tsunami hazard, capable fault, Ecuador’s northwestern coast.

1. INTRODUCTION

Regression equations applied to geometric and kinematic parameters of active and capable geological faults allow the estimation of maximum magnitudes (Wells and Coppersmith, 1994; Wesnousky, 2008; Leonard, 2010; Stirling et al., 2013) as well as Peak Ground Accelerations (PGA) (Fukushima and Tanaka, 1990). Empirical relationships between parameters of larger isostatic lengths of macro-seismic intensities and magnitudes have also been used to determine the seismic source (Marín et al., 2008). This methodology provides estimates of seismicity levels, particularly for areas where the history of seismic recurrence is poor or with little information. One of these tectonic areas, which is located in the eastern flank of the Pacific ring of fire is the northwestern coast of Ecuador at the border with the southwestern coast of Colombia. This area is geodynamically characterized by an active subduction zone where the Nazca oceanic plate (with a direction of N80 ° E, and a displacement velocity of 47 mm / yr) collides and subducts the continental segments of the South American and Caribbean plates (Berninghausen, 1962; Barazangi and Isacks 1976; Kanamori and McNally, 1982; De Mets et al., 1990; Nocquet et al., 2016; Trenkamp et al, 2002; Pararas-Carayannis, 2012; Toulkeridis et al., 2017) (Fig. 1).

For the continental territory of Ecuador, it has been possible to establish two main seismic sources, (1) the tectonic zone of the subduction interface, and (2) the crustal (or superficial) geological faults located within the continental segment. The main seismogenic structure, the subduction zone, which is located between 52 and 127 km away from the coastal limits of the province of Esmeraldas, is capable of generating potential earthquakes and subsequent tsunamis in the order of 7.6≤Mw≤9.0 (Fig. 2). The oblique convergence between the subducting Nazca plate with respect to the continental plate, controls in part the development, distribution and kinematics of the crustal faults (ie, Veloza et al., 2012).

In this current study, we evaluated only the crustal faults delineated in the continental segment of the provinces of Esmeraldas and northern Manabí and their extension on the continental shelf (ie, Dumont et al., 2006, Eguez et al., 2002; Michaud, 2012, Michaud et al., 2015, Migeon et al., 2016, Ratzov et al., 2012). These crustal structures have been mapped from field observations, interpretations of geological maps with a scale of 1: 100,000, topography, remote sensing images

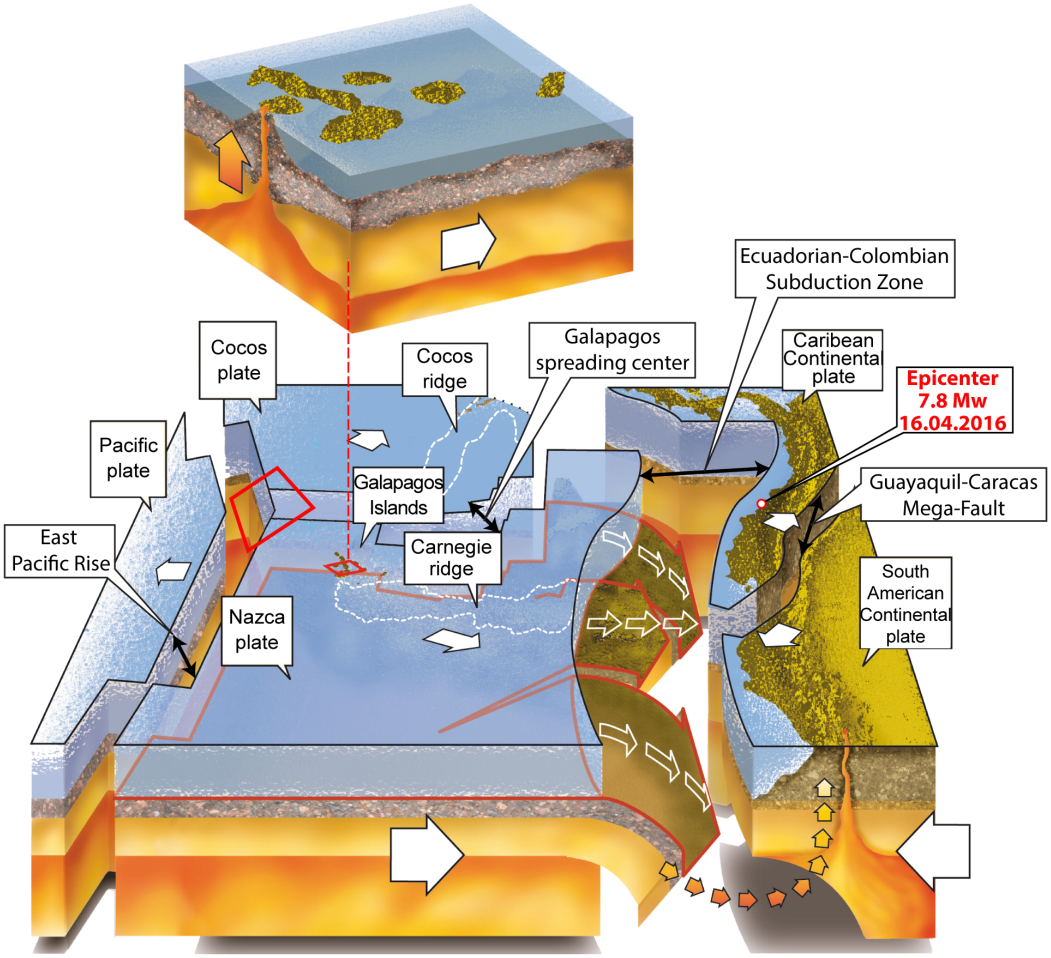

Fig. 1: Geodynamic setting of Ecuador, the Galapagos Islands and the Carnegie Ridge. Adapted from Toulkeridis, 2013 and Rodriguez et al., 2016

and spatial distribution of earthquakes from data available in the catalogs of the Instituto Geofísico of the Escuela Politécnica Nacional in Quito (IG- EPN) and the National Earthquake Information Center of the United States Geological Survey (NEIC-USGS).

The methodological procedure, from a structural geology and coastal geomorphology point of view, has been to delineate the dimensions of the geological fault lengths capable of generating earthquakes and also tsunamis with magnitudes M≥6. Smaller faults that generate earthquakes of 4≤M≤5.5 were not analyzed in this study because of their low probability of causing significant cosmic geological effects on the ground. Records of historical earthquakes associated with geological faults are poorly documented for the coast of Ecuador. However, the recent Pedernales / Muisne earthquake of April 16, 2016 (Mw 7.8) and successive aftershocks due to the seismogenic structure have generated post-seismic effects, such as activation of crustal faults, which are located between 74 and 115 km distant to the northeast of the epicenter. In the city of Esmeraldas, for the earthquake of Mw 7.8, minor damages of masonry of some houses in the urban center were reported.

Therefore, the main aim of this study has been to apply a methodology to evaluate each capable fault mapped in the territory in order to provide fundamental information of the maximum magnitude and PGA estimates, which may subsequently be applied to determine the level of seismic hazard in densely populated areas or the developing industrial sectors.

2. TECTONICS AND SUBDUCTION EARTHQUAKES OF THE STUDY AREA

Ecuador's subduction zone is approximately 576 kilometers long, but if we consider the subduction geodynamics from the northern coast of Peru reaching the southern Andean being part of the continental territory of Ecuador, then the subduction zone may be as long as 756 kilometers. The subduction interface zone is complex, but may be well distinguished in depth by the variation of the oblique convergence of the subducting Nazca plate towards the continental segment formed by the South American and Caribbean plates (Gutscher et al., 1999: Veloza et al., 2012; Toulkeridis, 2011). Other structural features that may define the areas and borders of seismogenic structures or seismotectonic divisions are the fracture zones of the oceanic crust (Kelleher, 1972; Wiens and Stein, 1983; Carena, 2011).

For the entire coast of Ecuador, three main seismogenic segments may be differentiated along the subduction zone. The first segment being the southern coast, including the Gulf of Guayaquil and the Santa Elena province, the second being the central coast around the Manabí province and the final being the northern coast along the province of Esmeraldas (Chlieh et al., 2014, Chunga, 2010; Chunga and Toulkeridis, 2014; Nocquet et al., 2014, Yepes et al., 2016; Matheus Medina et al., 2016). In the last segment of the seismic structure, the sixth strongest earthquake on the planet occurred on January 31, 1906, with a magnitude of Mw 8.8 (Kanamori and McNally, 1982) has been reported off the coast of Esmeraldas and also in Tumaco located in southwestern Colombia (Pararas-Carayannis, 1980; Ye et al., 2016; Yoshimoto et al., 2017). Later catastrophic earthquakes occurred in the same area in 1958 (Mw 7.6) and 1979 (Mw 7.7; USGS). In the southern zone of Esmeraldas, the delineation of the Galera fracture is well distinguished, so the spatial distributions of aftershock earthquakes of the Pedernales earthquake (2016, Mw 7.8) are culminating in this seismic area (Fig. 2 and 3a, 3b). As previously indicated, the largest documented earthquake for the Ecuadorian-Colombian coastal border occurred on the 31st January 1906 at 10h36 (local time), with a magnitude of 8.8 M_w had with an epicenter in the subduction zone located between 52 and 127 km away from the waterfront. The USGS catalog located the epicenter in the continental segment near the city of Esmeraldas. The tendency of crustal deformation has had a rupture extension of 450 km in length from the line Galera Muisne to Buenaventura, where moderate to high macrosysmic intensities have been documented (Rudolph and Szirtes, 1911). Other studies reported an estimated area of a greater rupture of approximately 500 Km x 180 km (Kelleher, 1972; Kanamori and MacNally, 1982).

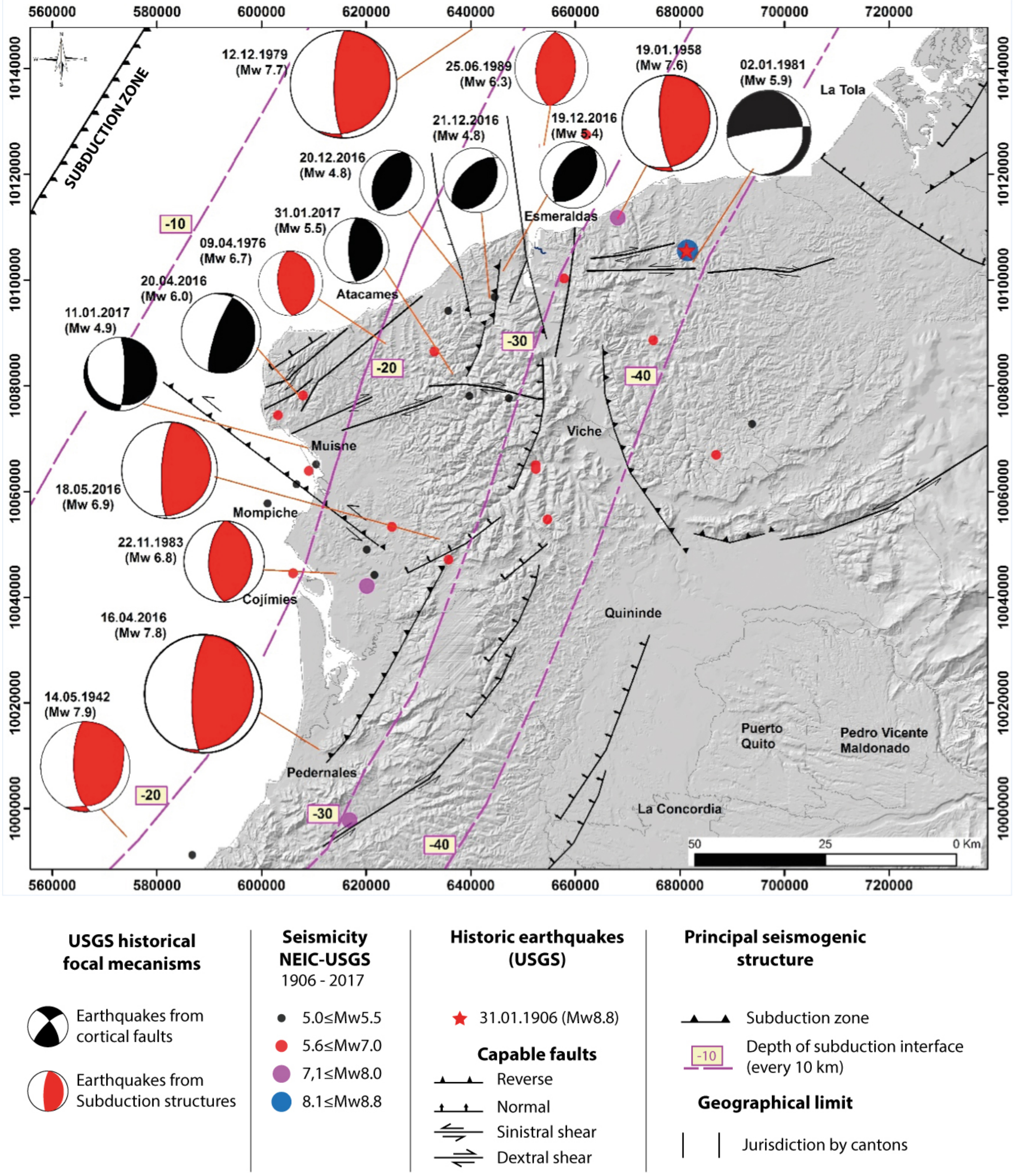

Figure 2. Seismotectonic map of the northern coast of Ecuador. Historical earthquakes with magnitude 5.0≤Mw≤8.8, some represented by focal mechanisms from the NEIC-USGS catalog, classified as earthquakes by subduction and activation of capable faults. Capable faults delineated in this study with abbreviations from FC01 to FC38, from field observations and literature data by Chunga 2010; Dumont et al., 2006; Eguez et al., 2002; Migeon et al., 2016; Ratzov et al., 2012; Reyes and Michaud, 2012. Depth of the subduction interface from Hayes et al., 2012 and Nocquet et al., 2016.

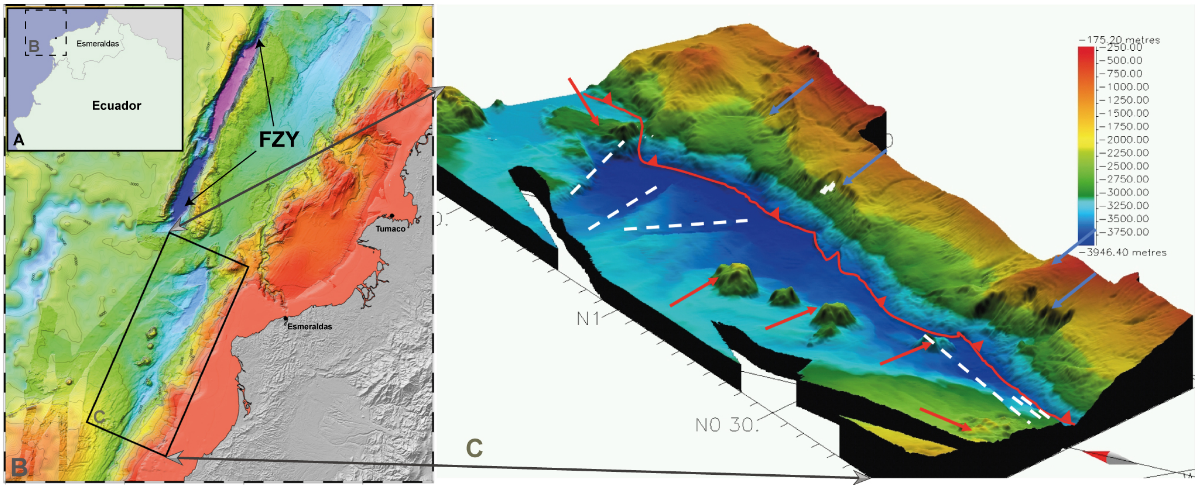

Fig. 3a: Detailed morphology of the continental rim of NW Ecuador, where inlet (b) shows the extension of the Fracture Zone of Yaquina (FZY). Its inlet (c) demonstrates further aspects of Ecuador´s active geodynamics such as deformation front evidencing suture between Nazca Oceanic Plate and Caribbean Continental Plate (red line), some active faults of the oceanic crust at its floor (white dashed lines), Seamounts which enter the subduction zone (red arrows) and some scars of landslides, fissures and submarine debris (blue arrows). Adapted from Collot et al., 2009.

Precursor earthquakes have been documented at 07h00 and 09h00, causing physical and environmental damage in the city of Esmeraldas. These coseismic effects of the second earthquake caused damage to buildings that have been added to the main earthquake (Mw 8.8), where about thirty houses collapsed. For the main event that began at 10:36 am, and lasted between three to five minutes, the premonitory earthquakes allowed many people to look for open spaces, reducing the number of victims. Subsequently, among all the replicas, that of February 2 (4:55 pm) seems to have been the strongest and most extensive, resembling its movement to the main earthquake (Rudolph and Szirtes, 1911).

The coseismic geological effects for the coasts at Esmeraldas, Rio Verde, Limones and La Tola in Ecuador and the sites of Cabo Manglares, Tumaco, Salahonda and Guapi in southwestern Colombia, documented for the epicentral area, primary effects such as subsidence and tectonic intensities of Io VIII to X MSK. The coastal margin from Bahía de Caráquez to Pedernales suff ered modest damages from the earthquake (Io VII MSK). In Manta, the earthquake was already that weak (Io VI MSK), so that many people did not even feel the movement at all (Rudolph and Szirtes, 1911). Impacts of tsunami waves occurred 30 minutes and 50 minutes after the main event, with run-up heights between 5 and 10 meters (Rudolph and Szirtes, 1911). In the site of Tumaco, waves with run-up of 2.5m of height were documented. The city of Esmeraldas was affected by the entrance of tsunami waves through the river and overflowing, flooding of the areas of plains and alluvial terraces (Espinoza, 1992). The location of the epicenter has been referred to the coordinates -79.368344 and 0.954894 at 31 km E of the city of Esmeraldas (USGS, 2017a).

The second record of a strong earthquake and subsequent tsunami for the northern coast of Ecuador occurred on January 19, 1958 with a magnitude of about 7.6 (09h09 TL, local time). The epicenter has been reported 19 km northeast of the city of Esmeraldas with the coordinates -79.4889 and 1.0106 (USGS, 2017b), which by its proximity documented the collapse of 30% of the buildings and the cracking of numerous buildings, 15 dead and 45 wounded (ie, Ramirez, 1958). The duration of this earthquake has been of about 35 to 45 seconds, and the maximum intensities with effect in the field extended up to Tumaco, where no victims were reported. In Cabo Manglares liquefaction has been evidenced of sandy soils with water expulsion to gushes of the open cracks in zone of alluvial plains estuaries. Several primary coseismic effects have been documented, such as a tsunami with a run-up height between 2.0 and 5.9 m (Lockridge, 1985), which devastated part of the coastal towns of Esmeraldas, while in the port of the city four custom guards drawn due to a damaged and sunk boat (ie, Ramirez, 1958). In addition to the earthquake and its primary coseismic effects such as the tsunami, increased intensity and run-up waves may be associated with the re-activation of multiple submarine landslides in the continental slope and in the Esmeraldas canyon (Figure X). The strongest aftershocks were documented on February 1 at 11:20 a.m., 1:10 p.m. and 15:54 p.m., the latter with the highest intensity. Ramírez (1958) documents two earthquakes until April 14, 1958 with epicenters in Esmeraldas Bay, where one person died and 14 were injured.

The third documented earthquake occurred in December 12, 1979 (Mw 7.7, Ms 7.9) at 02:59 local time, with an epicenter in the Pacific Ocean with the coordinates -79.359866 and 1.598427, (Pararas-Carayannis, 1980; USGS, 2017c), located 75 km northeast of the city of Esmeraldas and some 54 km northwest of the village of La Tola. The maximum intensities of VII to IX (IMM) were documented from Tumaco to Bozan, having a length of around 122 km in the southern coastal margin of Colombia. There, the primary coseismic effects of tectonic subsidence determined values between 0.15 m to 0.80 m of vertical displacement, while the site San Juan reached the maximum values of 1.2 to 1.6 m (Herd et al., 1981). An uplift of marine terraces has not been evidenced in the epicentral area.

For the coastal margin of Limones and San Lorenzo there are no field evidences of coseismic effects, but because of its proximity to the Tumaco site, there are certain features of subsidence and side effects attributed to the intensity of about VIII MSK (Herd et al. 1981). Liquefaction phenomena of sandy soils, sinkholes, cracks in the ground, lateral spreading and sand boils were evidenced in Tumaco (Pararas-Carayannis, 1980; Herd et al., 1981). The damages on buildings in the city of Esmeraldas were mild to moderate with an assignment of intensity of about VII, while no victims were reported. Pararas-Carayanis (1980) estimates a structural trend NW and SE of the seismic zone and a propagation of Tsunami waves with greater effect towards the NE, where the coasts of San Juan and El Charco have been washed away by waves with run-up heights between 2 to 5 meters, 6 minutes after the main earthquake. The tide level has been in its lowest position, deducing that the effects might have been more serious even with affectation for the Ecuadorian coasts if the tsunami appeared during the high tide (Espinoza, 1992). Aftershocks of moderate earthquakes that reached the magnitude of Ms 5.9 have been recorded on December 13, December 24 (Ms 5.3), December 31 (Ms 5.5) and January 7, 1980 (Ms 4.6, mb 5.1) (Herd et al. al., 1981).

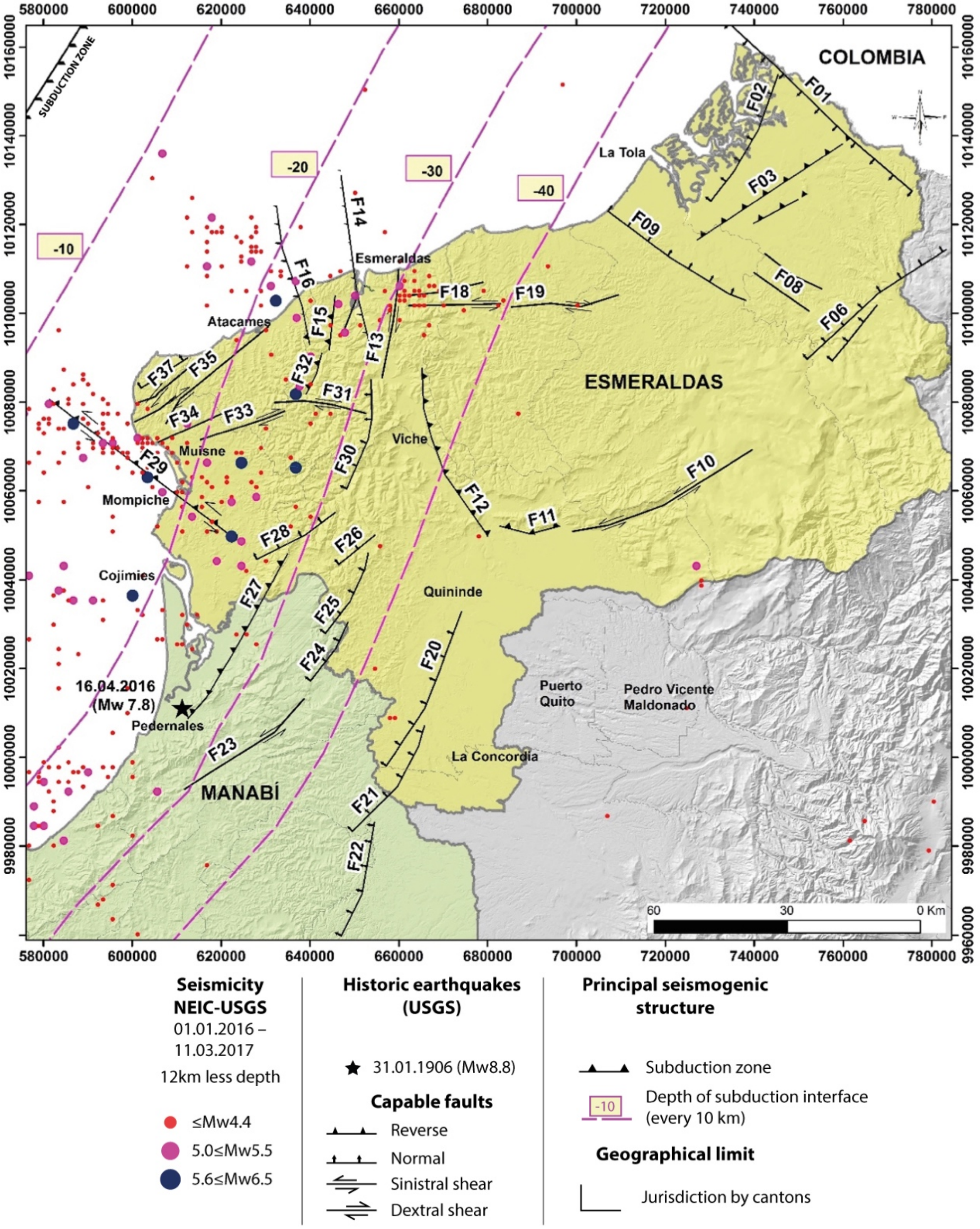

Figure 4. Capable faults and their recent activity from earthquakes recorded at a focal distance of less than 12 km. Earthquakes obtained from the IGEPN, for the time period from January 2016 to March 2017. The interrupted line represents the depth contours of the subduction interface (Hayes et al., 2012, Nocquet et al.). Greater activation of crustal faults is evidenced after the Pedernales earthquake of April 16, 2016 (Mw 7.8). The black star indicates the epicentral position of the recent earthquake of subduction (USGS, 2016; IG-EPN, 2017).

The epicentral area with the highest intensities of the Pedernales earthquake of April 16, 2016 (Mw 7.8, local time 18h58), includes the town of Pedernales and its neighboring communities of Coaque, Jama and Canoa, where the Imax IX - X ESI (Seismic Intensity, Michetti et al., 2007) have been assigned, based on evidence of coastal survey, liquefaction of soils, sinkholes, natural and stabilized slope landslides, cracks in natural soils, surface faults, transverse and longitudinal fractures In asphalt and concrete tracks (Chunga et al., 2017; Toulkeridis et al., 2017).

All of these historical earthquakes on the northern coast of Ecuador have been documented in the NEIC-USGS catalog, which provide seismicity information from 1906 to 2017, reporting 41 earthquakes in the order of magnitudes of $5.0 \leq M \leq 8.8$. Many of these earthquakes have hypocentral distances of less than 20 km in depth, and are attributed to crustal fault systems since the subduction interface zone is deeper (Fig. 4). The IGEPN's national seismological network provides additional information on seismic movements since 1988 (IG-EPN, 2017).

3. DOCUMENTED EARTHQUAKES FROM CAPABLE FAULTS

The recent Pedernales earthquake (Mw 7.8) on April 16, 2016 has provided a large amount of seismological information indicating the re-activation of smaller, capable faults in the continent, particularly in the province of Esmeraldas. In this study, earthquakes with a hypocentral distance of less than 12 km from January 2016 to March 2017 (Fig. 4), with an earthquake projection (IGEPN) and the focal mechanisms (USGS), have been used to classify the structural trend and types of faults capable of generating earthquakes. Hereby, the city of Esmeraldas, have presented a greater seismic activity of at least eight surface faults. These crustal faults have tectonic domain of inverse stress fields with shear components, and others with sinistral and dextral shear or transform faults (Fig. 2 and 4).

The sites from Cojimíes to Muisne have smaller dimensions of coseismic geological effects, where they reached and assigned degree of ESI-07 VIII. In the coastal strip between Cube-Tacu sa and Colope, it has been verified that the unstable natural slopes of clay and silt material that frequently affect the road, did not report rock falls or even minor landslides during the earthquake. In the urban center of the city of Esmeraldas minor damages of masonry of some houses have been documented (Fig. 6a-d). The intensity recorded in this sector of the province of Esmeradas has been of VI ESI-07 (Chunga et al., 2017). Oceanic tsunami propagation with oscillations of ~ 0.5 m / min has been recorded for the city of Esmeraldas between 7:06 p.m. to 7:09 p.m., while the wave amplitude did not reach the highest level since it occurred at low tide (Fig. 1 and 3; Toulkeridis et al., 2017).

In this area, historical earthquakes of moderate magnitude with fault location responsible for the activity are not well documented yet. The oldest well-documented event associated with the activation of a crustal fault is referred to the earthquake of April 9, 1976 (Mw 6.7, depth 9 km). As the city of Esmeraldas has been constructed above clayey and silty sediments within an environment of deposition of a river delta. Therefore, in saturated soils of plains and alluvial terr-

Figure 5. Spatial distribution of geomorphological features for the city of Esmeraldas, with the following abbreviations: Qa, floodplain alluvial plain; Qb: islet of flood barriers; Qt: alluvial terraces; Qc: quaternary colluvial soils; Mb: hills formed by lithologies of the Miocene and Pliocene formations Onzole and Bourbon. Photo City Courtesy: "photo & video drone Esmeraldas". Flood-prone geomorphological features may be considered to estimate the maximum run-up of tsunami waves.

aces, damages were evidences in foundations such as the Delfina Torres de Concha Hospital, the schools “5 de Agosto” and “Juan Montalvo” as well as the Central Market and several more buildings (Figure 7a-d).

Another crustal earthquake occurred on January 2, 1981 (Mw 5.9), where the type of potential shear fault is feasible with the focal mechanism information provided by the USGS (Fig. 2). The earthquake of June 25, 1989 (Mw 6.3) in front of the city of Esmeraldas, caused minor landslides and damages in the urban area (information provided by city dwellers). This available information did not indicate whether this earthquake corresponded to the subduction interface dynamics or the activation of the Esmeraldas crustal fault.

Another recent seismic activity associated with reverse-type surface faulting occurred on December 19, 2016 (Mw 5.4, Ml 5.8, depth 4 to 6 km), with an epicenter at the Tonsupa site in the Atacames area, causing damage to 70 buildings, of which 10 collapsed completely (Figure 8; IG-EPN, 2017; USGS, 2017d) being found on saturated sandy soils of a coastal plain. The next day, another earthquake of 5.2 shook the same coastal area. The last moderate earthquake report of activation of the Atacames fault (referred to as F16) has been on January 31, 2017, at 09:22 local time (Mw 5.5, Ml 5.7, depth 9 km). A particular case is that this earthquake occurred seven

Figure 6a-d. Minor damage in the center of the city of Esmeraldas by the earthquake of Pedernales of April 16, 2016 (Mw 7.8). Upper images from left to right referring to the Bolivar and Manuela Cañizares direction. Bottom images from left to right, referring to the addresses December 6 and Piedrahita, and Ricaurte and / Colon and Eloy Alfaro. Photo courtesy: "photo & video drone Esmeraldas".

minutes after the tsunami simulation organized by the Secretary of Risk Management. Damages occurred on the building of the Municipality of the city of Esmeraldas, with cracking in the masonry and collapses of some smaller walls. For the Atacames site, two buildings were also slightly affected with damage on their walls.This documented information may allow to underestimate in the assessment of seismic risk, because due to the lack of geological and seismological data the north coast may be considered as an area of seismicity generated by surface geological faults of moderate levels. Here the importance of applying this current method that allows to characterize the active or capable faults of generating crustal earthquakes with $6.0 \leq M \leq 7.3$. This would allow to obtain valuable information on the seismic potential of each fault, providing data of maximum magnitudes estimated and the PGA that could generate each geological fault in a certain site of interest.

TABLE 1. Moderate to high earthquakes, documented in the NEIC-USGS catalog, in the order of Mw≥5.0 (USGS, 2017d). The shaded squares represent the earthquakes that originated tsunamis with run-up wave heights between 1 and 5 meters. For the 1906 earthquake, wave heights between 5 and 10 meters have been documented (Rudolph and Szirtes, 1911).

Ref.	Year	Month	Day	Mw	Lat.	Long.	Depth (Km)
1	1906	1	31	8,8	0,955	-79,369	20
2	1942	5	14	7,9	-0,020	-79,950	20
3	1944	10	23	6,7	0,605	-79,320	20
4	1958	1	19	6,8	1,153	-79,543	28
5	1958	1	19	7,6	1,011	-79,489	28
6	1958	2	1	6,3	1,446	-79,146	25
7	1958	2	1	6,3	1,550	-79,305	25
8	1958	2	1	6,9	1,541	-79,338	15
9	1958	4	15	6,1	0,907	-79,581	25
10	1958	4	14	6,8	0,801	-79,428	25
11	1958	4	3	5,7	1,406	-79,547	25
12	1974	3	10	5,6	0,403	-80,047	43
13	1976	4	9	6,7	0,782	-79,804	9
14	1979	3	1	5,6	0,673	-80,073	33
15	1979	12	12	5,0	1,542	-79,377	33
16	1979	12	12	7,7	1,598	-79,358	24
17	1983	11	22	6,6	0,482	-79,877	55
18	1983	12	21	5,2	0,400	-79,907	40
19	1986	1	19	5,0	0,555	-80,041	33
20	1989	6	25	6,3	1,134	-79,616	15
21	1995	7	20	5,0	0,522	-80,091	33
20	1989	6	25	6,3	1,134	-79,616	15
22	1995	10	10	5,1	1,123	-79,350	56
23	2004	6	1	5,4	0,706	-79,744	24
24	2007	12	10	5,1	0,589	-80,007	39
25	2010	11	25	5,4	0,443	-79,920	43
26	2012	2	8	5,2	0,658	-79,258	65
27	2014	6	16	5,7	1,644	-79,250	15
28	2014	3	9	5,6	1,657	-79,350	6
29	2015	5	30	5,3	1,220	-79,570	13
30	2016	12	19	5,4	0,875	-79,700	10
31	2016	12	12	5,2	0,852	-79,780	35
32	2016	7	11	6,3	0,581	-79,630	21
33	2016	7	11	5,9	0,587	-79,630	17
34	2016	5	18	6,9	0,495	-79,610	30
35	2016	5	18	6,7	0,426	-79,780	16
36	2016	4	23	5,7	0,613	-80,250	10
37	2016	4	20	6,0	0,707	-80,030	10
38	2016	4	20	6,2	0,639	-80,210	14
39	2016	4	19	5,6	0,578	-80,020	11
40	2016	4	16	7,8	0,381	-79,920	21
41	2017	1	31	5,5	0,702	-79,676	10

Figure 7a-d. Physical damage caused by the earthquake of 9 April 1976 (Mw 6.7). Upper images from left to right referred to the site of the school “5 de Agosto” and the Central Market. Lower images from left to right, referring to the damages of the “Delfina Torres de Concha” hospital and buildings of the company CEPE - Petroecuador, in the city of Esmeraldas. Photo courtesy: Triconsul.

4. ESTIMATION OF MAXIMUM MAGNITUDES AND PGA FROM THE ANALYSIS OF CAPABLE FAULTS

For a better understanding of the structural geological terminology that we applied in our analysis, we define "capable" fault and potential source of future earthquakes, that structure that evidenced dislocations or superficial displacements during the last 30,000 years (IAEA, 2002), and / or if historical or instrumental seismicity is associated with a particular fault (Chunga, 2010). On the other hand, a fault is considered to be "potentially active" and is considered a potential source of future earthquakes if surface dislocations are evident at least once in the last 50,000 years (IAEA, 2002; Robert and Michetti, 2004; Michetti *et al*., 2007).

With this definition and in order to understand the crustal seismicity levels of the northwestern coast of Ecuador, a catalog of geological faults has been elaborated that includes 38 fault segments capable of deforming the surface of the terrain and generating potential moderate to high earthquakes, in a range of magnitudes from 6.0 to 7.3 degrees (Fig. 7). Earthquakes may be measured by their magnitude, macro-seismic intensity and PGA. The maximum PGA values estimated in our analysis have been in the order of 0.26g to 0.42g. The database includes mapped faults in the sea floor and part of the continental segment of the provinces of Esmeraldas and Manabí (Table 2). This structural geological information has been obtained from a variety of sources (Dumont et al., 2006; Eguez et al., 2002; Migeon et al., 2016; Ratzov et al., 2012; Reyes and Michaud, 2012), providing relevant information on the geometry and kinematics of each of the geological faults as well as evidence of vertical displacement from late Pleistocene to Holocene.

The geometric parameters for each of the selected faults include: (1) the spatial projection of the fault in the ground, (2) geometry and kinematics of the fault, (3) the structural immersion and estimated angle of displacement of the fault where in focal mechanism analysis it is called rake or direction of the fault and (4) the width of the seismogenic structure. It is fundamental to note here that if a fault has been modeled with several short segments instead of long segments, the maximum magnitude will be lower, and a fault slip rate requires many smaller earthquakes to accommodate a cumulative seismic moment (Well and Coppersmith, 1994).

Figure 8a-d. Structural damage caused by the earthquake of 19 December 2016 (Mw 5.4, hypocenter 4 km). Upper images from left to right refer to the collapse of foundations at the Atacames site. Bottom images from left to right, referring to the site Tonsupa, province of Esmeraldas. Photo courtesy: "photo & video drone Esmeraldas".

Estimated Magnitude (Mw) = 5.08+1.16*LOG (Lf)
Displacement of fault (in meters) = EXP(-1.38+1.02*LOG(Lf)
Where Lf, expresses the length of the capable fault.
Later, modifications and corrections have been proposed to the previous formula to estimate maximum magnitudes (Leonard, 2010).
Mw = a*log (Lf)+b; being the coefficients of, a=1.52 y b=4.33
Estimated Magnitude (Me) = 1,52*LOG (Lf)+4,33

The most common approach to estimate the maximum magnitude is through a comparison of the fault rupture length and its associated magnitude. Confirming the aforementioned, we estimated the maximum magnitudes for each of the individualized crustal faults in this study and the maximum vertical displacement based on empirical magnitude-earthquake-rupture / geological fault displacement empirical relationships proposed by Well and Coppersmith (1994).

A new proposal includes the earthquake scale ratio for each type of capable fault (Wesnousky, 2008), such as:
Transform (shear) faults; Mw = 5.56+0.87*Log(Lf)
Normal faults; Mw = 6.12+0.47*Log(Lf)
Reverse faults; Mw = 4.11 +1.88*Log (Lf)

These regression equations indicate that not all types of faults of the same dimension are able to generate earthquakes of the same value of magnitude (Stirling et al., 2013; Wesnousky, 2008). This theory has been applied for the delineated faults In the northwestern coast of Ecuador, where it is defined that those faults of the reverse type have been considered potentially capable of generating earthquakes larger than those of equal length than those of shear and normal types (Fig. 9).

Another determination of earthquakes is the PGA, of which the equation proposed by Fukushima and Tanaka (1990) has been applied. These values of PGA may be compared with the seismic zonation map of Ecuador, of the Ecuadorian Construction Standard (NEC, 2015).

The equation applied in this study has been:

Estimated PGA = (10^(0,41*Me-LOG10(Hf+0,032*10^(0,41*Me))-0,0034*Hf+1,3))/980

Hf, is the hypocenter or depth in kilometers of the geological fault.

With all these obtained data, estimations of magnitudes and PGA have been represented with spatially models of surfaces and contours associated to the active tectonics of the territory (Fig. 10), while programs or software's platform GIS and Surfer have allowed to interpolate and transform values of XYZ (X: coordinate latitude, Y: coordinate length, Z: value of magnitude), applying the gridding and nearest neighbor method on isovalues maps, as illustrated in figure 7 for data interpolations Mw and their tectonic confrontation with capable faults. The reliability levels for each of the capable faults have been applied, from seismic analysis (records of

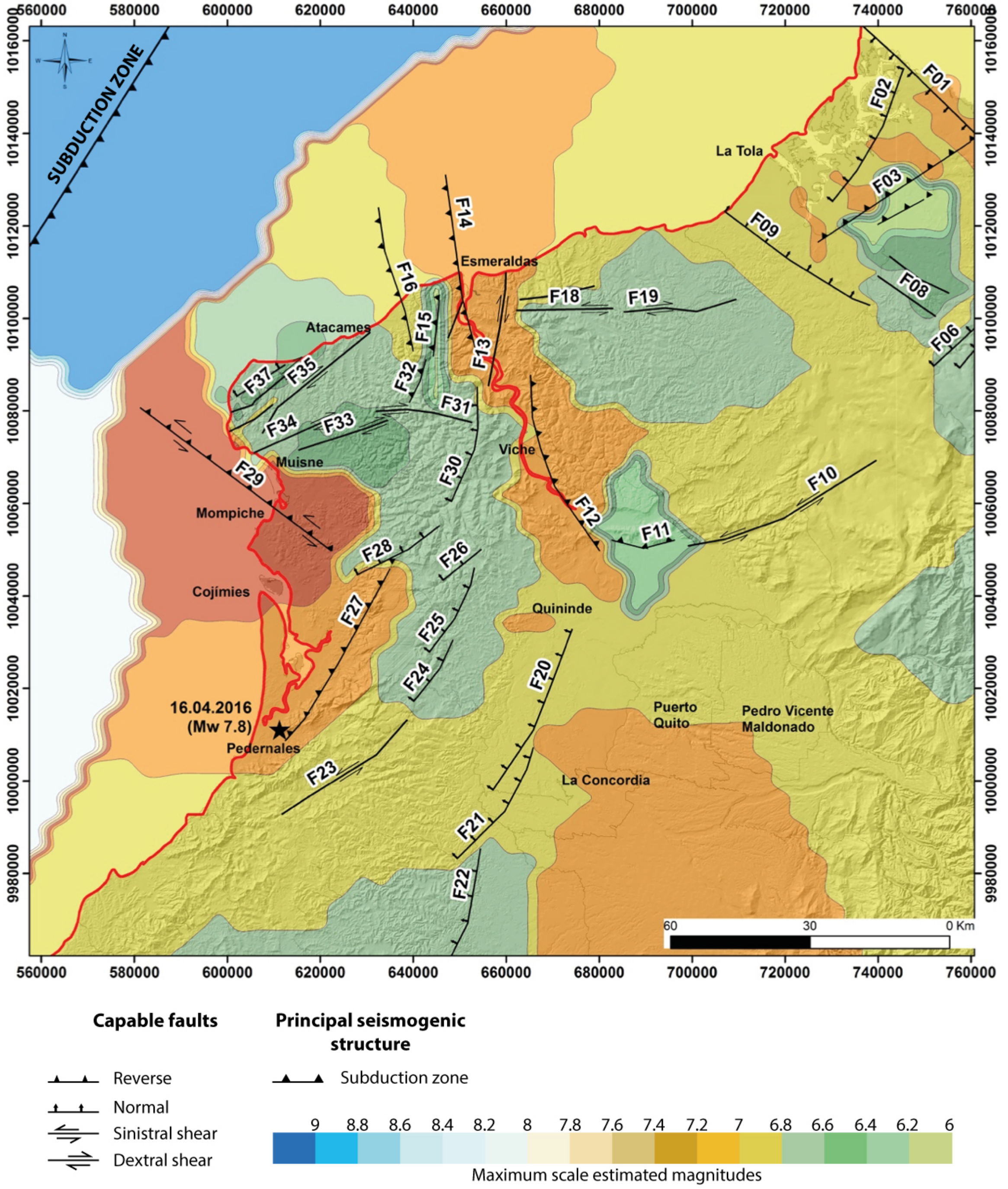

Figure 9. Estimation of maximum possible magnitudes obtained from fault analysis using the method of equations proposed by Wesnousky (2008). The abbreviations F-01 to F-38 indicate the numbering of the geological faults delineated in the north coast of Ecuador. Crustal faults have been delineated from Chunga 2010; Dumont et al., 2006; Eguez et al., 2002; Migeon et al., 2016; Ratzov et al., 2012; Reyes and Michaud, 2012.

instrumental earthquakes delineated along the structure) and morphological (faults escarpments or delineation of reliefs associated with tectonic collapse or sinking), classifying them in three categories: * I (true), ** II (deductible), and *** III (uncertain or hypothetical) (see Table 2). For a "true" structural reliability level, it is necessary that geological faults present evidence of seismicity and lateral displacements in the terrain during the Holocene. For a "deduced" level the fault must have displacement or dislocation of the well distinguished terrain in the morphometry of the relief, while for a "hypothetical" level it is when the structural guidelines may be associated with an active fault but the direction of the displacement remains unknown, or also when the earthquakes are aligned with depth less than 10 km.

The 41 capable faults selected in this study are able to generate earthquakes in the order of magnitudes ranging from 6.0 to 7.3, with the exception of the northern segment of the subduction zone located 53 and 121 km away from the coast of the province of Esmeraldas, which would be able to generate a potential earthquake in the order of 9.0 degrees of magnitude and PGA $\geq$ 0.50 g. The FC14 fault of reverse type with sinistral shear component is the closest to the city of Esmeraldas. In fact, the most developed urban area is in the area of a hanging wall. This fault is able to generate earthquakes in the order of M 7.18 and PGA in rock of 0.41g. Other faults of similar magnitudes are referred to FC03, FC12 and FC27. The Galera fault FC29 may reach the maximum of M7.33 and a PGA of 0.42, calculated from the application of Wesnousky (2008). The distance between the city of Esmeraldas and these potential faults are in the order of 25 to 77 km. However, faults of smaller magnitudes $6.1 \leq M \leq 6.9$ are located less than 10 km from the city of Esmeraldas, which are also considered because of their proximity and potential damage to the urban area, yielding a PGA between 0.27 g and 0.38 g (Fig. 10).

The information of moderate and strong earthquakes whose origin is associated to crustal geological faults, are little documented for the province of Esmeraldas. Crustal earthquakes from capable failures are reported for April 9, 1976 (Mw 6.7), January 2, 1981 (Mw 5.9), and June 25, 1989 (Mw 6.3), the latter may be associated with the Esmeraldas fault (FC14). For the Atacames fault (FC16), recent earthquakes had higher activity records from December 2016 to January 2017, reaching a Mw 5.5 (USGS, 2017d). In the area of Galera, an earthquake of Mw 6.0 occurred on April 20, 2016, considered an aftershock because it is located in the epicentral area of the earthquake of Mw 7.8, however its association with the activation of the FC35 fault is not ruled out.

1. THE ESMERALDAS FAULT AND THE SEISMIC RISK OF THE CITY OF ESMERALDAS

Remote sensing images, digital terrain models and bathymetry, earthquake focal mechanisms and gravimetric data have allowed us to characterize the dynamics and geometry of the Esmeraldas fault, which is abbreviated as F14 (Table 2) in the fault catalog. From a point of view of the gravimetric analysis for the province of Esmeraldas, we proceed from a data grid with a spacing of 1 minute (~ 2 km) between each measurement (Smith and Sandwell, 1997; Sandwell and Smith, 2009; Sandwell et al., 2013; Sandwell et al., 2014).

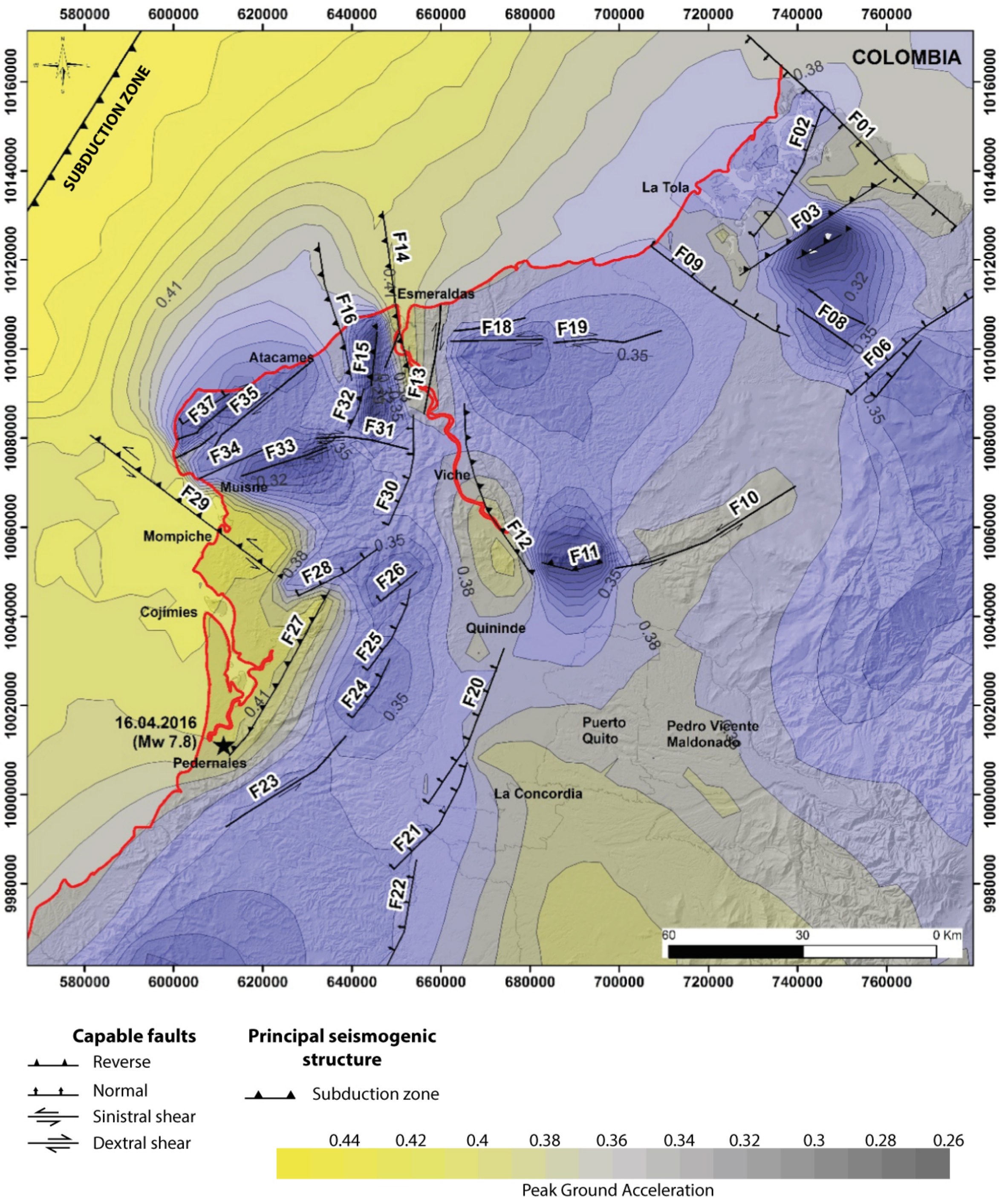

Figure 10. Estimation of obtained PGA from fault analysis using the method of equations proposed by Fukushima & Tanaka (1990). The abbreviations F-01 to F-38 indicate the numbering of the geological faults delineated in the north coast of Ecuador (Table 2).

The gravimetric data are based on the EGM2008 terrestrial gravimetric model, which was published by the National Geospatial and Intelligence Agency of the United States (NGA, 2013). This model has been calculated from combined models, that is, a robust estimation based on gravimetric measurements, terrestrial, marine and satellite models, which were tuned by spherical harmonic algorithms of degree and order of 2159, containing also additional coefficients of degree 2190 and order 2159. The gravimetric anomaly map of the Esmeraldas region and in particular for the urban area corresponds to a vertical derivative (Z), which has been processed by the software Geosoft Oasis Montaj 6.4 for the calculation of the topographic correction using a radius Minimum correction up to 500 meters, and a Bouguer correction with a reduction density of 2.7 gr / cm^3 (Fig. 11).

This first analysis plus the geomorphological features and details of bathymetric dips of the Esmeraldas canyon have allowed to delineate the length of 43 km of the fault with a structural tendency of 262/40 (dip-direction / dip). The review of focal mechanisms of surface earthquakes provided by the USGS, allowed to know the tectonic environment of deformation, being sinistral shear. Afterwards, regression equations applied to the geometric and kinematic parameters of faults allowed the estimation of the maximum magnitudes (Leonard, 2010; Stirling et al., 2013; Wells and Coppersmith, 1994; Wesnousky, 2008). For the Esmeraldas fault, this application estimates a maximum magnitude of 7.1. Hypocentral distances of crustal earthquakes near the fault allowed to associate the depth of a fault plane between 9 to 12 km (Table 3).

One of the most notable displacement features of the fault may be observed in the 1: 100,000 geological map where the upper Onzole Formation (Pliocene age) has a shear displacement in the order of 800 to 1500 m, and the formation Angostura (Mid-Miocene) in the order of 2.4 km. The Esmeraldas fault cuts off all this rocky stratigraphic sequence from the Miocene - Pliocene, so that an active tectonic rupture activity has been deduced since the Pleistocene.

From the point of view of the structural geological analysis of the Esmeraldas fault, considering the relation of moderate seismic activity with the well preserved geomorphological evidence, and the displacement rupture initiated in the Quaternary, we propose a rate of 0.4 to 0.8 mm / year for the Esmeraldas fault (Table 3). These values are confrontable with geomorphological features related to the fault activity proposed by Slemmons and Depolo (1984).

Geotechnical and superficial seismic information in the city of Esmeraldas, and geological sections, have evidenced a deformation of recent sediments as a consequence of the compressional effort exerted to the hanging block where the urban area has developed. The zone of greater deformation would occur it in the northern part of the city, and the depth of the interface rock / sediment in this place is closer to the surface, with folded layers which may be well delineated from radargrams (Chunga, 2017).

The seismic hazard levels increase in the city of Esmeraldas, due to the proximity of the geological fault capable of generating earthquakes in the order of M 7.1. In addition, the developed urban area is situated above the hangingwall position of the fault.

TABLE 2. Catalog of capable faults of generating earthquakes greater than 6 degrees of magnitudes. Estimations of maximum magnitudes for faults from applications of regression equations proposed by (^) Wesnousky (2008), and other formulas proposed by (*) Well & Coppermisth (1994) and Leonard (2010). PGA calculations are based on Fukushima & Tanaka (1990)

Capable Fault	Type	Length (km)	Depth (km)	Dist. to city (km)	Azim.	Rake	Width (km)	Structural position	Maxim. displac. (m)*	Estim. Magnit. from type of fault^	Reliability levels	PGA in Rock	Hypo-central distance (in km)	Refer.
F01	Normal	63	12	101	134	-90	11	Hanging wall	1,6	6,97	deducted	0,38	101,71	Dumont et al., 2006
F02	Normal	32	12	81	28	-90	9	Hanging wall	1,2	6,83	deducted	0,36	81,88	Dumont et al., 2006
F03	Reverse	39	12	77	58	90	10	Hanging wall	1,3	7,10	true	0,40	77,93	Dumont et al., 2006
F04	Reverse	11	12	90	60	90	7	Hanging wall	0,7	6,07	deducted	0,26	90,80	Dumont et al., 2006
F05	Sinistral shear	15	12	92	118	5	8	left-lateral	0,8	6,47	true	0,32	92,78	Dumont et al., 2006
F06	Normal	40	12	103	52	-90	10	Hanging wall	1,3	6,87	deducted	0,37	103,70	Dumont et al., 2006
F07	Normal	16	12	108	32	-90	8	Hanging wall	0,9	6,69	deducted	0,34	108,66	Dumont et al., 2006
F08	Dextral shear	15	12	89	122	-175	8	right-lateral	0,8	6,61	true	0,33	89,81	Dumont et al., 2006
F09	Normal	37	12	58	123	-90	10	Foot wall	1,2	6,86	deducted	0,37	59,23	Dumont et al., 2006
F10	Dextral shear	44	12	75	66	-175	10	right-lateral	1,3	6,92	deducted	0,38	75,95	Michaud, 2015
F11	Reverse	14	12	64	81	90	7	Hanging wall	0,8	6,26	true	0,29	65,12	Eguez et al., 2003
F12	Reverse	42	12	25	146	90	10	Foot wall	1,3	7,16	deducted	0,40	27,73	Eguez et al., 2003
F13	Dextral shear	25	12	10	12	-175	9	right-lateral	1,0	6,97	deducted	0,38	15,62	Eguez et al., 2003
F14	Reverse	43	12	1	352	90	10	Hanging wall	1,3	7,18	deducted	0,41	12,04	Eguez et al., 2003
F15	Reverse	12	12	6	8	90	7	Foot wall	0,8	6,16	deducted	0,27	13,42	This study
F16	Reverse	32	12	14	348	90	9	Foot wall	1,2	6,94	deducted	0,38	18,44	Dumont et al., 2006
F17	Dextral shear	16	12	13	77	-175	8	right-lateral	0,9	6,87	true	0,37	17,69	This study
F18	Sinistral shear	21	12	13	89	-5	8	left-lateral	1,0	6,61	true	0,33	17,69	Pontoise, 2004
F19	Dextral shear	24	12	36	81	-175	9	right-lateral	1,0	6,70	deducted	0,35	37,95	Pontoise, 2004

Continuation of Table 2

Capable Fault	Type	Length (km)	Depth (km)	Dist. to city (km)	Azim.	Rake	Width (km)	Structural position	Maxim. displac. (m)*	Estim. Magnit. from type of fault^	Reliability levels	PGA in Rock	Hypo-central distance (in km)	Refer.
F20	Normal	39	12	78	22	-90	10	Hanging wall	1,3	6,87	deducted	0,37	78,92	Eguez et al., 2003
F21	Normal	30	12	103	20	-90	9	Hanging wall	1,1	6,81	deducted	0,36	103,70	Eguez et al., 2003
F21	Normal	30	12	103	20	-90	9	Hanging wall	1,1	6,81	deducted	0,36	103,70	Eguez et al., 2003
F21	Normal	30	12	103	20	-90	9	Hanging wall	1,1	6,81	deducted	0,36	103,70	Eguez et al., 2003
F22	Normal	27	12	125	10	-90	9	Hanging wall	1,1	6,79	true	0,36	125,57	Eguez et al., 2003
F23	Sinistral shear	34	12	94	51	-5	10	left-lateral	1,2	6,81	true	0,36	94,76	Eguez et al., 2003
F24	Normal	16	12	77	22	-90	8	Hanging wall	0,9	6,69	true	0,34	77,93	Eguez et al., 2003
F25	Normal	21	12	64	3	-90	8	Hanging wall	1,0	6,74	deducted	0,35	65,12	Eguez et al., 2003
F26	Normal	11	12	58	52	-90	7	Hanging wall	0,7	6,60	true	0,33	59,23	Eguez et al., 2003
F27	Reverse	44	12	65	32	90	10	Hanging wall	1,3	7,19	deducted	0,41	66,10	Eguez et al., 2003
F28	Normal	21	12	52	61	-90	8	Hanging wall	1,0	6,74	true	0,35	53,37	Eguez et al., 2003
F29	Reverse	52	12	62	129	90	11	Hanging wall	1,4	7,33	deducted	0,42	63,15	This study
F30	Normal	26	12	22	11	-90	9	Hanging wall	1,1	6,78	true	0,36	25,06	Eguez et al., 2003
F31	Dextral shear	21	12	28	97	-175	8	right-lateral	1,0	6,79	true	0,36	30,46	This study
F32	Reverse	10	12	18	12	-175	7	Foot wall	0,7	6,71	deducted	0,35	21,63	This study
F33	Dextral shear	20	12	34	71	-175	8	right-lateral	0,9	6,44	deducted	0,31	36,06	Michaud, 2015
F34	Dextral shear	17	12	42	66	-175	8	right-lateral	0,9	6,69	deducted	0,35	43,68	Michaud, 2015
F35	Dextral shear	32	12	23	52	-175	9	right-lateral	1,2	6,63	true	0,34	25,94	Michaud, 2015
F36	Dextral shear	11	12	49	52	-175	7	right-lateral	0,7	6,87	deducted	0,37	50,45	Michaud, 2015
F37	Dextral shear	19	12	38	53	-175	8	right-lateral	0,9	6,46	deducted	0,31	39,85	Michaud, 2015
F38	Normal	13	12	42	56	-90	7	Foot wall	0,8	6,64	true	0,34	43,68	Michaud, 2015
ZS	Reverse	400	25	82	32	90	20	Hanging wall	3,6	9,00	true	≥0,50	85,73	Eguez et al., 2003

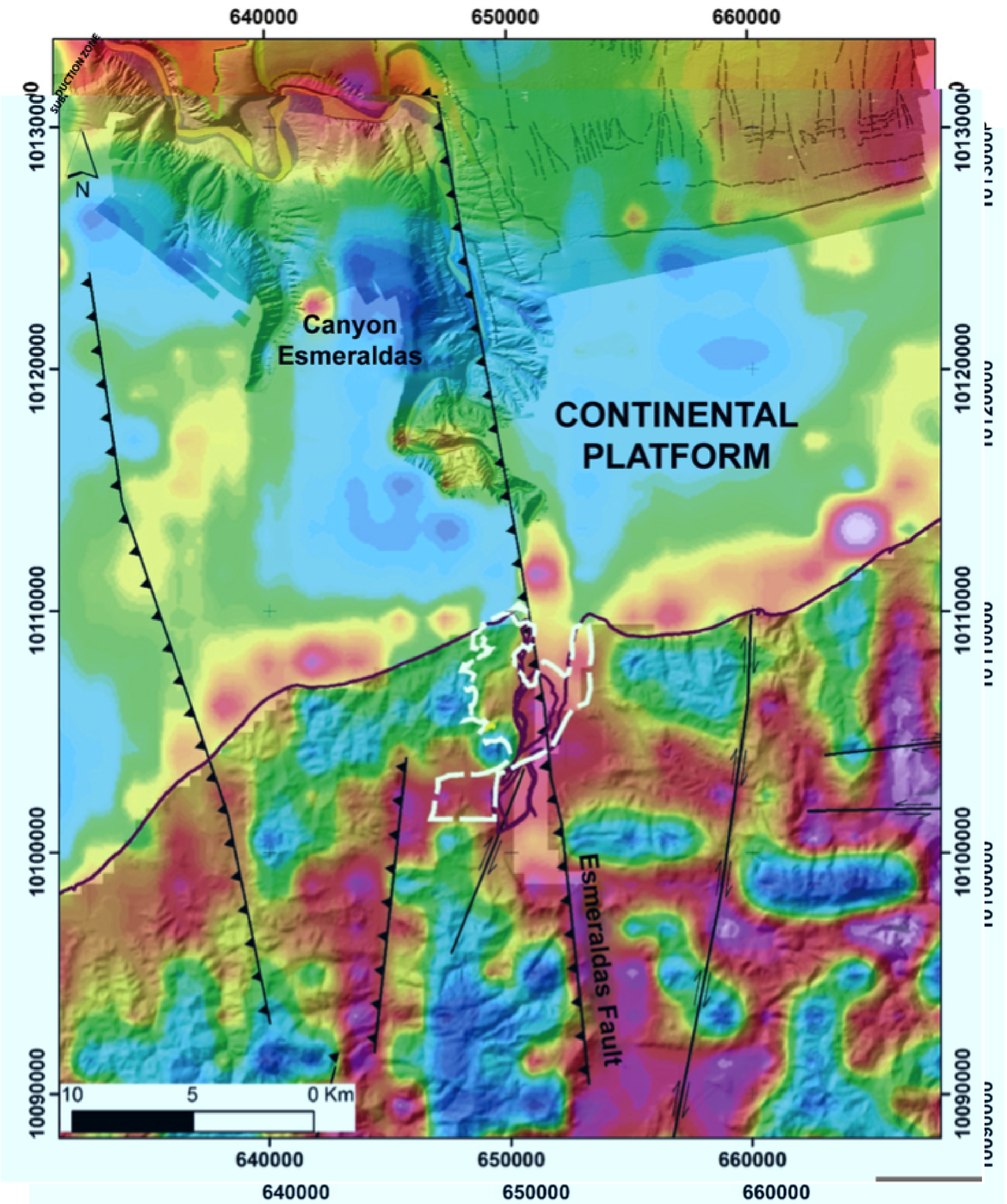

Figure 11. Delineation of the Esmeraldas fault from digital terrain models, gravimetric and seismological data. The interrupted white line is the delimitation of the study area of the city of Esmeraldas.

Table 3. Characterization of the Esmeraldas fault and its kinematic and geometric parameters.

Characterization of seismic source for the city of Esmeraldas	**Seismogenic structure**	**Type**	**Estimated length of fault based on morphologic analysis (km)**	**Distance Fault - City (km)**	**Structural fault data (dip-direction/dip)**
	Esmeraldas Fault (F-14)	Reverse with sinistral shear component	43	-1	262/40
	Estimated magnitude	**Reliability levels from seismological and morphological analysis**	**Historic earthquakes associated with the fault**	**Position of the city in respect to the fault**	**Displacement rate (mm / year) from geomorphological**
	7,18	true (I) to deducted (II)	09.04.1976 (Mw 6,7) 25.06.1976 (Mw 6,3)	Hangingwall	0,4 - 0,8

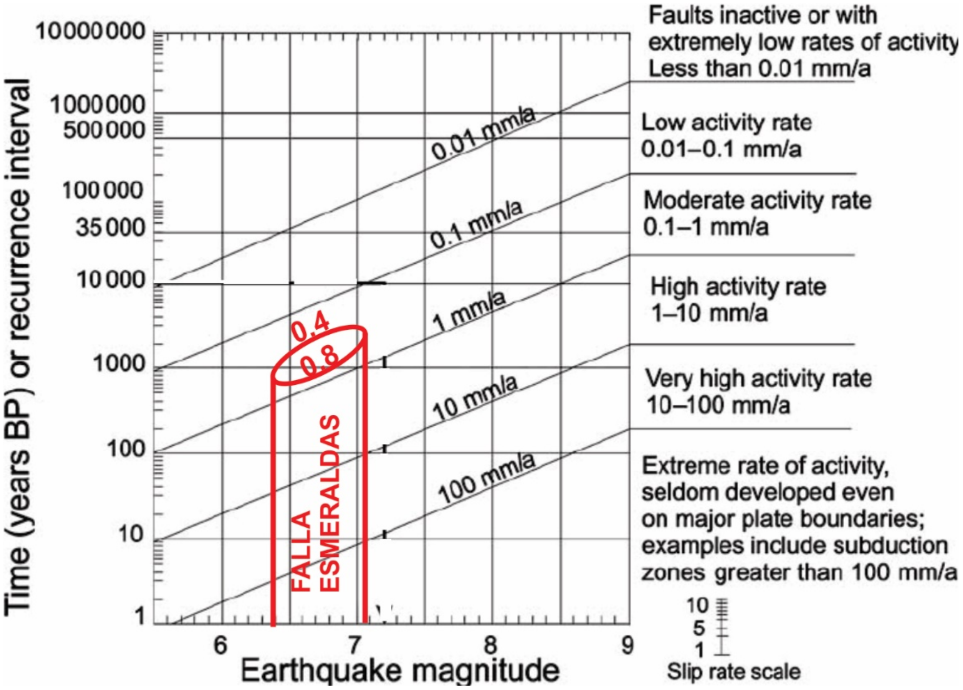

Figure 12. Estimation of the displacement rate of the Esmeraldas fault and its relation with recurrence intervals. Earthquake magnitude reference and recurrence time from Slemmons and Depolo (1984).

Therefore, the estimation of a crustal earthquake from a capable fault with M≥8 is discarded for the northwestern coast of Ecuador. The erroneous calculation to estimate this exaggerated magnitude derives from an oversized geological fault, without considering important parameters such as (a) behavior of kinematics and efforts with variable tendencies, besides the (b) morphologic-structural guidelines that are those that define in the potential segments of seismogenic structures (Chunga, 2010). These two parameters (a and b) have been respected and considered in the present study.

5. CONCLUSIONS

Well documented historical earthquakes for the northwestern coast of Ecuador begin in 1906 with Mw 8.8 and continue in 1958 (Mw 7.6), 1979 (Mw 7.7) until 2016 (Mw 7.8) and are considered to be associated with the dynamic interface of the subduction zone in front of the coasts of the province of Esmeraldas. In all these years, 41 earthquakes have been recorded among subduction and from capable faults, with magnitudes in the order of $5.0 \leq M \leq 8.8$. Crustal earthquakes from capable failures are reported for 1976 (Mw 6.7), 1981 (Mw 5.9) and 1989 (Mw 6.3).

Coseismic effects on the ground may be driven from moderate earthquakes from capable faults and also from strong distant earthquakes such as those from subduction. Coastal urban development in the city of Esmeraldas and communities increases the level of seismic risk by being above sandy saturated sediments and liquefiable sandy silts and clays. Tsunami risk should be considered between 13 and 18 m.a.s.l., which would be able to flood through tsunami run-up waves in the plains and the first alluvial terrace in the city of Esmeraldas. A preliminary paleoseismologic analysis by the authors allows to distinguish deposits of tsunamis of up to 800 m of distance from the coastline assuming the floodplain.

The estimation of a crustal earthquake (and tsunami) from a capable fault with $M \geq 8$ is discarded for the northwestern coast of Ecuador due to the evaluation of parameters such as behavior of kinematics and the consideration of morphologic-structural guidelines that define potential segments of seismogenic structures.

6. REFERENCES

Barazangi M. and Isacks, B.L. (1976). Spatial distribution of earthquakes and subduction of the Nazca plate beneath South America: Geology, v. 4, p. 686-692.

Berninghausen, W.H., 1962. Tsunamis reported from the west coast of South America 1562-1960. Bull. of the Seismological Soc. of America, 52 (4): 915-921.

Carena, S. (2011) - Subducting-plate topography and nucleation of great and giant earthquakes along the South America trench. Seismol. Res. Lett., 82 (5) 629-637, doi:10.1785/gssrl.82.5.629.

Chlieh M., Mothes P.A., Nocquet J.-M., Jarrin P., Charvis P., Cisneros D., Font Y., Collot J.-Y., Villegas-Lanza J.-C., Rolandone F., Vallée M., Regnier M., Segovia M., Martin X., Yepes H. (2014). Distribution of discrete seismic asperities and aseismic slip along the Ecuadorian megathrust. Earth Planet. Sci. Lett. 400, 292_301.

Chunga K. (2010). Shallow crustal earthquakes and seismic zonation for Ecuador through the integration of geological, seismological and morphostructural data (in Italian). University of Insubria. Ph.D. Thesis, p. 165.

Chunga K., Michetti AM., Mulas M., Besenzon D., Ferrario MF., Garces D., Ochoa F. (2017). Intensidad Macrosísmica ESI-07 y Efectos Geológicos del Terremoto de Pedernales del 16.04.2016 (Mw 7.8). VIII Jornadas en Ciencias de la Tierra. Quito, 8/14 de mayo, 207-211.

Chunga, K. and Toulkeridis, T. (2014). First evidence of paleo-tsunami deposits of a major historic event in Ecuador. Science of Tsunami Hazards. 33: 55-69.

Collot J. Y., Michaud F., Alvarado A., Marcaillou B., Sosson M., Ratzov G., Pazmino A., 2009. Visión general de la morfología submarina del margen convergente de Ecuador-Sur de Colombia: Implicaciones sobre la transferencia de masa y la edad de la subducción de la Cordillera de Carnegie. En: Geología y Geofísica Marina y Terrestre del Ecuador desde la Costa Continental hasta las Islas Galápagos. Editores: Collot J. Y., Sallares V., Pazmiño N. Impreso: Argudo & Asociados, Guayaquil-Ecuador. pp. 47-74. ISBN-978-9978-92-737-3.

De Mets, C., Gordon, R.G., Argus, D.F., y Stein, S. (1990). Current plate motions, Geophys. J. Int., 101, 425-478.

Dumont J.F., Santana, E., Valdez F., Tihay J.P., Usselmann P., Iturralde D., Navarrete E. (2006). Fan beheading and drainage diversion as evidence of a 3200-2800 BP earthquake event in the Esmeraldas-Tumaco seismic zone: A case study for the effects of great subduction earthquakes. Geomorphology 74, 100– 123. doi:10.1016/j.geomorph.2005.07.011

Eguez A., Alvarado, A., Yepes, H., Machette, M.N., Costa, C.H., Dart, R.L., and Bradley, L.-A. (2003). Database and map of Quaternary faults and folds of Ecuador and its offshore regions: U.S. Geological Survey Open-File Report 03-289.

Espinoza J. (1992). Terremotos Tsunamigénicos en el Ecuador. Acta Oceanográfica del Pacífico, 7(1), 21-28.

Fukushima Y. and Tanaka T. (1990). A New Attenuation Relation for Peak Horizontal Acceleration of Strong Earthquake Ground Motion in Japan, Bull.Seism.Soc. Am., Vol. 80, No. 4, 757-783.

Gutscher, M.A., Malavieille, J.S.L. and Collot, J.-Y., 1999: Tectonic segmentation of the North Andean margin: impact of the Carnegie ridge collision. Earth Planet. Sci. Lett. 168: 255–270.

Hayes, G.P., Wald, D.J., Johnson, R.L. (2012). Slab1.0: a three-dimensional model of global subduction zone geometries. J. Geophys. Res. Solid Earth 117, B01302 (2012).

Herd DG, Youd TL, Meyer H, C JL, Person WJ, Mendoza C. (1981). The great tumaco, Colombia earthquake of 12 december 1979. Science 211(4481):441-5. doi: 10.1126/science.211.4481.441

http://www.igepn.edu.ec/eq20160416-home

https://earthquake.usgs.gov/earthquakes/search/

IAEA International Agency of Atomic Energy Safety Standards Series (2002). Evaluation of Seismic Hazards for Nuclear Power Plants. Safety Guide. No. NS-G-3.3. International Atomic Energy Agency.

IGEPN (Instituto Geofísico de la Escuela Politécnica Nacional), 2017. Informes de los últimos sismos. (http://www.igepn.edu.ec/portal/ultimo-sismo/informe-ultimo-sismo.html)

Kanamori, H. and McNally, K. (1982). Variable rupture mode of the suduction zone along the Ecuador-Colombia coast. Bull. Seismol. Soc. Am. 72, 1241_1253.

Kanamori, H. and McNally, K.C., 1982. Variable rupture mode of the subduction zone along the Ecuador-Colombia coast. Bulletin of the Seismological Society of America, 72(4), pp.1241-1253.

Kelleher, J. (1972). Rupture zones of large South Amercan earthquakes and some predictions. Journal of Geophysical Research, vol 77, No. 11, pp. 2087-2103.

Leonard M., (2010), "Earthquake fault scaling: Self consistent relating of rupture length width, average displacement, and moment release", Bulletin of the Seismological Society of America, 100 (SA), 1971-1988p.

Lockridge, P. (1985). Tsunamis in Peru-Chile (Report SE-39, World Data Center A for Solid Earth Geophysics, 1985).

Marín J.P., Salcedo E., Castillo H. (2008). Relaciones empíricas entre parámetros instrumentales y macrosísmicos de algunos terremotos fuertes de Colombia. Boletín de Geología. Vol. 30, No. 1, 99-111p.

Medina, A. S. M., D'Howitt, M. C., Almeida, O. P., Toulkeridis, T., and Haro, A. G. (2016). Enhanced vertical evacuation application with geomatic tolos for tsunamis in Salinas, Ecuador. *Science of Tsunami Hazards*, *35*(3): 189-213.

Michaud F., Proust J. N., Collot J.Y., Lebrun J. F., Witt C., Ratzov G., Pouderoux H., Martillo C., Hernandez M. J., Loayza G., Penafiel L., Schenini Laure, Dano A., Gonzalez M., Barba D., De Min L., Ponce G., Urresta A., Calderon M. (2015). Quaternary sedimentation and active faulting along the Ecuadorian shelf: preliminary results of the ATACAMES Cruise (2012). Marine Geophysical Research, 36 (1), 81-98. ISSN 0025-3235

Michetti A.M., Esposito E., Guerrieri L., Porfido S., Serva L., Tatevossian R., Vittori E., Audemard F., Azuma T., Clague J., Comerci V., Gürpinar A., McCalpin J., Mohammadioun B., Mörner N.A., Ota Y. e Rogozhin E. (2007). Intensity Scale ESI 2007. La Scala di Intensità ESI 2007, ed. L. Guerrieri e E. Vittori (Memorie Descrittive della Carta Geologica d'Italia, vol.74, Servizio Geologico d'Italia – Dipartimento Difesa del Suolo, APAT), Roma, http://www.apat.gov.it/site/it-IT/Progetti/-INQUA_Scale/.

Migeon, S., Garibaldi, C., Ratzov, G., Schmidt, S., Collot, J.-Y., Zaragosi, S., Texier, L., (2016). Earthquake-triggered deposits in the subduction trench of the North Ecuador/South Colombia margin and their implication for paleoseismology, Marine Geology (2016), doi: 10.1016/j.margeo.2016.09.008

NEC-15 (2015). Norma Ecuatoriana de la Construcción, Ministerio de Desarrollo Urbano y Vivienda, MIDUVI, Quito.

NGA (National Geospatial and Intelligence Agency of the United States), 2013. EGM2008 – WGS 84 Version. http://earth-info.nga.mil/GandG/wgs84/gravitymod/egm2008/egm08_wgs84.html

Nocquet J.-M., Jarrin P., Vallée M. et al. (2016). Supercycle at the Ecuadorian subduction zone revealed after the 2016 Pedernales earthquake. Nature Geoscience 10, 145-149. doi:10.1038/ngeo2864

Nocquet, J.-M., Villegas-Lanza J.-C., Chlieh M., Mothes P.A., Rolandone F., Jarrin P., Cisneros D., Alvarado A., Audin L., Bondoux F., Martin X., Font Y., Regnier M., Vallée M., Tran T., Beauval C., Maguiña Mendoza J.M., Martinez W., Tavera H., Yepes H. (2014). Motion of continental slivers and creeping subduction in the northern Andes. Nat. Geosci. 7, 287_292.

Pararas-Carayannis G. (1980). Earthquake and Tsunami of 12 December 1979 in Colombia (International Tsunami Information Center, Honolulu).

Pararas-Carayannis, G. 1980: The Earthquake and Tsunami of December 12, 1979, in Colombia. Intern. Tsunami Information Center Report, Abstracted article in Tsunami Newsletter, Vol. XIII, No. 1.

Pararas-Carayannis, G., 2012: Potential of tsunami generation along the Colombia/Ecuador subduction margin and the Dolores-Guayaquil Mega-Thrust. Science of Tsunami Hazards, 31, 3: 209-230.

Ramírez J. (1958). Los terremotos de enero y febrero de 1958 en la costa del Pacífico de Ecuador y Colombia. Boletín de la Sociedad Geográfica de Colombia. Numero 58, vol. XVI.

Ratzov G, Sosson M, Collot JY, Migeon S (2012) Late quaternary geomorphologic evolution of submarine canyons as a marker of active deformation on convergent margins: the example of the South Colombian margin. Mar Geol 315–318:77–97

Reyes P, Michaud F., (2012) Mapa Geologico de la Margen Costera Ecuatoriana (1500000). EPPetroEcuador-IRD (eds), Quito, Ecuador

Robert G.P., Michetti A.M. (2004). Spatial and temporal variations in growth rates along active normal fault systems: an example from The Lazio – Abruzzo Apennines, central Italy. Journal of Structural Geology 26, 339-376.

Rodriguez, F., DHowitt, M.C., Toulkeridis, T., Salazar, R., Romero, G.E.R., Moya, V.A.R. and Padilla, O., 2016. The economic evaluation and significance of an early relocation versus complete destruction by a potential tsunami of a coastal city in Ecuador. Science of Tsunami Hazards, 35(1). 18-33.

Rudolph E, Szirtes S. (1911). "El terremoto colombiano del 31 de enero de 1906" Gerlands Beiträge zur Geophysik – Vol. XI, N° 1. Traducción: Hansjürgen Meyer, Alba de Cárdenas

Stirling M., Goded T., Berryman K., Litchfield N. (2013). Selection of earthquake scaling relationships for seismic-hazard analysis. Bulletin of the Seismological Society of America, Vol. 103, No. 6, pp. 2993-3011, doi: 10.1785/0120130052.

Toulkeridis T, Chunga K, Rentería W., Rodriguez F., Mato F., Nikolaou S., Antonaki N., Diaz-Fanas G., Cruz D´Howitt M, Besenzon D., Ruiz H., Parra H., Vera-Grunauer X. (2017). Mw7.8 Muisne, Ecuador 4/16/16 Earthquake observations: geophysical clustering, intensity mapping, Tsunami. 16th World Conference on Earthquake Engineering, 16WCEE 2017. Santiago Chile, January 9th to 13th 2017. Paper N° 5003. Registration Code: S-A1479327300

Toulkeridis, 2011: Volcanic Galápagos Volcánico. Ediecuatorial, Quito, Ecuador: 364 pp

Toulkeridis, T., Chunga, K., Rentería, W., Rodriguez, F., Mato, F., Nikolaou, S., Cruz D´Howitt, M., Besenzon, D., Ruiz, H., Parra, H. and Vera-Grunaer, X., 2017: The 7.8 M_w Earthquake and Tsunami of the 16th April 2016 in Ecuador - Seismic evaluation, geological field survey and economic implications. Science of Tsunami Hazards, in press

Trenkamp R, Kellogg JN, Freymueller JT, Mora P (2002) Wide plate margin deformation, southern Central America and northwestern South America, CASA GPS observations. J S Am Earth Sci 15:157–171

USGS (United States Geological Service), 2016: M7.8 - 29km SSE of Muisne, Ecuador. (http://earthquake.usgs.gov/earthquakes/eventpage/us20005j32#general)

USGS (United States Geological Service), 2017a: Historic Earthquakes, 1906 January 31st. (https://earthquake.usgs.gov/earthquakes/eventpage/official19060131153610_30#executive)

USGS (United States Geological Service), 2017b. M6.8 – near the coast of Ecuador. (https://earthquake.usgs.gov/earthquakes/eventpage/iscgem883714#executive)

USGS (United States Geological Service), 2017c. M7.7 – near the coast of Ecuador. (https://earthquake.usgs.gov/earthquakes/eventpage/usp00014ey#executive)

USGS (United States Geological Service), 2017d. Earthquakes Hazard Programm. (https://earthquake.usgs.gov/earthquakes/)

Veloza G., Styron R., Taylor M. (2012). Open-source archive of active faults for northwest South America. GSA Today, v. 22, no. 10, doi: 10.1130/GSAT-G156A.1.

Wells D. L. and Coppersmith K. J. (1994). New empirical relationships among magnitude, rupture length, rupture width, rupture area, and surface displacement: Bulletin of the Seismological Society of America, v. 84, p. 974-1002.

Wesnousky (2008). Displacement and geometrical characteristics of earthquake surface ruptures: issues and implications for seismic-hazard analysis and the process of earthquake rupture. Bulletin of the Seismological Society of America, Vol. 98, No. 4, pp. 1609-1632, doi: 10.1785/0120070111.

Wiens, D. A., & Stein, S. (1983). Age dependence of oceanic intraplate seismicity and implications for lithospheric evolution. *Journal of Geophysical Research: Solid Earth*, *88*(B8), 6455-6468.

Ye, L. Kanamori H., Avouac J.-P., Li L., Fai Cheung K., Lay T. (2016) The 16 April 2016, Mw 7.8 (Ms 7.5) Ecuador earthquake: a quasi-repeat of the 1942 Ms 7.5 earthquake and partial re-rupture of the 1906 Ms 8.6 Colombia_Ecuador earthquake. Earth Planet. Sci. Lett. 454, 248_258

Yepes, H., Audin, L., Alvarado, A., Beauval, C., Aguilar, J., Font, Y., Cotton, F. (2016): A new view for the geodynamics of Ecuador: implication in seismogenic sources definition and seismic hazard assessment. - Tectonics, 35, 5, pp. 1249—1279.

Yoshimoto M. Kumagai H., Acero W., Ponce G., Vasconez F., Arrais S., Ruiz M., Alvarado A., Pedraza Garcia P., Dionicio V., Chamorro O, Maeda Y., Nakano M. (2017). Depth-dependent rupture mode along the Ecuador-Colombia subduction zone. Geophysical Research Letters. 44, 2203-2210. Doi: 10.1002/2016GL071929.

ISSN 8755-6839

SCIENCE OF **TSUNAMI HAZARDS**

Journal of Tsunami Society International

Volume 36 **Number 3** **2017**

THE MISSING LINK IN EL NIÑO'S PHENOMENON GENERATION

Fernando Mato[1]*, TheofilosToulkeridis[2]

[1] Universidad de las Fuerzas Armadas ESPE, Sangolquí, Quito, Ecuador
*Corresponding author: fjmato@espe.edu.ec

ABSTRACT

The study of the El Niño phenomenon has been addressed for decades by means of the well-known ocean-atmosphere coupling model described by El Niño Southern Oscillation (ENSO) phenomenon. However, its generation mechanism has remained unknown until now, hindering the forecast of such occurrence and the degree of its intensity. Our research provides for the first time the discovery of a clear correlation pattern between a temporal inmense increase in seismicity at localized regions inside the Pacific Plate, triggered by previous telluric movements at the plate boundaries, leading to the subsequent emergence of El Niño's extraordinary events. Thus, we were able to provide supported evidence of such extraordinary climatic episodes occur due to the increase of magmatic activity in the seafloor inside the Pacific Plate, establishing the asthenosphere ocean coupling mechanism that triggers them. Furthermore, our research provides three additional major discoveries suggesting the need of rethinking both, the ENSO and the usual climate models themselves. These would be that the asthenosphere-ocean coupling mechanism becomes the major mode in the inter-annual variability of ENSO, providing the missing link in the generation of El Niño extraordinary events; the origin of the two modes of manifestation, the CP-El Niño and the EP-El Niño; and the evidence that the Southern Oscillation phenomenon governs the secondary mode of the inter-annual variability of the ENSO, generating the weak and moderate episodes of El Niño phenomenon.

Keywords: Climate, El Niño, ENSO, CP-El Niño, EP-El Niño, Seismicity.

1. INTRODUCTION

The connection between El Niño and the Southern Oscillation (SO) (Walker and Bliss, 1932) was established in 1969 by means of the ENSO (Bjerknes, 1969), considered to be the dominant mode during the inter-annual variability in the tropical Pacific, and the most dominant feature in the cyclical global climate variability (Yeh et al., 2009; Capotondi et al., 2014; Qin et al., 2014). Based on the widely accepted cyclic nature of this phenomenon, the predictability of the El Niño has been approached by means of statistical and complex dynamic computational models developed since then (McPhaden et al., 2006; Yeh et al., 2009; Capotondi et al., 2014). Surprisingly, their ability to forecast this phenomenon started to demonstrate difficulties in its detection, evolution and degree of intensity since the early 80's (Wolter and Timlin, 1998; Kessler, 2002; Philander and Fedorov, 2003; McPhaden et al., 2006; Yeh et al., 2009; Capotondi et al., 2014; Mukhin et al., 2015; Kintisch, 2016). More recently, it has been observed that various events of El Niño occurred in a different form (Philander and Fedorov, 2003; Yeh et al., 2009; Mukhin et al., 2015) (as El Niño Modoki (Ashok et al., 2007), also termed (Yeh et al., 2009) central Pacific El Niño (CP-El Niño), warm pool El Niño, or the dateline El Niño) that previously determined by the original ENSO model (The Canonical El Niño (Rasmusson and Carpenter, 1982) or eastern Pacific El Niño (EP-El Niño) (Yeh et al., 2009)), greatly hindering forecasts (Philander and Fedorov, 2003; Capotondi et al., 2014). Therefore, the uncertainty indicated by current climate models to follow El Niño's behavior also results in low confidence levels for future projections (Takahashi et al., 2011; Qin et al., 2014; Kintisch, 2016).

A high natural variability of the spatial pattern, temporal evolution and intensity of El Niño (Qin et al., 2014) has been demonstrated for the last 7000 years through a recent analysis of high resolution coral records (Cobb et al., 2013). This fact highlighted the need to incorporate other variables in the research of El Niño (Qin et al., 2014), including geosphere dynamics among them. In this sense, a hypothesis that increased seismic activity may trigger El Niño has been studied at the confluence of large plates (Walker, 1995, 1999; Guillas et al., 2010; Molchanov, 2010) in different areas of the Pacific Ocean. However, in all cases the origin of El Niño's generation mechanism has not been identified (Kessler, 2002; Philander and Fedorov, 2003; Qin et al., 2014), leading to speculative discussions regarding its volcanic (Shaw and Moore, 1988; Robock, 2000; Emile-Geay et al., 2008) or seismic (Walker, 1988, 1995, 1999; Guillas et al., 2010; Molchanov, 2010) connection. We have identified that the origin of the problem has been mainly due to five factors that hampered the study of possible relationships between El Niño and the dynamic behavior of the geosphere: (1) The existence of a link between the seismic and volcanic activities (Marzocchi et al., 2004); (2) The existence of an interplate seismic teleconnection (Bath, 1984; Marzocchi et al., 2003); (3) The observation of bidirectional cause-effect relationships (Walker, 1995, 1999; Guillas et al., 2010; Molchanov, 2010), indicating in turn different delay times; (4) The lack of an identified and proven physical mechanism linking the dynamic behavior of the geosphere inside the Pacific Ocean with El Niño phenomenon (Shaw and Moore, 1988; Walker, 1995, 1999; Robock, 2000; Guillas et al., 2010); and (5) The use of statistical correlations that only provides information about static temporal relationships (Walker, 1995, 1999; Guillas et al., 2010; Molchanov, 2010), remaining always unknown the connection of temporal-frequency dynamic information (Cooper and Cowan, 2008).

2. DATA AND METHODOLOGY

To solve the uncertainties delivered from the problem explained previously, we proceeded first to compare the time series of the Multivariate ENSO Index (MEI) (Wolter and Timlin, 1998) and the Outgoing Long Wave Radiation (OLR) (Liebmann, 1996) at Equator since June 1974, being the start date for satellite monitoring of this variable. On the one hand, the MEI method combines a set of six observed variables being: sea-level pressure, zonal and meridional components of the surface wind, sea surface temperature, surface air temperature, and the total cloudiness fraction of the sky. It is, therefore, a more complete indicator of the ocean-atmosphere coupling mechanism that the mere variation of the temperature (Sea Surface Temperature (SST) anomalies, Oceanic Niño Index (ONI)) or pressure (SOI) on the surface of the sea through the Pacific Ocean used in related studies (Walker, 1988, 1995, 1999; Guillas et al., 2010; Molchanov, 2010). The OLR, on the other hand, reflects the variation in the level of radiation coming out of the atmosphere, serving as indicator of the evaporation level from the surface of the ocean through the formation of clouds at the troposphere.

Seismic data were retrieved from IRIS catalog (http://www.iris.washington.edu/) at the Incorporated Research Institutions for Seismology (IRIS). Data in Fig. 1b, and Figs. 3 to 7 were acquired from the following coordinates inside the Pacific Plate: [10° N - 7.5° S, 160° W - 170° W], [10° N - 15° S, 170° W - 170° E], [105° N - 40° S, 170° E - 120° E] and [10° N - 40° S, 120° E - 100° E]. Before processing, seismic data located over the boundaries of the plate were removed. After this, the number of seismic events was monthly computed for the observed window, from January 1970 to March 2016. Data in Fig. 2b were acquired from the following coordinates: [5° N - 5° S, 160° E - 150° W] at the Niño 4 in the Central Tropical Pacific, and [2° N - 5° S, 82° E - 74° E] at Ecuadorian Country.

Climate data were acquired from the Climate Prediction Center (http://www.cpc.ncep.noaa.gov/) and the ESRL Physical Sciences Division (PSD), both at the National Oceanic and Atmospheric Administration (NOAA). Figure 8 was elaborated by means of the forecast data acquired from the International Research Institute for Climate and Society (http://iri.columbia.edu), part of the Earth Institute at Columbia University.

The observed window for seismic data processing was established from January 1970 (due to the lack of information about seismicity prior 1970) to March 2016, date on which the arrival of the forecasted very strong Godzilla El Niño was officially discarded. Although climate data are available since 1950, the observed window for climate data processing was also fixed to this period for correlation purposes. In the case of OLR data processing, the observed window starts in June 1974 due to the absence of data for previous months. All data used in our research have been integrally processed with MATLAB and Statistics Toolbox Release 2013a, MathWorks (www.mathworks.com/). Data correlation in Fig. 1 and Fig. 3 has been conducted by means of the wavelet-transform-based semblance analysis (Cooper and Cowan, 2008).

3. ANALYSIS AND RESULTS

First, we proceeded to carry out a long-time correlation analysis between MEI and OLR time series (Fig. 1a), and between MEI and Min-Max normalized seismicity series (Fig. 1b). By means of the Continuous Wavelet Transform (CWT) it is indicated the frequency content evolution over time for each time series; bright red in real part values of the complex CWT indicates a large positive amplitude while dark blue indicates a large negative amplitude. Then, the correlation analysis between time series (bottom) is conducted by means of the wavelet-transform-based semblance. Results indicate high correlation degree in dark red ($\rho = 1$), high anti correlation degree in dark blue ($\rho = -1$), and non correlation degree ($\rho = 0$) in green. Our results (Fig. 1a) evidence the existence of four anomalies for the period of observation. We have obtained identical results (but with lower resolution) correlating the OLR values with both, ONI and SOI time series. Such anomalies in the correlation of time series indicate that their generation is unrelated with the SO phenomenon. In a different way, we encountered that all anomalies are related with a previous unusual increase in seismicity inside the Pacific Plate (Fig. 1b). Moreover, the first two anomalies are located around El Niño's very strong event occurred in the period of 1982-83, and the third before El Niño's very strong event occurred in the period of 1997-98.

After this, we proceeded to compare the time series of the MEI (Fig. 2a) and the seismicity values (Fig. 2b) registered at Niño 4 region [5° N - 5° S, 160° E - 150° W] and the Ecuadorian Country [2° N - 5° S, 82° E - 74° E], between January 1970 and March 2016. Current climate models associate positive values of MEI (high values shown in red in Fig. 2a) with the warm ENSO phase (El Niño phenomenon), and negative values of MEI (low values shown in blue in Fig. 2a) with the cold ENSO phase (La Niña phenomenon). In this regard, and unlike current climate models, we were able to observe that Niño 3-4 region does not provide discriminating information to detect the generation of El Niño's very strong episodes. The same occurs with Niño 3 data. Furthermore, we discovered that the combined information from both, Niño 4 and Ecuadorian Country regions, provide a clearer seismic correlation (Fig. 2b), observing the existence of an extraordinary correlation between the seismic activity in the Niño 4 region (Fig. 3a and Fig. 5a) three months prior the generation of El Niño's very strong event occurred in the period of 1982-83. Similarly, Fig. 3b and Fig. 6c demonstrate this high correlation degree in both regions, clearly discriminated from Niño 4 region twelve months before the generation of El Niño's very strong event occurred in the period of 1997-98. Finally, Fig. 2b and Figs. 4 to 7 also support our hypothesis by means of the existence of a high correlation degree between the previous generation of seismic events, in this occasion with low levels of seismicity, and the subsequent appearance of El Niño phenomenon less intense (Takahashi et al., 2011). In all other residual periods of times, when low levels of seismicity appear, the correlation analysis evidences that other mechanism governs the remaining El Niño episodes of low degree of intensity.

Our study confirms that the increase of seismicity within the Pacific Plate initiates by increased seismicity at its eastern and western boundaries. Figures 4 to 7 illustrate the spatio-temporal distribution of intraplate seismicity from January 1970 to March 2016. For each year the temporal evolution of earthquakes registered is shown from January (light red) to December (dark red), with their intensity represented by the diameter of the circles. There, most of the earthquakes produced in early-year are located in the western end of the intraplate, preceding the remaining earthquakes located inside the plate the rest of the year. Thus, the generation of El Niño's very strong event during 1982-1983 is indicated by a previous increase in the seismicity at coordinates [1° S - 6.5° S, 175° W - 180° W] of Kiribati (Gilbert Islands) and Tuvalu archipelagos since late 1981 (Fig. 4l). Similarly it behaves with the generation of El Niño's very strong event during 1997-1998 at coordinates [0° - 40° S, 151° E - 180° E] of Fiji, Samoa, Tonga, Kermadec and North Islands since late 1995 (Fig. 6b). Additionally, an increase in the seismicity of low intensity is indicated at coordinates [12° S - 30° S, 140° E - 155° E] of the French Polynesia (Society and Tubai Islands) at Central Pacific during 1993-1994 (Fig. 5l and Fig. 6a) and during 2002-2010 (Figs. 6i to 6l and Figs. 7a to 7e), correlated in time with the generation of El Niño Modoki (Ashok et al., 2007; Takahashi et al., 2011).

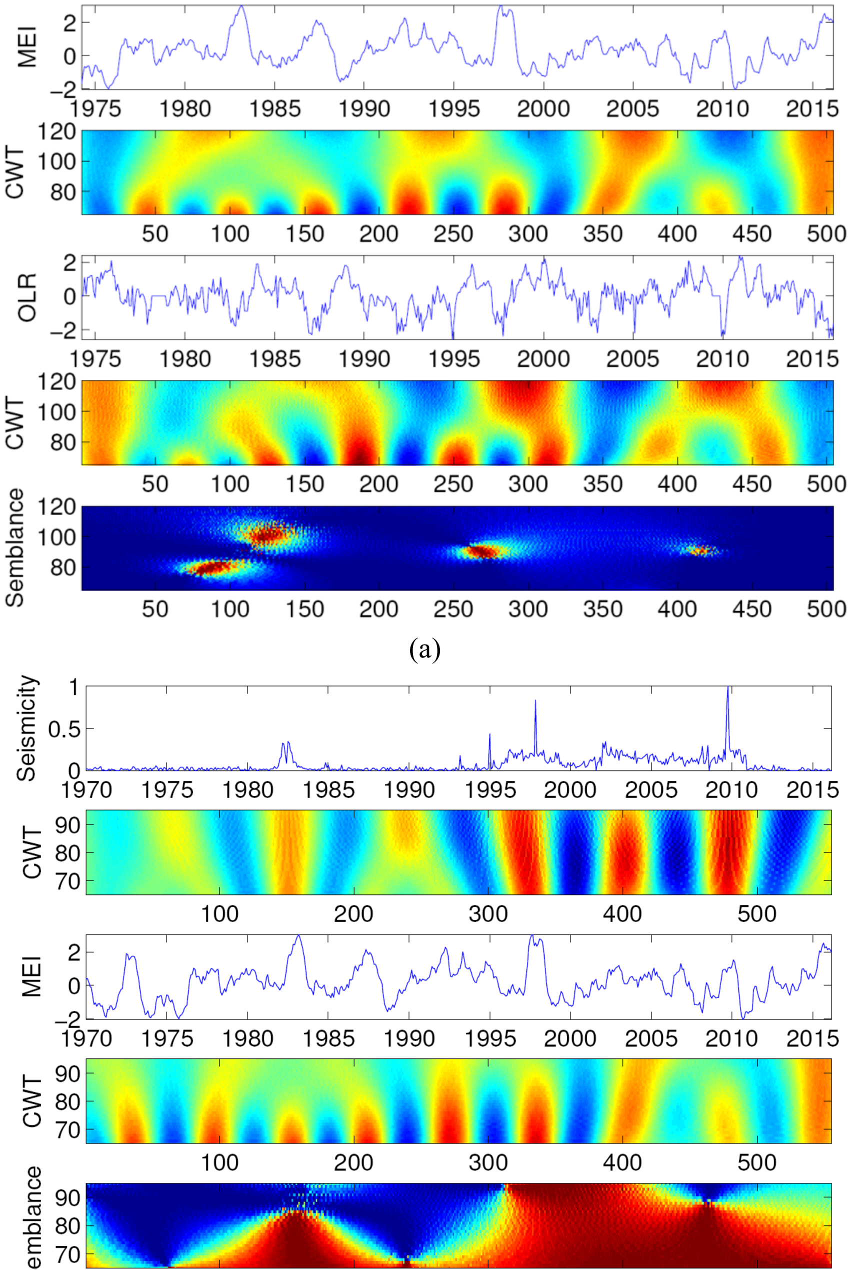

(a)

(b)

Fig. 1: Long-time correlation analysis by means of the Continuous Wavelet Transform (CWT): (a) MEI and OLR time series; (b) Min-Max normalized seismicity and MEI time series registered inside the Pacific Plate: [10° N - 7.5° S, 160° W - 170° W], [10° N - 15° S, 170° W - 170° E], [105° N - 40° S, 170° E - 120° E] and [10° N - 40° S, 120° E - 100° E].

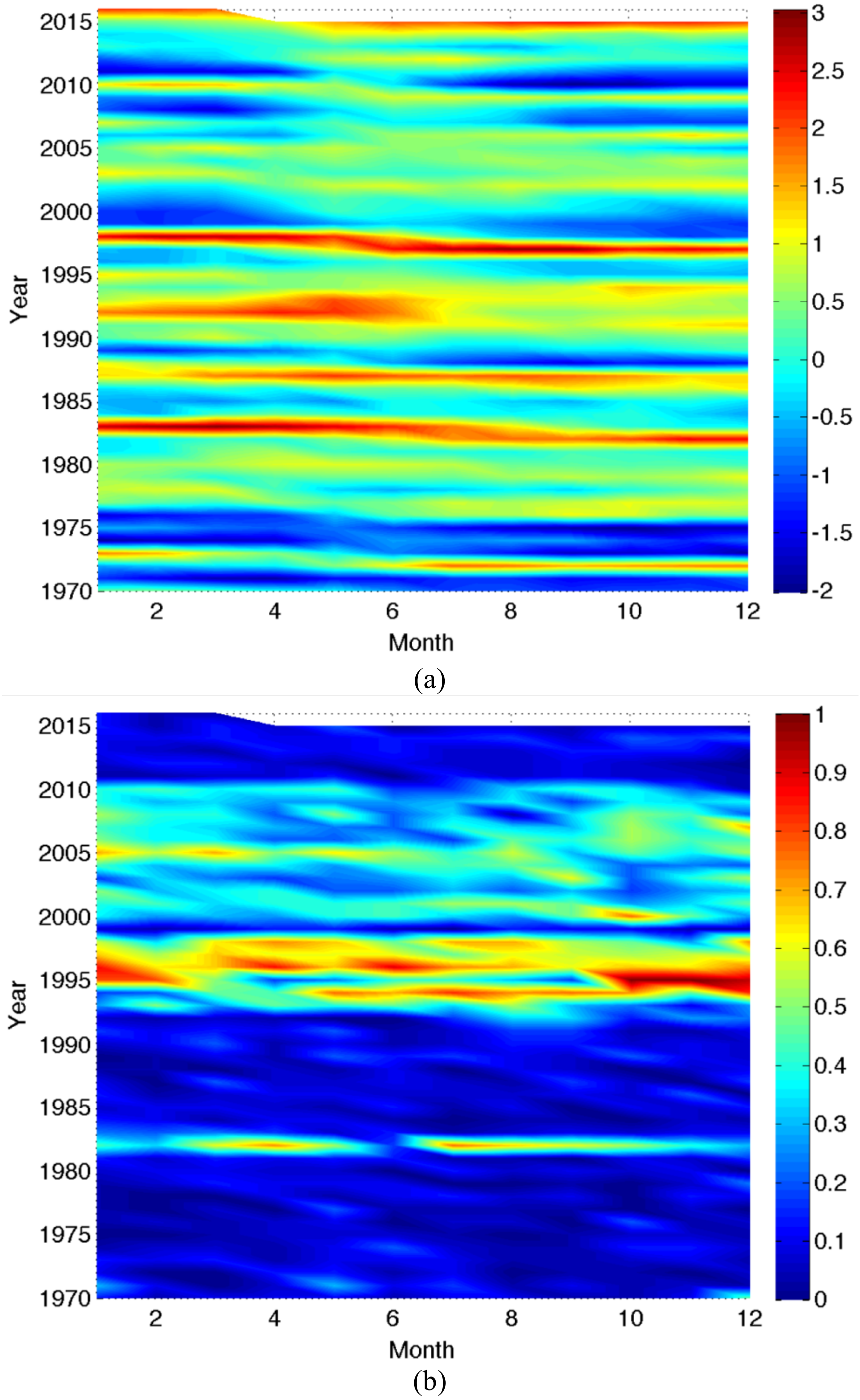

Fig. 2: Long-time anomalies analysis: (a) MEI time series; (b) Min-Max normalized seismicity time series registered at Niño 4 region [5° N - 5° S, 160° E - 150° W] and the Ecuadorian Country [2° N - 5° S, 82° E - 74° E], between January 1970 and March 2016. Results indicate the location of anomalies (high values) shown in hot colors versus low seismic activity shown in cold colors.

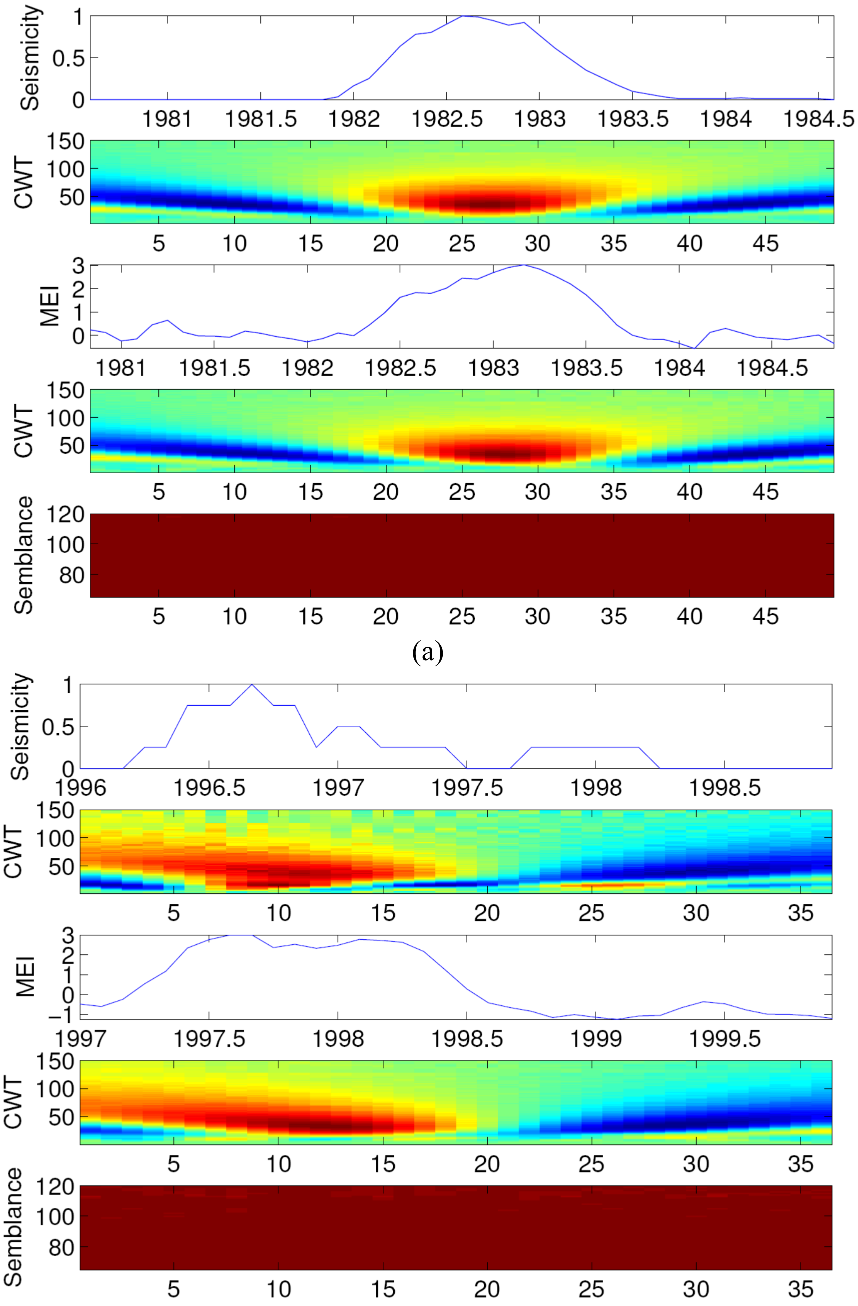

(a)

(b)

Fig. 3: Short-time correlation analysis by means of the Continuous Wavelet Transform (CWT). MEI time series and Min-Max normalized seismicity inside the Pacific Plate: (a) El Niño's very strong event occurred in the period 1982-83; (b) El Niño's very strong event occurred in the period 1997-98; In both cases results indicate high correlation degree in dark red ($\rho = 1$); in both cases the wavelet-transform-based semblance analysis indicate high correlation degree in dark red ($\rho = 1$).

(a) 1970 (29 Earthquakes) (b) 1971 (7 Earthquakes) (c) 1972 (19 Earthquakes)

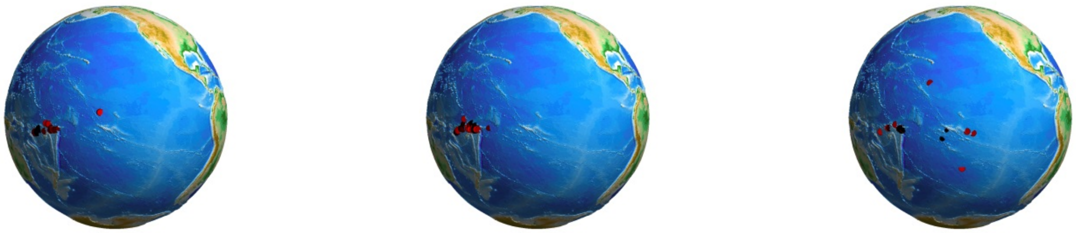

(d) 1973 (22 Earthquakes) (e) 1974 (32 Earthquakes) (f) 1975 (20 Earthquakes)

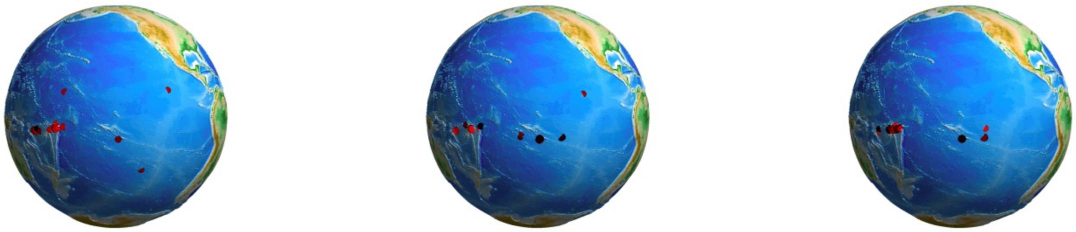

(g) 1976 (23 Earthquakes) (h) 1977 (21 Earthquakes) (i) 1978 (32 Earthquakes)

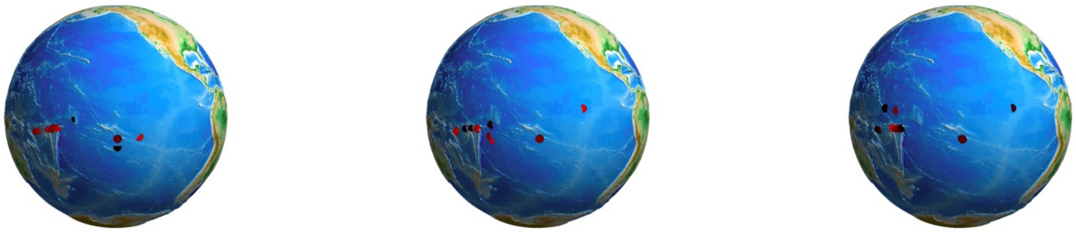

(j) 1979 (20 Earthquakes) (k) 1980 (17 Earthquakes) (l) 1981 (29 Earthquakes)

Fig. 4: Spatio-temporal distribution (1970-81) of the earthquakes registered inside the Pacific Plate at coordinates [10° N - 40° S, 100° E - 160° W], from January (light red) to December (dark red) months.

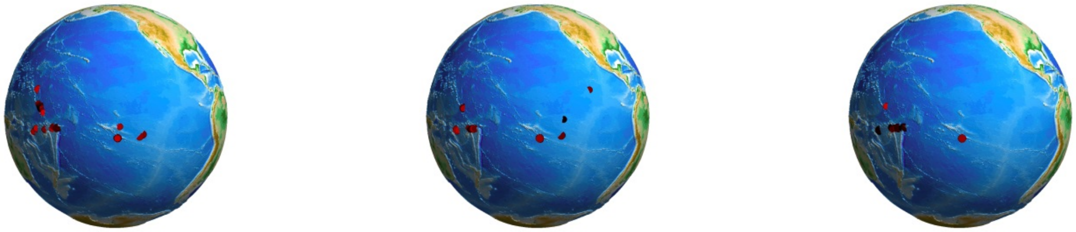

(a) 1982 (271 Earthquakes) (b) 1983 (44 Earthquakes) (c) 1984 (30 Earthquakes)

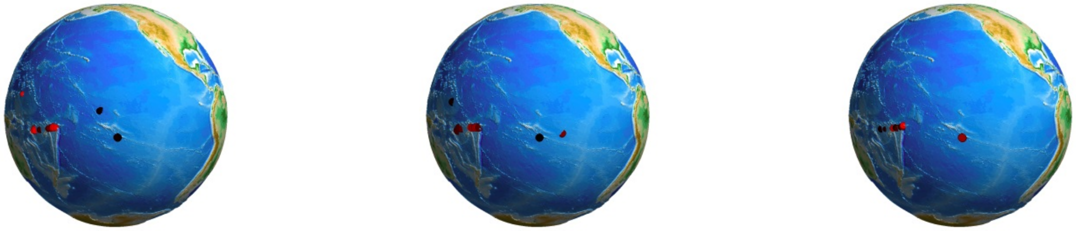

(d) 1985 (24 Earthquakes) (e) 1986 (19 Earthquakes) (f) 1987 (18 Earthquakes)

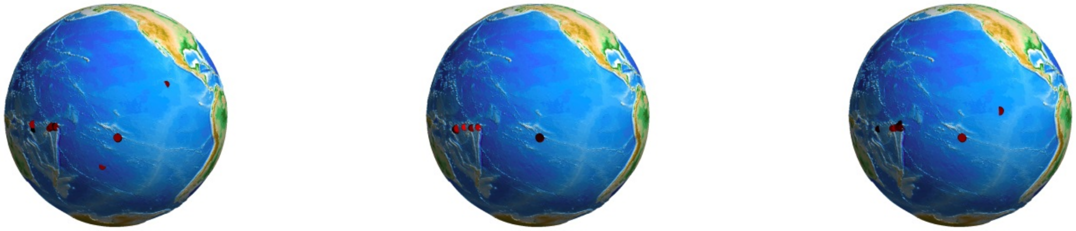

(g) 1988 (22 Earthquakes) (h) 1989 (17 Earthquakes) (i) 1990 (20 Earthquakes)

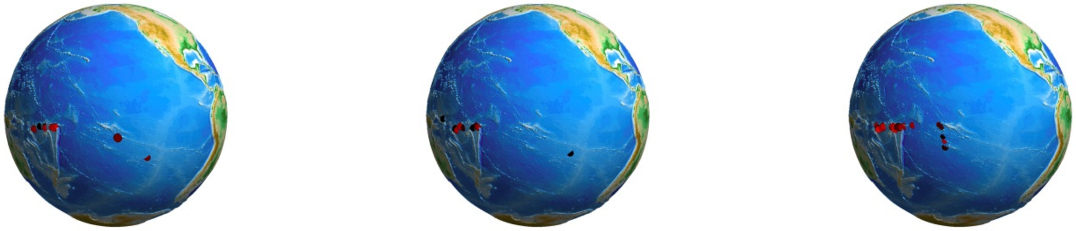

(j) 1991 (15 Earthquakes) (k) 1992 (13 Earthquakes) (l) 1993 (42 Earthquakes)

Fig. 5: Spatio-temporal distribution (1982-93) of the earthquakes registered inside the Pacific Plate at coordinates [10° N - 40° S, 100° E - 160° W], from January (light red) to December (dark red) months.

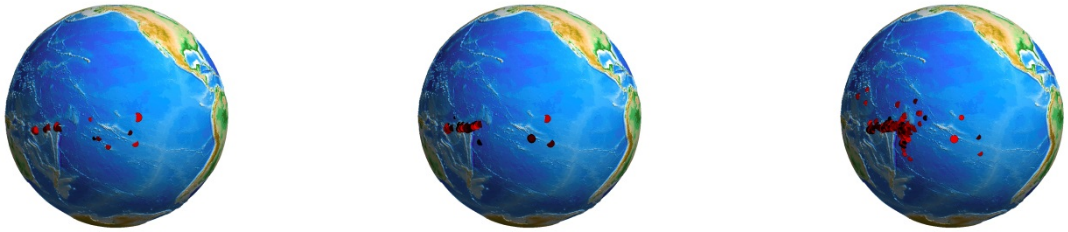

(a) 1994 (28 Earthquakes) (b) 1995 (112 Earthquakes) (c) 1996 (249 Earthquakes)

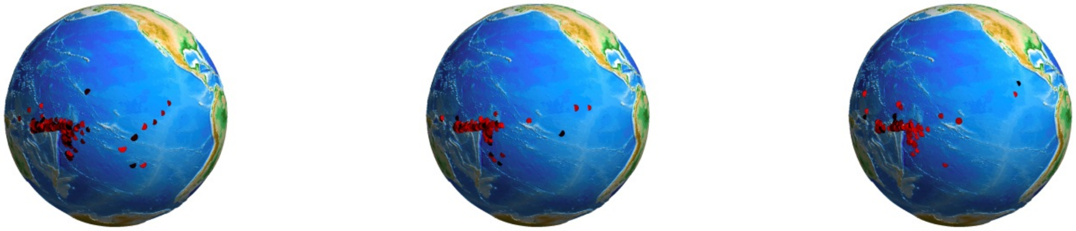

(d) 1997 (301 Earthquakes) (e) 1998 (190 Earthquakes) (f) 1999 (129 Earthquakes)

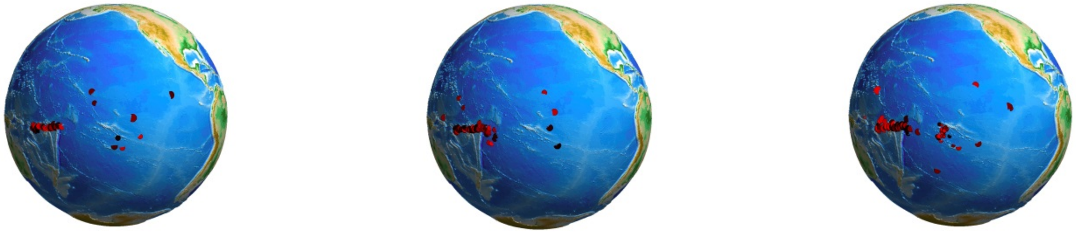

(g) 2000 (81 Earthquakes) (h) 2001 (124 Earthquakes) (i) 2002 (298 Earthquakes)

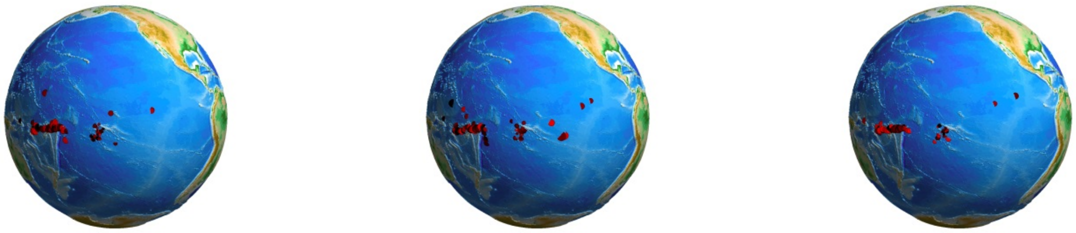

(j) 2003 (212 Earthquakes) (k) 2004 (200 Earthquakes) (l) 2005 (164 Earthquakes)

Fig. 6: Spatio-temporal distribution (1994-2005) of the earthquakes registered inside the Pacific Plate at coordinates [10° N - 40° S, 100° E - 160° W], from January (light red) to December (dark red) months.

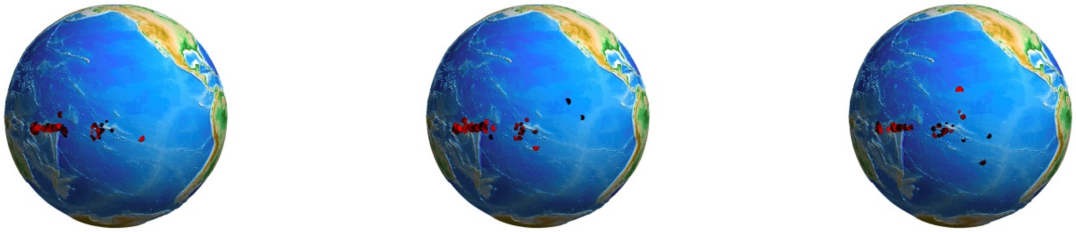

(a) 2006 (183 Earthquakes) (b) 2007 (133 Earthquakes) (c) 2008 (186 Earthquakes)

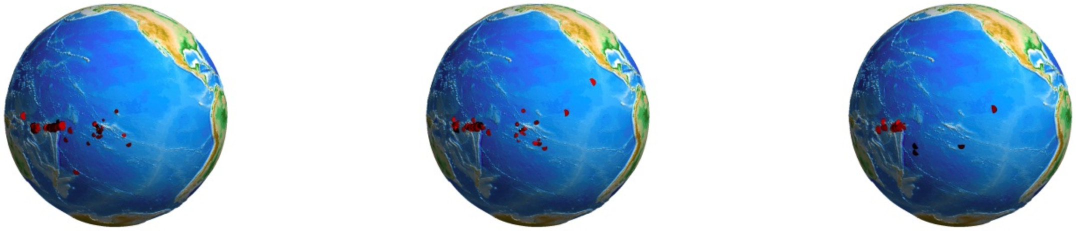

(d) 2009 (363 Earthquakes) (e) 2010 (227 Earthquakes) (f) 2011 (34 Earthquakes)

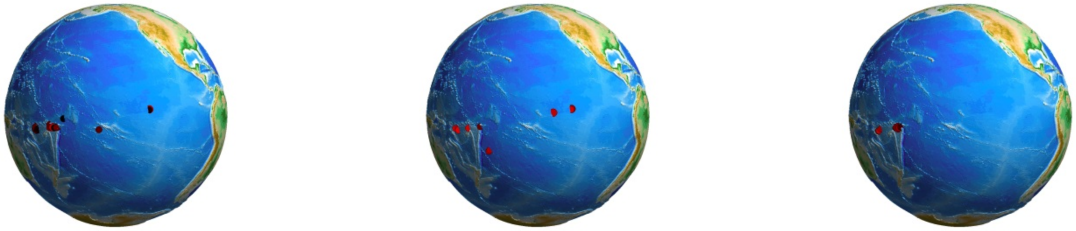

(g) 2012 (23 Earthquakes) (h) 2013 (10 Earthquakes) (i) 2014 (14 Earthquakes)

(j) 2015 (7 Earthquakes) (k) 2016 (6 Earthquakes)

Fig. 7: Spatio-temporal distribution (2006-March 2016) of the earthquakes registered inside the Pacific Plate at coordinates [10° N - 40° S, 100° E - 160° W], from January (light red) to December (dark red) months.

4. DISCUSSION

Based on the new findings mentioned above, we suggest that the increase of seismicity inside the plate further drives magma activity increase on the seafloor of the Central Pacific where hot spots are located, which subsequently increase the sea temperature (Shaw and Moore, 1988; French et al., 2013; French and Romanowicz, 2015). The connection with the upper mantle magma activity has recently been demonstrated by French et al. through the detection of a reduction of between 2 % to 4 % in the speed of seismic waves, reaching in some cases to 10 % (French and Romanowicz, 2015). This decrease in velocity, found using seismic inversion models (French et al., 2013; French and Romanowicz, 2015), is linked to an increase in viscosity due to the presence of magma plumes that connect the upper mantle to the surface of the ocean. The temperature reached (400 °C - 1200 °C) across the width of these plumes (800 km) (French and Romanowicz, 2015) would also be more than enough to trigger earthquakes by a decrease in pressure levels (Molchanov, 2010). We established that this asthenosphere-ocean coupling mechanism (that we named Asthenosphere Generation of El Niño Oscillation (AGEO)) generates the strong and very strong episodes of El Niño determining the major mode (high degree of correlation in semblance (Fig. 1b)) of inter-annual variation in ENSO. This major mode (AGEO) acts on the ocean-atmosphere-coupling mechanism generating low pressures (negative values in the SOI series) and increases in sea surface temperature (positive values in the ONI series). For periods of low seismicity, however, El Niño is governed by the SO phenomenon determining the secondary mode (high degree of anticorrelation in semblance (Fig. 1b)) of inter-annual variation of the ENSO generating less intense episodes of El Niño in its warming periods. During cooling periods, the generation of high pressures (positive values in the SOI series) and negative anomalies in the sea surface temperature (negative values in the ONI series) contribute (apart of other natural variables) to a further increase of seismicity at the Pacific Plate's boundaries by a reduction in the sea surface pressure (Luttrell and Sandwell, 2010), in accordance with results obtained by Guillas et al. (Guillas et al., 2010).

In 2015-2016, the SST at the Pacific Ocean registered a similar pattern to that presented by the very strong El Niño events in 1982-83 and 1997-98. Therefore, according to the ENSO climatic models, an El Niño's very strong event would take place, but the necessary ocean-atmosphere coupling did not occur. As a necessary condition, our results evidence the need for a high level of seismic activity inside the Pacific Plate several months prior the generation of the CP-El Niño and the EP-El Niño extraordinary episodes, whose spatial location and intensity define which type will take place. In this respect, the results illustrated in the Figs. 7i to 7k invalidate the ENSO-based forecasts of occurrence of the so-called Godzilla El Niño (Fig. 8). Such extraordinary event has not been triggered and the global climatic effects greatly differed from those expected by the current ENSO model (Kintisch, 2016). Moreover, we evidenced that the CP-El Niño and the EP-El Niño have the same origin, confirming the hypothesis given by Takahashi et al. (Takahashi et al., 2011) about the existence of only two regimes of El Niño: (1) strong and very strong events, and (2) weak and moderate events. This provides additional evidence that the first type is generated by the AGEO coupling model, and the second type by the SO model. For each regime, the intensity of the El Niño's events would be subsequently modulated by the annual cycle and the Pacific and Atlantic dynamics, providing thus a needed physical explanation to the three nonlinear dynamical modes (NDMs) extracted by Mukhin et al. (Mukhin et al., 2015).

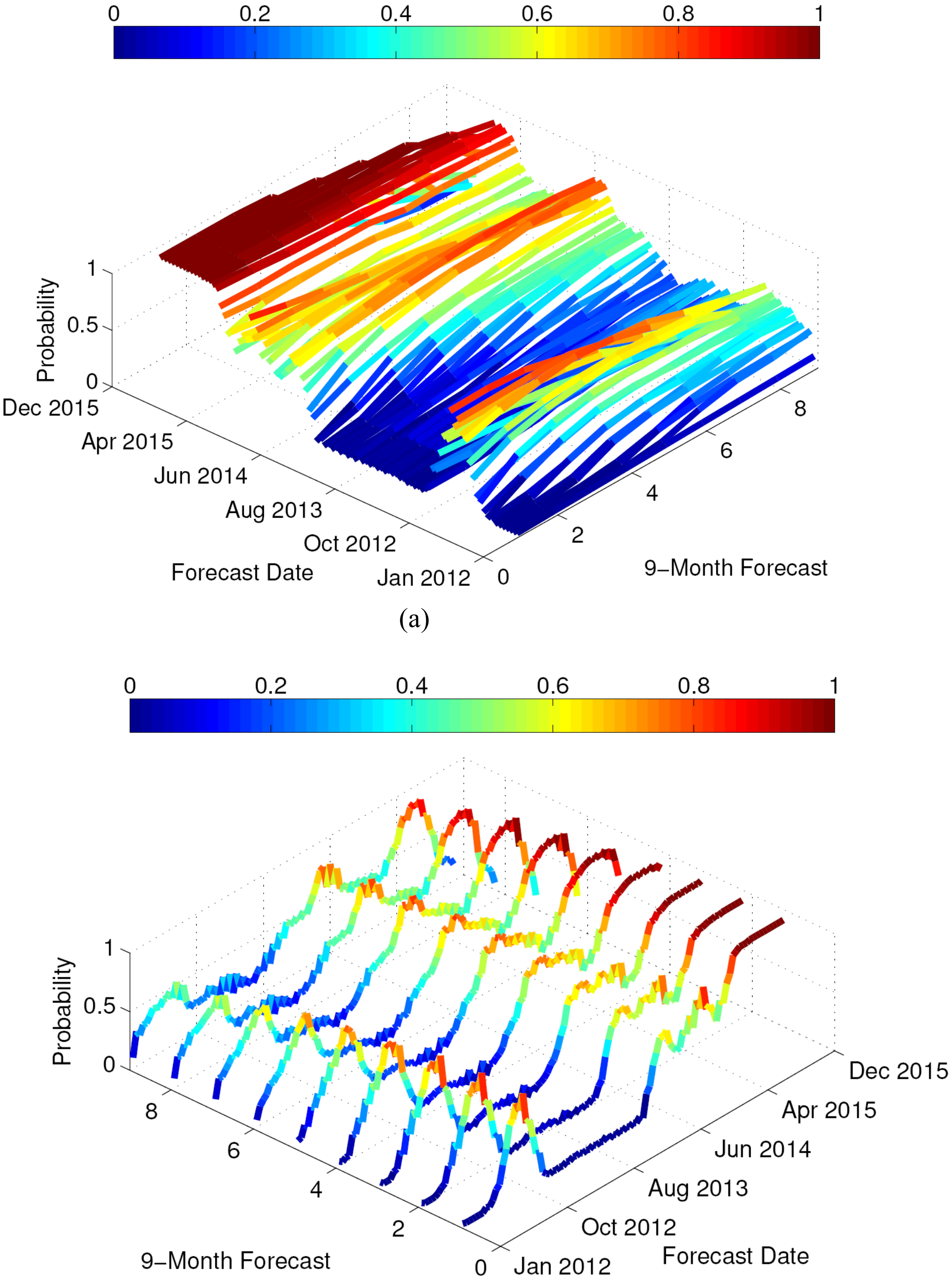

(a)

(b)

Fig. 8: Temporal series of the CPC/IRI early-month consensus ENSO forecast probabilities from January 2012 to December 2015: (a) Biweekly forecast series; (b) 9-Month forecast series. Data acquired from the International Research Institute for Climate and Society (http://iri.columbia.edu).

5. CONCLUSIONS

As a major discovery, our research solves the origin about the El Niño's generation, providing supported evidence about the asthenosphere-ocean coupling mechanism that triggers its extraordinary events. Furthermore, our study provides three additional major discoveries: (1) This asthenosphere-ocean coupling mechanism (AGEO) becomes the major mode in the interannual variability of ENSO, providing the missing link in the generation of El Niño and delivering the needed explanation to the mismatch of the climate models in forecast its very strong episodes since the early-80s; (2) This major mode provides a needed explanation for the origin of the two modes of manifestation (the CP-El Niño and the EP-El Niño); and (3) The evidence that for periods of low seismicity the SO governs the secondary mode of the inter-annual variability of the ENSO, generating less intense episodes of El Niño during its warming periods.

We are able to finally conclude that El Niño is not well linked to the SO by means of the current ENSO model, suggesting the need for rethinking both, the ENSO and the usual climate models themselves. This conclusion is reinforced by the great uncertainty and lack of precision still demonstrated by these models in the recent forecast of the arrival of the so-called Godzilla El Niño. Based on our results, we are also able to anticipate two fundamental facts: First, the conditions for the generation of an El Niño's very strong event with global effects, similar in intensity to those occurred during 1982-83 and 1997-98, had not yet taken place. Second, these conditions will not take place in a short-term based on the current period of minimal seismicity inside the Pacific Plate since 2013.

ACKNOWLEDGEMENTS

We thank the IRIS Data Management Center, the Climate Prediction Center (NOAA), the ESRL Physical Sciences Division (NOAA) and the International Research Institute for Climate and Society (Columbia University) for providing the data used in this research. Fernando Mato discovered the missing link in El Niño's phenomenon generation, conceived research and conducted data processing, Theofilos Toulkeridis enriched the geophysical and climatic analysis. Both authors analyzed and discussed the results and commented on the manuscript. This work has been supported by the Prometeo Project at the National Secretary of Higher Education, Science, Technology and Innovation (SENESCYT), Ecuadorian Government.

REFERENCES

Barazangi M. and Isacks, B.L. (1976). Spatial distribution of earthquakes and subduction of the Nazca plate beneath South America: Geology, v. 4, p. 686-692.

Berninghausen, W.H., 1962. Tsunamis reported from the west coast of South America 1562-1960. Bull. of the Seismological Soc. of America, 52 (4): 915-921.

Ashok, K., Behera, S. K., Rao, S. A.,Weng, H., and Yamagata, T.: El Niño Modoki and its possible teleconnection, J. Geophys. Res.: Oceans (1978-2012), 112, 2007.

Bath, M.: Correlation between regional and global seismic activity, Tectonophysics, 104, 187-194, 1984.

Bjerknes, J.: Atmospheric teleconnections from the equatorial pacific 1, Mon. Weather Rev., 97, 163-172, 1969.

Capotondi, A., Wittenberg, A. T., Newman, M., Lorenzo, E. D., Yu, J. Y., Braconnot, P., Cole, J., Dewitte, B., Giese, B., Guilyardi, E., Jin, F. F., Karnauskas, K., Kirtman, B., Lee, T., Schneider, N., Xue, Y., and Yeh, S.W.: Understanding ENSO diversity, B. Am. Meteorol. Soc., 2014.

Cobb, K. M., Westphal, N., Sayani, H. R., Watson, J. T., Di Lorenzo, E., Cheng, H., Edwards, R. L., and Christopher, D. C.: Highly variable El Niño-Southern Oscillation throughout the Holocene, Science, 339, 67-70, 2013.

Cooper, G. R. J. and Cowan, D. R.: Comparing time series using wavelet-based semblance analysis, Comput. Geosci., 34, 95-102, 2008.

Emile-Geay, J., Seager, R., Cane, M. A., Cook, E. R., and Haug, G. H.: Volcanoes and ENSO over the past millennium, J. Climate, 21, 3134-3148, 2008.

French, S., Lekic, V., and Romanowicz, B.:Waveform tomography reveals channeled flow at the base of the oceanic asthenosphere, Science, 342, 227-230, 2013.

French, S.W. and Romanowicz, B.: Broad plumes rooted at the base of the Earth's mantle beneath major hotspots, Nature, 525, 95-99, 2015.

Guillas, S., Day, S. J., and McGuire, B.: Statistical analysis of the El Niño-Southern Oscillation and sea-floor seismicity in the eastern tropical Pacific, Philos. T. Roy. Soc. A, 368, 2481-2500, 2010.

Kessler, W. S.: Is ENSO a cycle or a series of events?, Geophys. Res. Lett., 29, 40-1, 2002.

Kintisch, E.: How a 'Godzilla' El Niño shook up weather forecasts, Science, 352, 1501-1502, 2016.

Liebmann, B.: Description of a Complete (Interpolated) Outgoing Longwave Radiation Dataset, B. Am. Meteorol. Soc., 77, 1275-1277, 1996.

Luttrell, K. and Sandwell, D.: Ocean loading effects on stress at near shore plate boundary fault systems, J. Geophys. Res.-Sol. Ea. (1978-2012), 115, 2010.

Marzocchi, W., Selva, J., Piersanti, A., and Boschi, E.: On the long-term interaction among earthquakes: Some insight from a model simulation (1978-2012), J. Geophys. Res.-Sol. Ea., 108, 2003.

Marzocchi,W., Zaccarelli, L., and Boschi, E.: Phenomenological evidence in favor of a remote seismic coupling for large volcanic eruptions, Geophys. Res. Lett., 31, 2004.

McPhaden, M. J., Zebiak, S. E., and Glantz, M. H.: ENSO as an Integrating Concept in Earth Science, Science, 314, 1740-1745, 2006.

Molchanov, O.: About climate-seismicity coupling from correlation analysis, Nat. Hazard. Earth Sys., 10, 299-304, 2010.

Mukhin, D., Gavrilov, A., Feigin, A., Loskutov, E., and Kurths, J.: Principal nonlinear dynamical modes of climate variability, Sci. Rep., 5, 15510, 2015.

Philander, S. G. and Fedorov, A. V.: Is El Niño sporadic or cyclic?, Annu. Rev. Earth Pl. Sc., 31, 579-594, 2003.

Qin, D., Plattner, G. K., Tignor, M., Allen, S. K., Boschung, J., Nauels, A., and Midgley, P. M.: Climate change 2013: The physical science basis, Cambridge University Press, Cambridge, UK, and New York, 2014.

Rasmusson, E. M. and Carpenter, T. H.: Variations in tropical sea surface temperature and surface wind fields associated with the Southern Oscillation/El Niño, Mon. Weather Rev., 110, 354-384, 1982.

Robock, A.: Volcanic eruptions and climate, Rev. Geophys., 38, 191-219, 2000.

Shaw, H. R. and Moore, J. G.: Magmatic heat and the El Niño cycle, EOS, Trans. Amer. Geophys. Union, 69, 1553-1565, 1988.

Takahashi, K., Montecinos, A., Goubanova, K., and Dewitte, B.: ENSO regimes: Reinterpreting the canonical and Modoki El Niño, Geophys. Res. Lett., 38, 2011.

Walker, D. A.: Seismicity of the 5 East Pacific Rise: correlations with the southern oscillation index?., Eos, Trans. Amer. Geophys. Union, 69, 857-867, 1988.

Walker, D. A.: More Evidence Indicates Link between El Niños and Seismicity, EOS, Trans. Amer. Geophys. Union, 76, 33-36, 1995.

Walker, D. A.: Seismic predictors of El Niño revisited, EOS, Trans. Amer. Geophys. Union, 80, 281-285, 1999.

Walker, G. T. and Bliss, E. W.: World weather, V. Mem. Roy. Meteor. Soc., 4, 53-84, 1932.

Wolter, K. and Timlin, M. S.: Measuring the strength of ENSO events: how does 1997/98 rank?, Weather, 53, 315-324, 1998.

Yeh, S. W., Kug, J. S., Dewitte, B., Kwon, M. H., Kirtman, B. P., and Jin, F. F.: El Niño in a changing climate, Nature, 461, 511-514, 2009.

ISSN 8755-6839

SCIENCE OF TSUNAMI HAZARDS

Journal of Tsunami Society International

Volume 36 Number 3 2017

MANIFESTATION OF THE 1963 URUP TSUNAMI ON SAKHALIN: OBSERVATIONS AND MODELING

Andrey Zaytsev[1,2], Irina Kostenko[1], Andrey Kurkin[2,3], Efim Pelinovsky[2,4,5]
& George Pararas-Carayannis [6]

1) Special Research Bureau for Automation of Marine Researches, Yuzhno-Sakhalinsk, Russia
2) Nizhny Novgorod State Technical University n.a. R. Alekseev, Nizhny Novgorod, Russia
3) Institute of Space Technologies, Peoples' Friendship University of Russia (RUDN University), Moscow, Russia
4) Institute of Applied Physics, Nizhny Novgorod, Russia
5) National Research University – Higher School of Economics, Moscow, Russia
6) Tsunami Society International, Honolulu, Hawaii, USA.

ABSTRACT

In the history of instrumental observations, the tsunami of 1963 generated in the vicinity of Urup in the Kuril Islands had the highest runup heights on the coasts of Sakhalin Island. It was generated by a strong earthquake which had a moment magnitude M_w 8.1. The present study summarizes the known observations of this event along the coasts of Sakhalin, in the Hawaiian Islands and elsewhere in the Pacific Ocean. Additionally, the prestent study includes the numerical simulation of this 1963 tsunami event in the framework of nonlinear shallow water theory. The results of the numerical calculations are in good agreement with the observational data.

1. INTRODUCTION

Sakhalin Island is located in the Sea of Okhotsk, which is in the northwestern part of the Pacific Ocean and is connected to the Pacific Ocean by the straits of the Kuril Islands (Fig. 1). The width of the Kuril Islands is about 500 km and the length is about 1200 km, which is 41.6% of the total distance between the Kamchatka Peninsula and the island of Hokkaido. The Pacific and the Kuril Islands are located along a strong seismic activity zone where major and great earthquakes occur, and which can generate destructive tsunamis across the Pacific Ocean basin. Tsunamis originating from distant Pacific sources upon entering the Sea of Okhotsk become weakened due to the shielding effect of the Kuril Islands (Kostenko et al, 2016, Shevchenko et al., 2011). On the other hand, earthquakes originating in the Sea of Okhotsk and the Sea of Japan can generate tsunamis which can impact significantly the Island of Sakhalin. It should be noted that the network of tide gauges established along coastal areas of Sakhalin Island, have provided valuable historical data of tsunamis for the last 60 years. For that period, a total of about 30 tsunamis were recorded. (Kostenko et al, 2015, Zaytsev et al., 2017). The magnitudes of earthquakes that have generated tunamis on Sakhalin over the past 100 years, usually exceed M_s 6.1, while maximum magnitudes exceeded $M_s = 9$ for two events (Chile, 1960 and Japan, 2011).

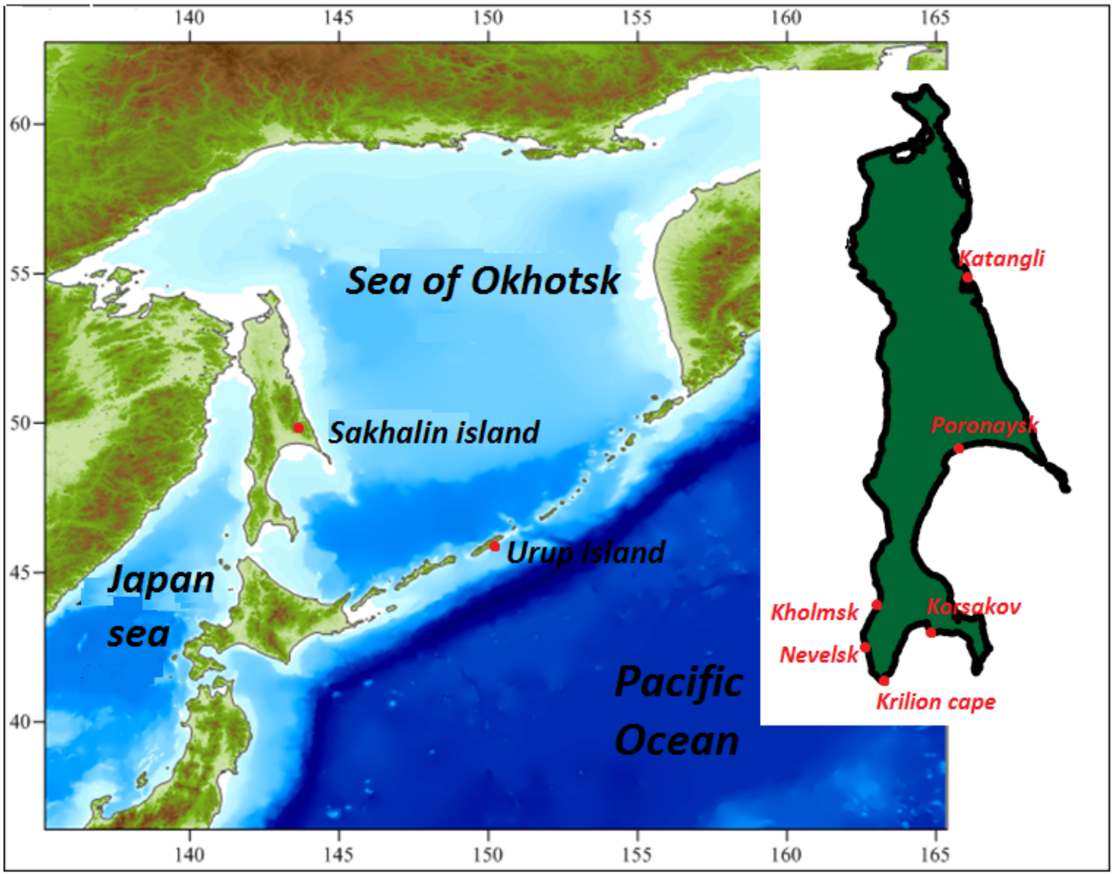

Figure 1. Sakhalin Island

Inpite of the fact that in the Far Eastern region earthquakes with magnitudes of more than M_s 8 over the past 100 years have occurred, there has been no catastrophic tsunami with losses of human lives on Sakhalin Island. However, though the maximum tsunami height did not exceed 2-3 m for these large events, such runup heights were sufficient to cause damage on Sakhalin's infrastructure. For example, during the Nevel earthquake of August 2, 2007 (magnitude $M = 6.2$), the seabed rose, so it became necessary to rebuild the port (Zaitsev et al, 2008, 2009). Fig. 2 shows the location of tsunami sources that have been detected on Sakhalin Island over the past 300 years. The figure identifies the main areas of tsunami generation. Most of the sources were located relatively close to Sakhalin, along the northern and eastern part of the Sea of Japan or along the Pacific coast of the southern and central Kuril Islands. For example, the severe earthquake of March 11, 2011, east of Honshu Island in Japan, caused not only a devastating tsunami in Japan and elsewhere in the Pacific but also led to the destruction of the coastal ice field in the Kuril Islands (Kaistrenko et al, 2013).

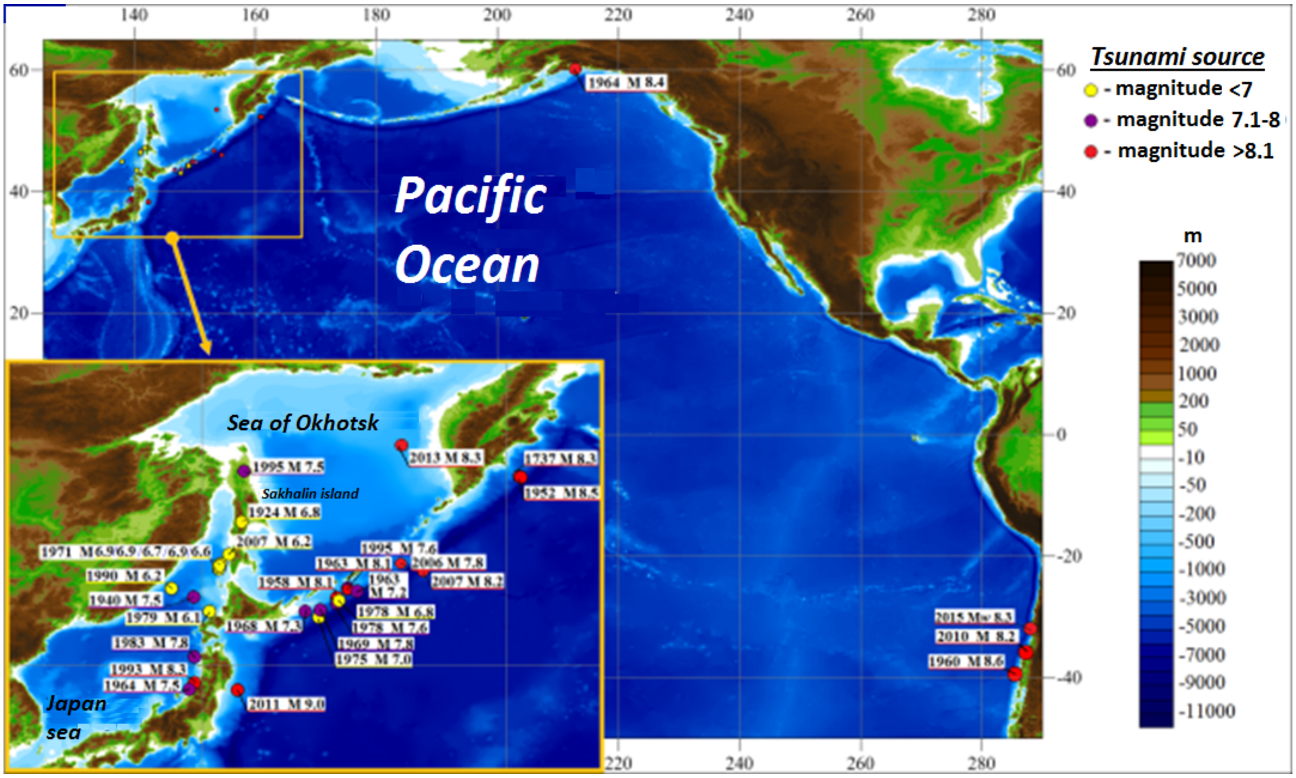

Figure 2. Epicenters of earthquakes that caused tsunami, which manifested themselves on the coast of Sakhalin

In summary, the Kuril Islands can be impacted not only from tsunamis generated from distant sources, but also from locally generated events. The strongest impact on Sakhalin was caused by the tsunami generated by the earthquake of October 13, 1963 at 05:17:51 (Greenwich Mean Time) near the area of Urup Island (Fig. 1)(. The moment magnitude (M_w) of this earthquake was estimated to be 8.1, (but according to some data, it may have been as much as $M_w = 8.5$). The tsunami source area was near the wider straits of Vries and Bussol, thus contributing to a greater amount of tsunami energy entering the Sea of Okhotsk. The present study presents a discussion of the 1963 Urup tsunami observations on Sakhalin Island and elsewhere, as well as to the numerical modeling of this event.

2. TECTONIC SETTING OF THE KURIL ISLAND REGION

In order to understand the generation of tsunamigenic earthquakes near the Kuril Islands and the Sea of Okhotsk, there is a need for a brief review of the seimo-tectonics of the region. This is necessary as the overall tectonics of northeast Asia are very complicated and not sufficiently understood. For example, it has not been determined with certainty whether the Sea of Okhotsk and the northern Japanese islands are part of the North American plate or of a separate Okhotsk tectonic plate. On the Pacific Ocean side, earthquake slip vectors along the Kuril and Japan trenches are consistent with either a Pacific-North America or a Pacific-Okhotsk plate motion. However, it has been concluded that the Pacific-North America plate motion is better supported (Pararas-Carayannis, 1994, 2006).

Furthermore, the volcanic Kuril island arc chain runs from the northern tip of the Japanese Island of Hokkaido to the southern tip of Russia's Kamchatka Peninsula. It is also a region of high seismic activity. The Kuril Trench has been formed by the subduction of the Pacific plate under the North American plate and extends from the offshore central area of Kamchatka to Hokkaido.

The plate tectonics of the Southern Kuril islands-Northern Hokkaido region are also quite different than those along the southern portion of the Japanese Trench. The South Kuril Islands are part of the Kuril arc in the Okhotsk plate which has been colliding westward against the Northeast Japan arc, along the Hidaka Collision Zone (HCZ), where new continental crust is created by active arc-arc collision (Pararas-Carayannis, 1994, 2006).

Also, deep seismic reflection studies (Ito, Kazuka @Abe, 2001) show the lower crust of the Kuril arc to be delaminated at a depth of about 23 km. These studies indicate that the upper half (above 23 km) - consisting of the earth's upper crust and the upper portion of lower crust of the Kuril arc - is thrusting over the Northeast Japan arc along the Hidaka Main Thrust (HMT). However, the lower half (below 23 km) - consisting of the lower portion of lower crust and upper mantle material - is descending downward (Pararas-Carayannis, 1994, 2006).

As a result of such kinematic processes, the wedge of the Northeast Japan arc is intruded into the delaminated Kuril arc, as the Pacific plate is subducting northward beneath both of the above mentioned structures, thus continuing the arc-arc collision (and continental crust production). The complex, seismo-tectonic kinematic process of this region has been named "Delamination-wedge-subduction system" - which may apply also to other areas where active arc-arc collision and concurrent subduction take place (Pararas-Carayannis, 2006).

This region of the southern Kuril Islands is characterized by crustal displacements which appear to be ocurring along the boundaries of broken subplates that may not be longer than 200-250 km. The Kuril

Back-Arc basin is a deep basin in southern Sea of Okhotsk, northwest of the Kuril Arc. These fractured smaller plates, near this tectonically active arc-arc collision area, appear to limit the extent of crustal ruptures and therefore the areal extent of tsunami sources. This is the reason why large magnitude earthquakes in this region have generated only locally destructive and not Pacific-wide – tsunamis (Pararas-Carayannis, 1994, 2006).

Specifically, the October 12, 1963 earthquake (as that of October 4, 1994) which ocurred at the Pacific side boundary of the Kuril Arc (near the South Kuril Islands) of the Okhotsk plate. but with lesser vertical subduction and greater rotational movement - as the North Pacific Plate grinds against it. The whole area appears to be highly fractured by complex tectonic interactions and the crustal displacements appear to be ocurring along the boundaries of broken subplates – which as mentioned - may not be longer than 200-250 Km.

3. HISTORICAL DATA ON THE 1963 URUP TSUNAMI

Historical data on tsunami are given in a number of papers (Solovyev, 1965, 1978, Iida et.al, 1967; Pararas-Carayannis, 1968; Pararas-Carayannis & Calebaugh, 1977; Shchetnikov, 1981, 1990; Shevchenko et al., 2012). Tsunami warnings for the Pacific were issued by what was then known as the U. S. Seismic Sea Wave Warning System operated by the Honolulu Observatory in Hawaii for this event and for another potentially tsunamigenic earthquake (Ms 7) near Iturup in the Kurils, a week later (Pararas-Carayannis, 1968; Pararas-Carayannis & Calebaugh, 1977). The earthquake of 13 October, 1963 had a magnitude of 8.1 and occurred at 06:17:51 GMT. The coordinates of the epicenter were 44.81^0N and 149.54^0 (it was on a continental slope near the island of Urup); the focal depth is 47 km.

According to the Urup hydro-meteorological station observations, the tsunami began with the level lowering (the drainage zone was 70-80 m), then came the first wave 2-3 m high. After it a more significant low tide followed, and the drainage region was 400-500 m. The second wave was the most dangerous. Its height, according to the hydrostatic logger in Nevidimka Bay, was 4.4 m. In total, five large waves were observed with an interval of 12-15 minutes, and then the tsunami intensity gradually decreased. The tsunami manifested itself mainly on the Pacific coast of the islands of Urup and Iturup, but also caused quite dangerous fluctuations in sea level in Shikotan, Kunashir (up to 1.5 m), and also on the islands of the Lesser Kuril ridge. On the Middle and Northern Kuril Islands the tsunami was quite intense (about 1 m in height), but it was not dangerous. The tsunami of October, 13 caused significant economic damage to the Kuril Islands facilities (Solovyov, 1965, 1978; Shevchenko et al., 2012). For instance, in the bays of the island of Shikotan several ships were stranded (height up to 2.5 m, current speed up to 10 knots). In many whaling plants on the islands of Urup, Simushir and Iturup the tsunami carried into the sea many tons of coal, fuel and containers.

This tsunami was registered in Japan (maximum height 0.6 m, the tsunami began with a tidal wave), in the Hawaiian Islands (max height up to 0.4 m in Kahului, Island of Maui), in the Aleutian Islands (the height did not exceed 0.4 m), in California (0.5 m) and Mexico (0.7 m) (Iida et.al, 1967; Pararas-Carayannis, 1968; Pararas-Carayannis & Calebaugh, 1977).

On the coast of Sakhalin the tsunami came weakened and the wave heights did not exceed 0.4m (see Table 1), according to observations (the town of Korsakov, Cape Krilion, Katangli settlement). Instrumental ("paper") data on the Sakhalin tsunami recording are shown in Fig. 3. As can be seen, the tsunami waves caused many hours of water level fluctuations, with the first wave not being the maximum.

Table1. The Urup tsunami observations on Sakhalin

Location	Wave height, m	Travel time, hr	Period, min
Katangli	0.4	2.8	23
Poronaisk	0.3	3.3	30
Korsakov	0.4	2.3	25
Cape Krillion	0.4	2.3	8
Nevelsk	0.15		
Kholmsk	0.1		

A week later, on October 20, was recorded the strongest earthquake aftershock with a magnitude of 7.4. A very strong tsunami (up to 15m in height) was observed directly opposite the focus (CapeVan-der-Lind, Urup), outside this zone the wave heights were small. A unique photograph of the tsunami wave which moves down from the coast in Yuzhno-Kurilsk (Kunashir Island) is shown in Fig. 4; the wave height in this bay did not exceed 0.5m.

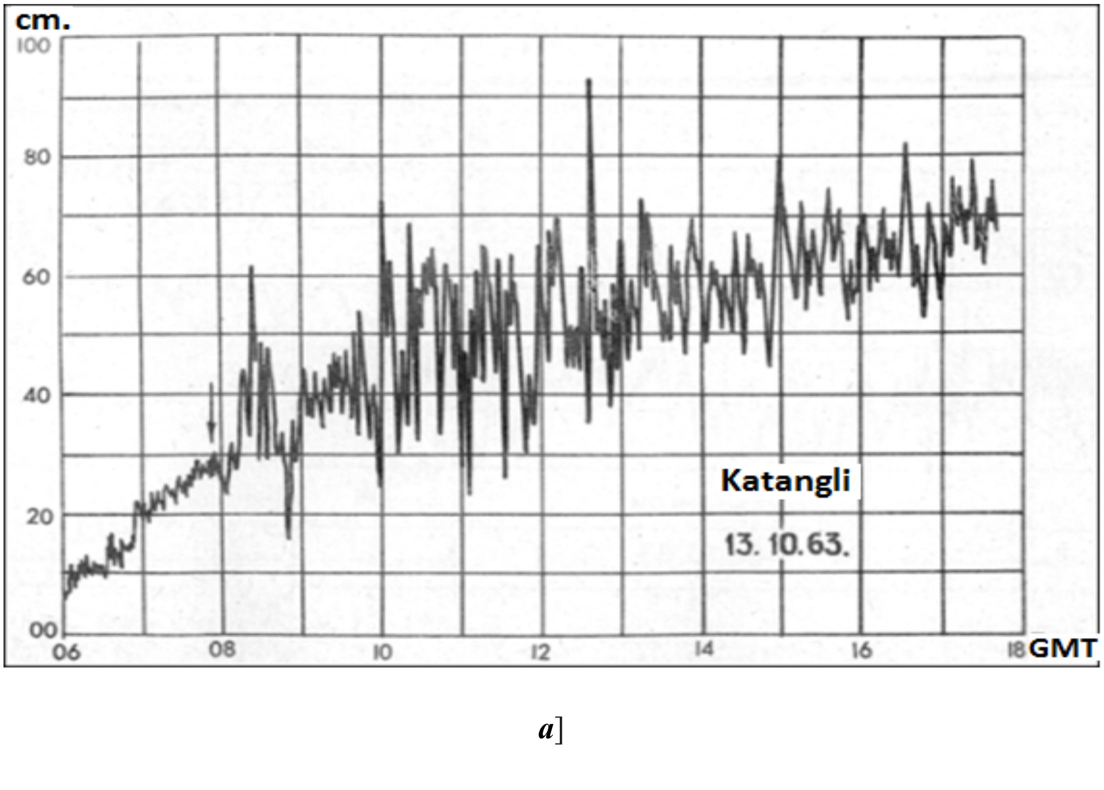

a]

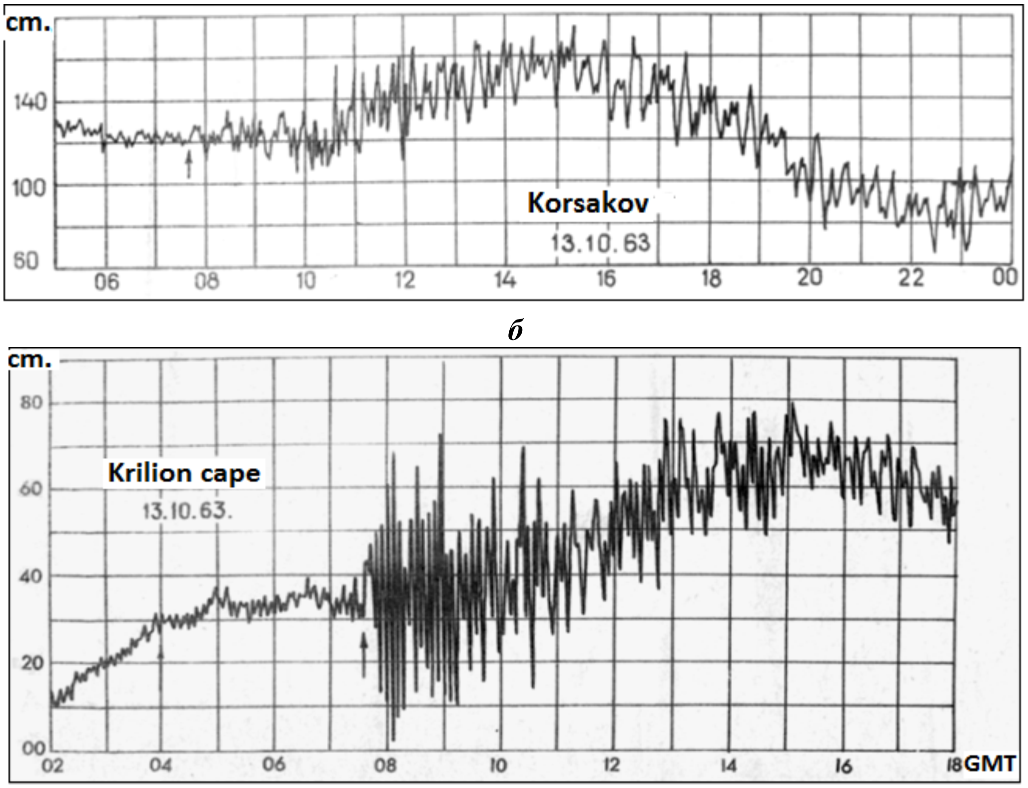

б

в

Figure 3. Records of the October 13, 1963 tsunami on Sakhalin (*a* - Katangli, *b* - Korsakov, *c* - Cape Krilion) [Schetnikov, 1981, 1990].

Figure 4.The tsunami wave moves down in Yuzhno-Kurilsk, Kunashir Island on October 20, 1960 (courtesy S.L. Solovyev)

4. MATHEMATICAL MODEL OF THE 1963 TSUNAMI PROPAGATION

Tsunami waves of seismic origin are long waves (the wavelength exceeds the ocean depth), so the based model is the famous non-linear shallow-water theory described by a system of equations, which take into account the sphericity of the Earth, the Coriolis force and the bottom friction (Pelinovsky, 1996, Levin and Nosov, 2016)

$$\frac{\partial M}{\partial t}+\frac{1}{R\cos\theta}\frac{\partial}{\partial\lambda}\left(\frac{M^2}{D}\right)+\frac{1}{R\cos\theta}\frac{\partial}{\partial\theta}\left(\frac{MN\cos\theta}{D}\right)+\frac{gD}{R\cos\theta}\frac{\partial\eta}{\partial\lambda}+\frac{gn^2}{D^{7/3}}M\sqrt{M^2+N^2}=f\,N \quad (1)$$

$$\frac{\partial N}{\partial t}+\frac{1}{R\cos\theta}\frac{\partial}{\partial\lambda}\left(\frac{MN}{D}\right)+\frac{1}{R\cos\theta}\frac{\partial}{\partial\theta}\left(\frac{N^2\cos\theta}{D}\right)+\frac{gD}{R}\frac{\partial\eta}{\partial\theta}+\frac{gn^2}{D^{7/3}}N\sqrt{M^2+N^2}=-f\,M \quad (2)$$

$$\frac{\partial\eta}{\partial t}+\frac{1}{R\cos\theta}\left[\frac{\partial M}{\partial\lambda}+\frac{\partial}{\partial\theta}\left(N\cos\theta\right)\right]=0\,, \quad (3)$$

where η is the sea level displacement with regard to the unperturbed one; *M* and *N* are discharge components along latitude λ and longitude θ; *D* is the basin total depth; *g* is the gravity acceleration, *R* is the Earth radius, *f* is the Coriolis parameter ($f = 2\omega\, sin\theta$), ω is the Earth rotation frequency (rotation period of 24 hours), and *n* is the bottom roughness coefficient. In the calculations, the value $n = 0.015$ $m^{-1/3}s$, typical for the natural bottom (sand, small pebbles) is used. The total basin depth of is defined as:

$$D(\lambda,\theta,t)=h(\lambda,\theta)+\eta(\lambda,\theta,t) \quad (4)$$

,

where *h* is the unperturbed ocean depth, assumed to be known and not changing in time. The bathymetry, created from GEBCO Digital Atlas with a 30 arc second resolution, was used in the calculations[http://www.gebco.net].

The initial conditions correspond to the instantaneous bottom movement

$$\eta(\lambda,\theta,t=0)=\eta_0(\lambda,\theta)\ .\ M(\lambda,\theta,t=0)=N(\lambda,\theta,t=0)=0 \quad . \quad (5)$$

The function $\eta_0\ (\lambda,\theta)$ is found by Okada's solution [Okada, 1985], which determines the residual displacements of the earth surface after the earthquake. This solution is too cumbersome to be given here. It is important to note that the following earthquake parameters are necessary to know for its calculation: fault depth, length (L) and width (W), vertical displacement (D), strike angle (θ), dip angle (δ), slip (rake) angle (λ) - Fig. 5.

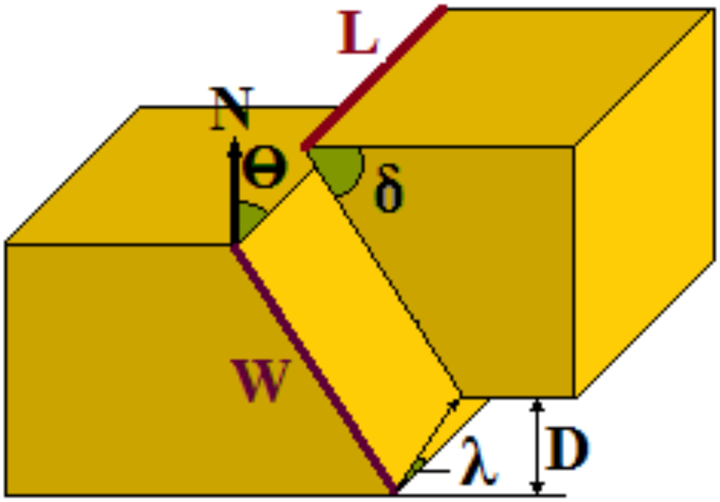

Figure 5.The earthquake parameters

The boundary conditions on the free (sea) boundaries of the computational domain assume the Sommerfeld radiation condition:

$$M_n = \eta\sqrt{gD} \qquad (6)$$

where M_n is the normal component of discharge(obviously, this condition requires the smoothness of the computational domain boundary). This condition is exact for shallow water equations ignoring the Coriolis force (the Earth rotation) and the bottom friction. These factors lead to a weak wave reflection from the sea wall and can influence the results of wave parameter calculations at large times when the wave amplitude becomes sufficiently small. In our calculations, the sea boundaries are used in the Pacific to reduce computation time. The sea boundaries are also used in nested grids for calculations in the vicinity of Sakhalin.

The boundary condition on the moving shore is used on the solid walls (coast)

$$. \qquad D(\lambda,\theta,t) = 0 \qquad (7) \qquad .$$

The NAMI DANCE code of shallow-water equations is used to compute tsunami propagation [http://avi-nami.ce.metu.edu.tr]. It has already been used to model various historical tsunamis [Zaitsev et al., 2005, 2009; Kurkin et al, 2004; Yalciner et al., 2007, 2010; Baranova et al, 2014; Dilmen et al., 2014; Ozer et al. 2015; Zaytsev et al, 2016]. The shallow water equations are solved by a finite-difference method [Shuto et al., 1990; Imamura, 1989]). The NAMI DANCE code includes a subroutine for calculating a tsunami source using Okada formula. It makes it possible to calculate tsunami wave propagation in the water area; wave propagation time and velocity, wave and runup heights, as well as power characteristics [Ozer et al, 2015].The complex control panel view is shown in Fig. 6. The calculation speed depends on the computer capabilities, the step size and other parameters that are set at the start of the calculation.

To compare the numerical results with the observation data, 'computer' tide gauges are located in places closest to the sea level measurement points of the Russian Tsunami Warning Service on Sakhalin Island and the Kuril Islands [http://www.rtws.ru/]. However, they are always located in the open sea, while the real tide gauges are installed in harbor bays, which, in turn, can affect the height and characteristic periods of sea level fluctuations due to resonant (seiche) effects. In general, the bathymetry of the near-shore zone is not set well enough; it does not include port and coastal structures. Therefore, tsunami runup assessments are quite rough for settlements where ports, fish plants and other industrial and civil structures are located.

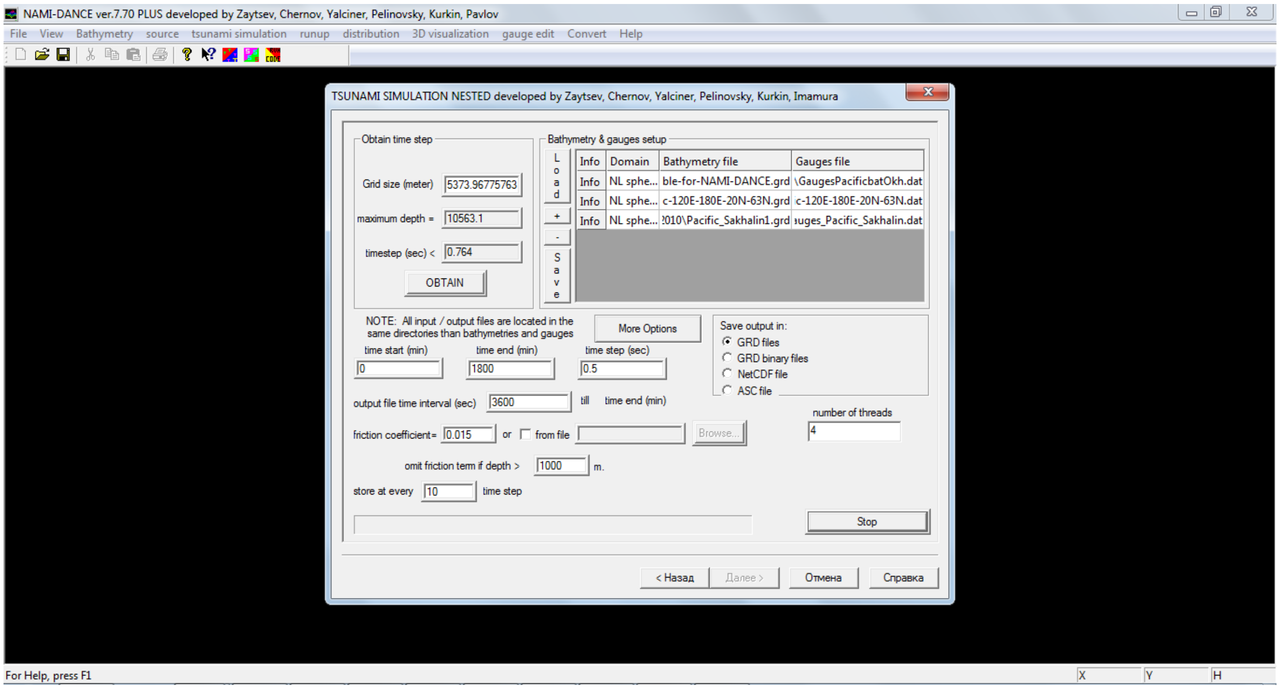

NAMI-DANCE ver.7.70 PLUS developed by Zaytsev, Chernov, Yalciner, Pelinovsky, Kurkin, Pavlov

TSUNAMI SIMULATION NESTED developed by Zaytsev, Chernov, Yalciner, Pelinovsky, Kurkin, Imamura

Obtain time step

Grid size (meter) 5373.96775763

maximum depth = 10563.1

timestep (sec) < 0.764

Bathymetry & gauges setup

Info	Domain	Bathymetry file	Gauges file
Info	NL sphe...	ble-for-NAMI-DANCE.grd	\GaugesPacificbatOkh.dat
Info	NL sphe...	c-120E-180E-20N-63N.grd	c-120E-180E-20N-63N.dat
Info	NL sphe...	2010\Pacific_Sakhalin1.grd	auges_Pacific_Sakhalin.dat

NOTE: All input / output files are located in the same directories than bathymetries and gauges

time start (min) 0

time end (min) 1800

time step (sec) 0.5

Save output in:
● GRD files
○ GRD binary files
○ NetCDF file
○ ASC file

output file time interval (sec) 3600 till time end (min)

number of threads 4

friction coefficient= 0.015 or ☐ from file

omit friction term if depth > 1000 m.

store at every 10 time step

Figure 6. NAMI DANCE complex control panel

5. NUMERICAL MODELING OF THE 1963 URUP TSUNAMI

The results of the 1963 Urup tsunami numerical modeling and its manifestations on the Coast of Sakhalin Island are presented here. It should be reminded that the earthquake had a magnitude of 8.1 (according to some data, $Mw = 8.5$). The tsunami that was formed as a result of the earthquake, struck the coast of the Kuril Islands with a wave height of about 4 m, and on Sakhalin with a height of 0.4 m. It is an example of one of the most powerful tsunamis that occurred on the Pacific coast of the Kuril Islands during the instrumental measurement period. The tsunami source was located on the Pacific side of Urup near the Vries and Bussol Straits, which contributed to a greater tsunami wave penetration into the Sea of Okhotsk. It was this tsunami that had the strongest impact on Sakhalin.

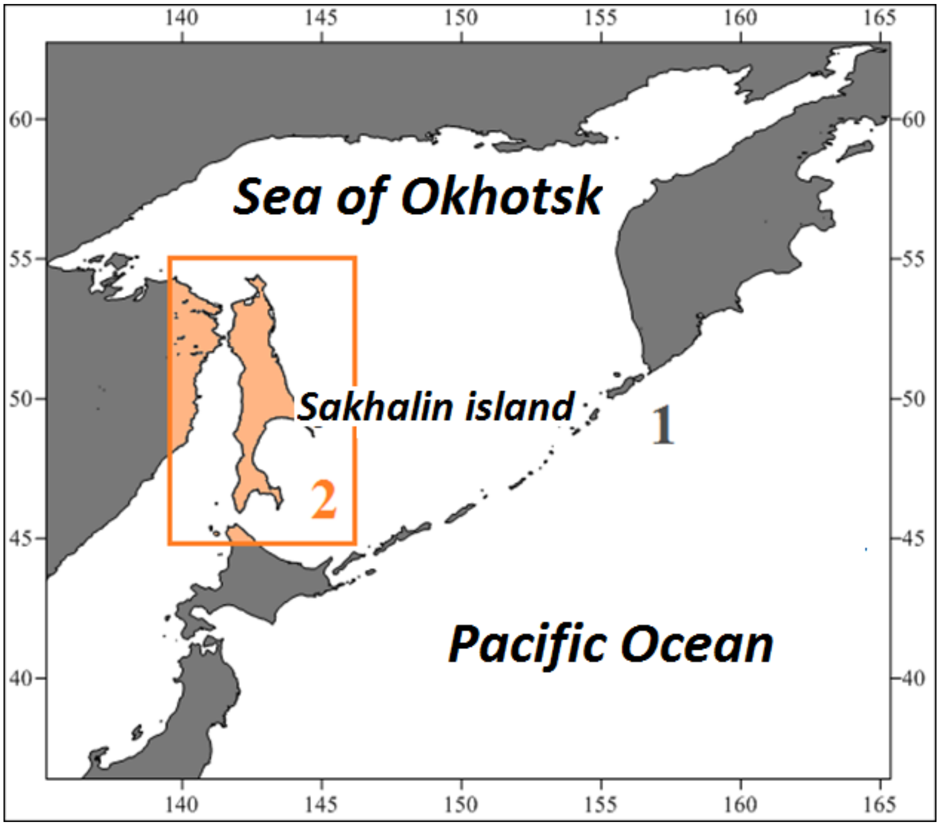

Figure 7. 'Embedded' bathymetry used for numerical calculation (**1**- the northwestern area of the Pacific, **2** - the Sakhalin Island region)

Since the tsunami source was located relatively near the coast of Sakhalin, there is no need to calculate tsunami waves throughout the entire Pacific Ocean. The average distance between the nodes of the bathymetry grid in the northwestern Pacific is 690 (541-839) m (Fig. 7). The grid spacing of the 'embedded' bathymetry in the vicinity of Sakhalin is 229 (179-279) m.

The 1963 earthquake characteristics are taken from [Ioki and Tanioka, 2008]. They are presented in Table 2.

Table2. October 13, 1963 earthquake parameters

Epicenter coordinates	151,8^{0}E 44,763^{0}N
Focal depth (km)	26
Fault length (km)	250
Fault width (km)	150
Strike angle	223
Dip angle	22
Rake angle	90
Displacement (m)	3

Calculated by the Okada formula [Okada, 1985], the tsunami source is shown in Fig. 8. The water rise in the source was 1.4 m, and the descent was 0.3 m, so that the water level difference (height) in the source was 1.7 m.

The simulation was to last 10 operation hours, enough for the wave to propagate in the Sea of Okhotsk. The numerical results were verified on the basis of tsunami observation data in the Kuril Islands, which we omit here.

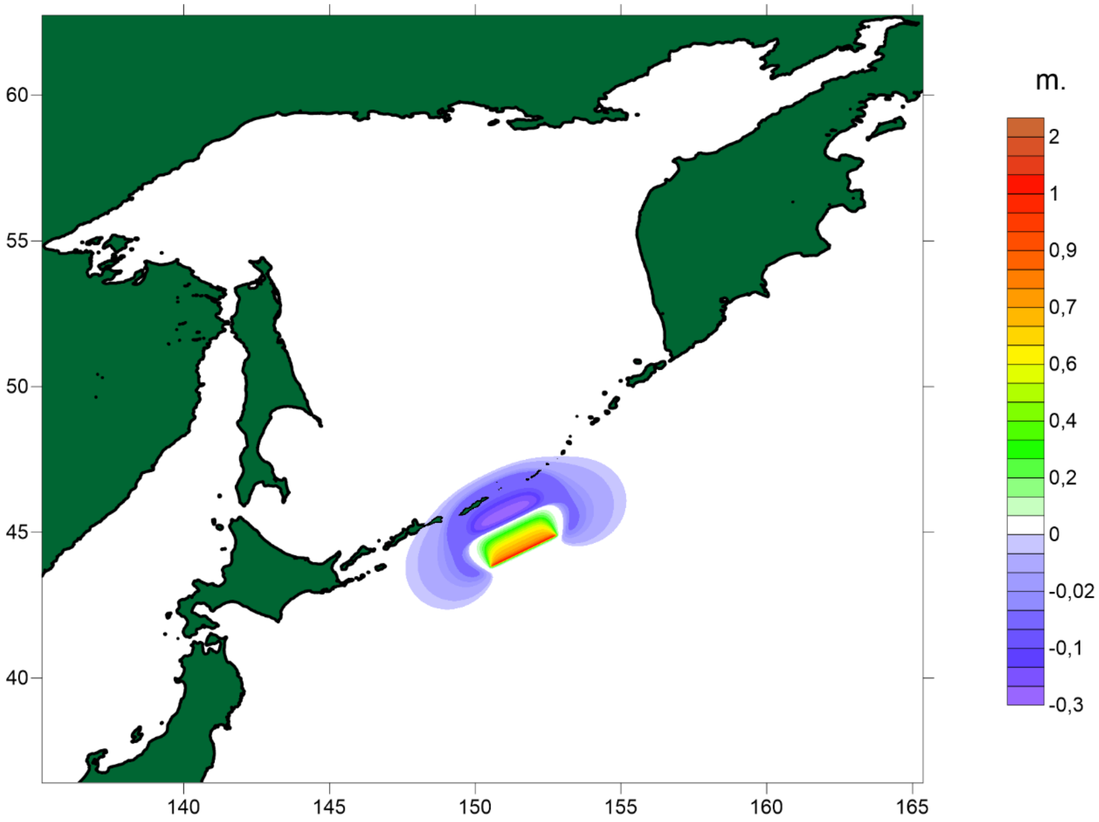

Figure 8. The computed tsunami source

Fig. 9 shows the spatial distribution of the tsunami amplitude for the entire calculation area. It is seen, as expected, that the bulk of the tsunami energy is in the Pacific Ocean where it is dispersed. In the Kuril Islands the largest amplitudes according to numerical calculation results are from the Pacific side in the vicinity of the source and large islands. In the Sea of Okhotsk, there are three areas where tsunamis most intensively manifested themselves: the Sakhalin southern and eastern coast, the Sea of Okhotsk northern coast and the Kamchatka Peninsula western coast. The same areas of increasing tsunami intensity are also noted for other tsunami events [Kostenko et al, 2015; Zaytsev et al, 2016, 2017]. On the Sakhalin coast, the largest values of tsunami amplitudes were shown on the east and south-east coasts, according to numerical calculations. In the Tatar Strait (the Sakhalin Island western coast) tsunami waves were less intense, especially in the central and northern parts.

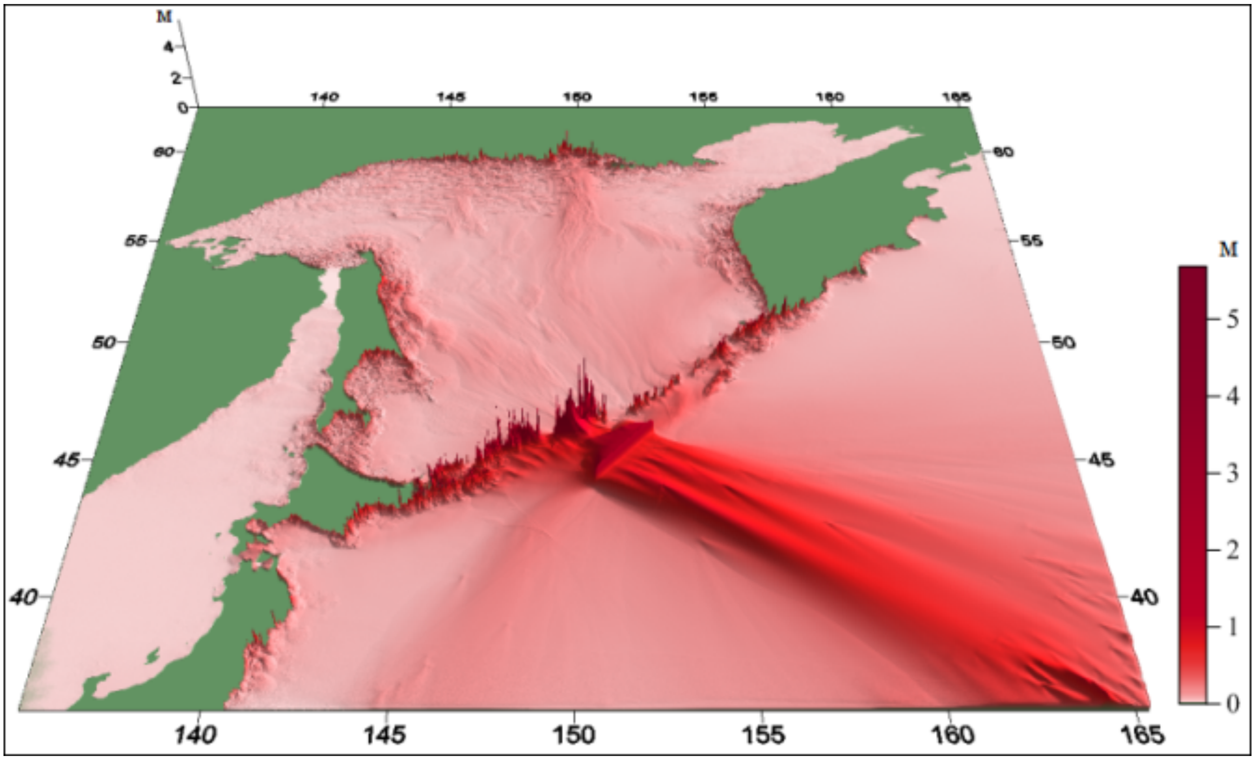

Figure 9. Distribution of the 1963 Urup tsunami maximal wave amplitudes

Let us discuss in more detail the tsunami quantitative characteristics. Fig. 10 shows the maximum value calculated distribution of tsunami amplitudes along the Coast of Sakhalin Island. On the northeastern coast of Sakhalin, according to observations, the tsunami height in the settlement of Katangli was 0.4 m. The maximum values of the tsunami amplitudes are on average 0.2-0.5 m, according to the numerical calculation results. According to observations in Terpeniya Bay in the town of Poronaisk, the tsunami wave height reached 0.3 m. The maximum amplitudes of tsunami wave in Terpeniya Bay and on the Sakhalin southeast coast, according to the numerical calculation results, are in the range 0.2-0.8 m. The highest values of wave amplitudes are on the Tonino-Aniva Peninsula east coast (0.4-0.6 m) and in the upper part of Terpenia Bay (0.7-0.8 m).

According to observations on the western coast of the island, the tsunami manifested itself in Nevelsk (0.15 m) and in Kholmsk (0.1 m), which is consistent with numerical calculations. On the coast of the Tatar Strait, the largest wave amplitudes are found in the south-eastern part of Sakhalin in the area of the Strait of La Perouse, according to the numerical simulation. From there the most part of the waves were hardly manifested themselves, according to the numerical simulation.

On the Sakhalin northern coast the measurements were not carried out, but according to the numerical simulation, the tsunami wave height here did not exceed 0.15 m.

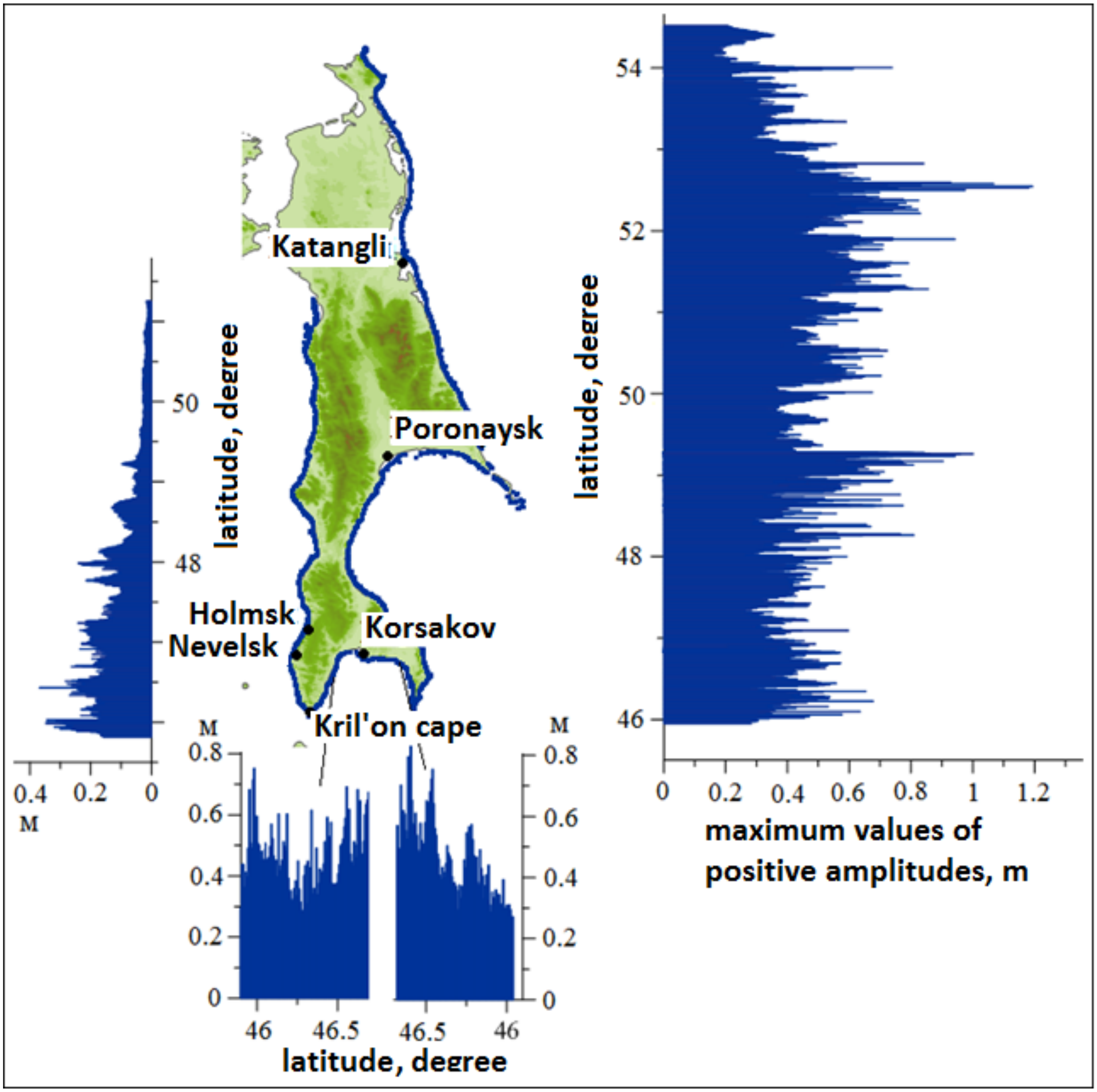

Figure 10. Distribution of the maximum wave amplitudes along the coast of Sakhalin.

Fig. 11 shows travel times of tsunamis of the leading wave (a) and wave of maximal amplitude (b). Tsunami waves approach the south-east coast of Sakhalin 1 hr after earthquake and after 2-3 hrs the wave comes to the main cities of Sakhalin (Poronaisk, Kholmsk). After 10 hrs waves reached all coastal locations on Sakhalin.

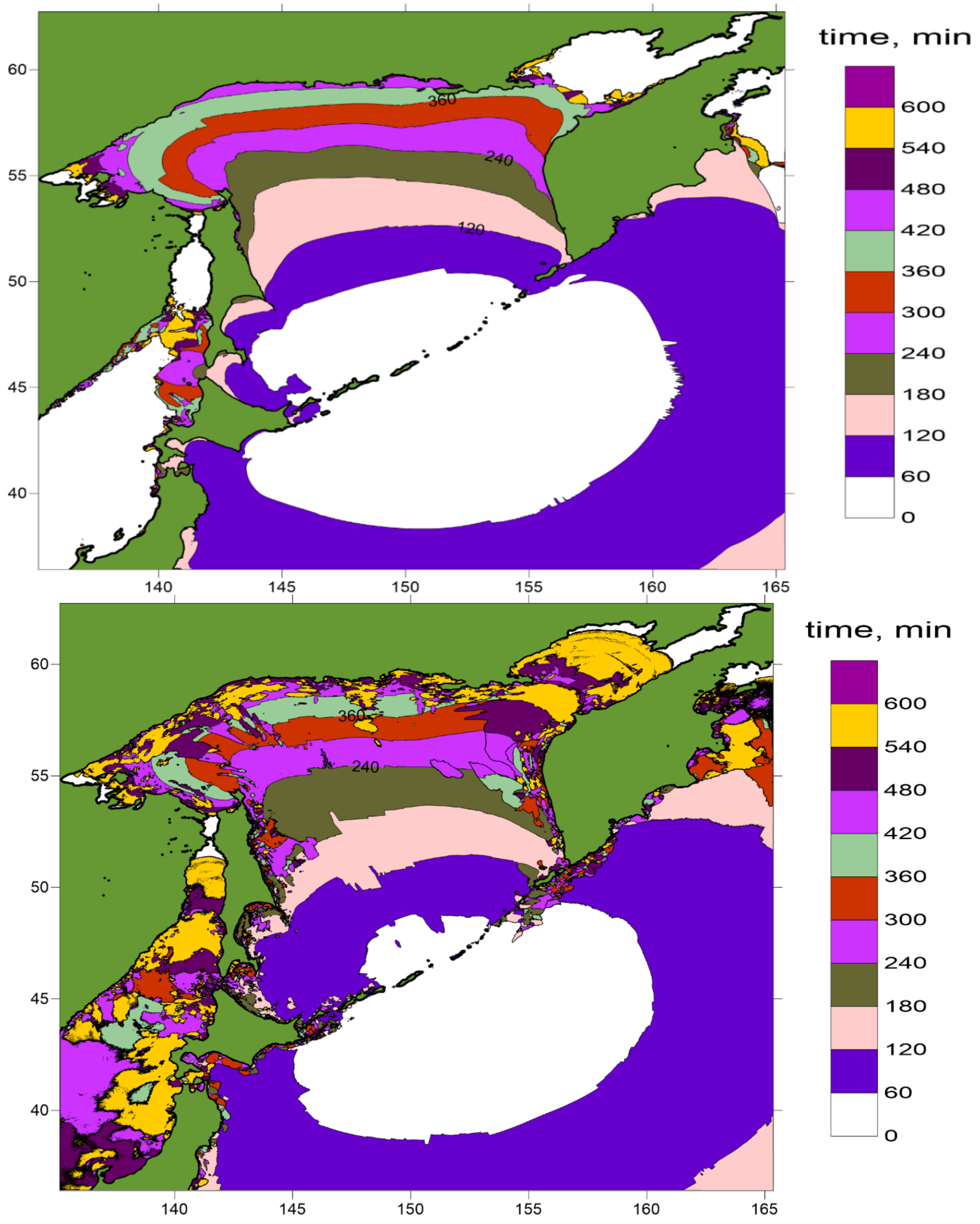

Figure 11. Computed travel time: a) leading wave, b) wave of maximal amplitude

Computed tide-gauge records in several coastal locations where tsunami was recorded are displayed in Fig. 12.

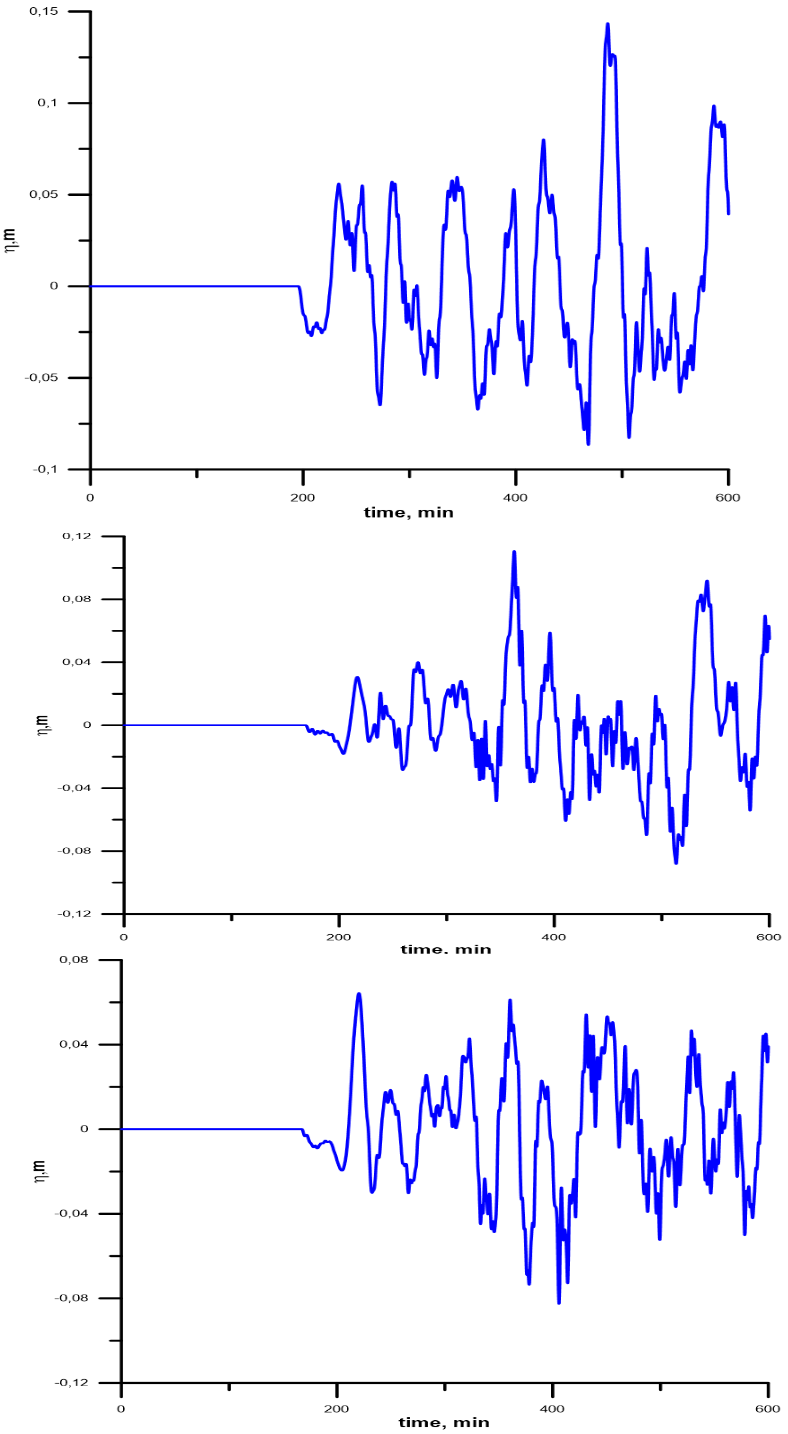

Figure 12. Computed tide gauge records of 1963 tsunami in Katangli (above), Korsakov (middle), and Krilion Cape (below)

According to simulation the tsunami began from the ebb phase. Then the series of large waves in the time period of approximately 5 hrs is clearly visible on mariograms. Let us compare the observed and computed tide gauge records in Katangli (Figs. 3 and 12). Both mariograms begin from the negative wave. The wave of maximal amplitude comes 5 hrs after the earthquake according to both, observation and computation. So, the agreement between mariograms is very good. According to the observations a wave of maximal amplitude arrives in 3 hrs after the earthquake in Korsakov and this corresponds to the computations. On the records in Krilion Cape the wave of maximal amplitude is not clearly selected in both, in observations and computations. So the agreement between observations and computations is quite good.

Similar tide gauge records are computed for some other coastal locations (Fig. 13). Unfortunately, we could not compare here tide gauge records because only visual observations are available for these locations.

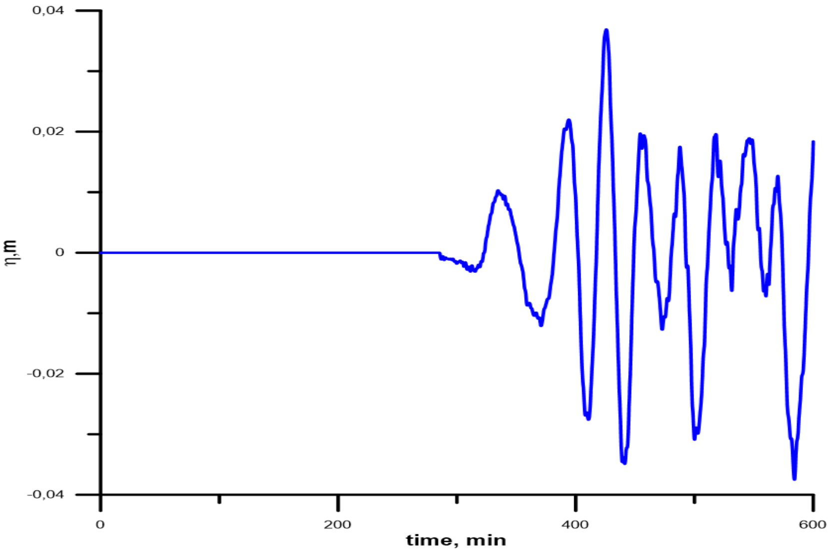

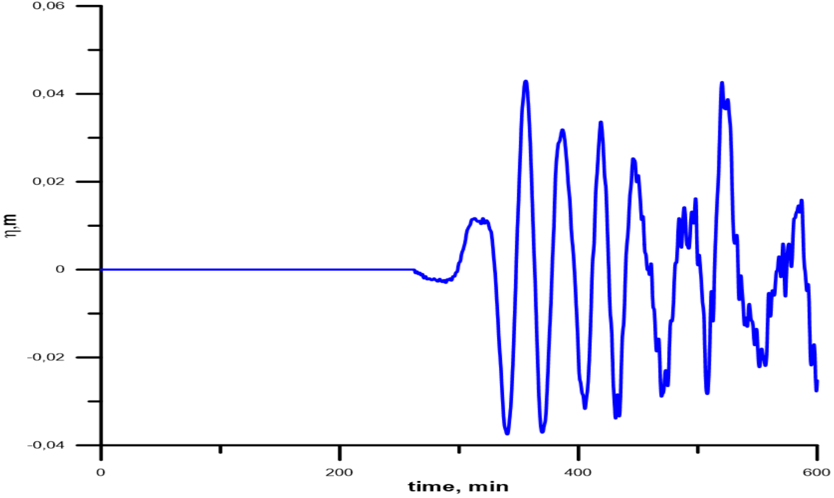

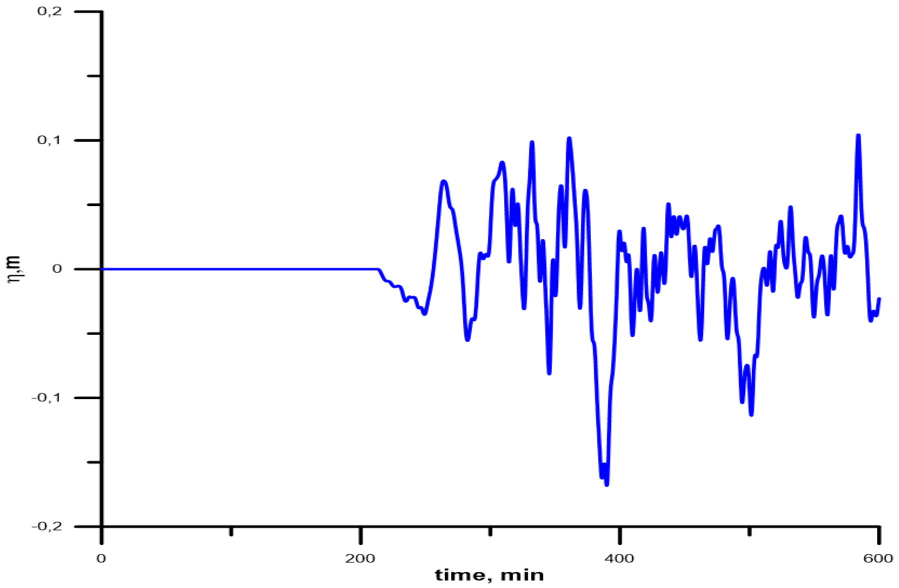

Figure 13. Computed tide gauge records of 1963 tsunami in Kholmsk (above), Nevelsk (middle), and Poronaisk (below)

Table 3. Observed and computed wave heights on Sakhalin

Coastal location	Tsunami height according to observations, m	Tsunami height according to numerical simulations, m
Katangli settlement	0,4	0,5
Poronaisk	0,3	0,6
Korsakov	0,4	0,6
Cape Krilion	0,4	0,4
Nevelsk	0,15	0,26
Kholmsk	0,1	0,3

The 1963 Urup tsunami wave heights, observed and calculated for the coastal locations of Sakhalin, are presented in Table 3 and are shown in Fig. 14. They show that the calculated wave heights are slightly higher than those observed, which can be considered a good result.

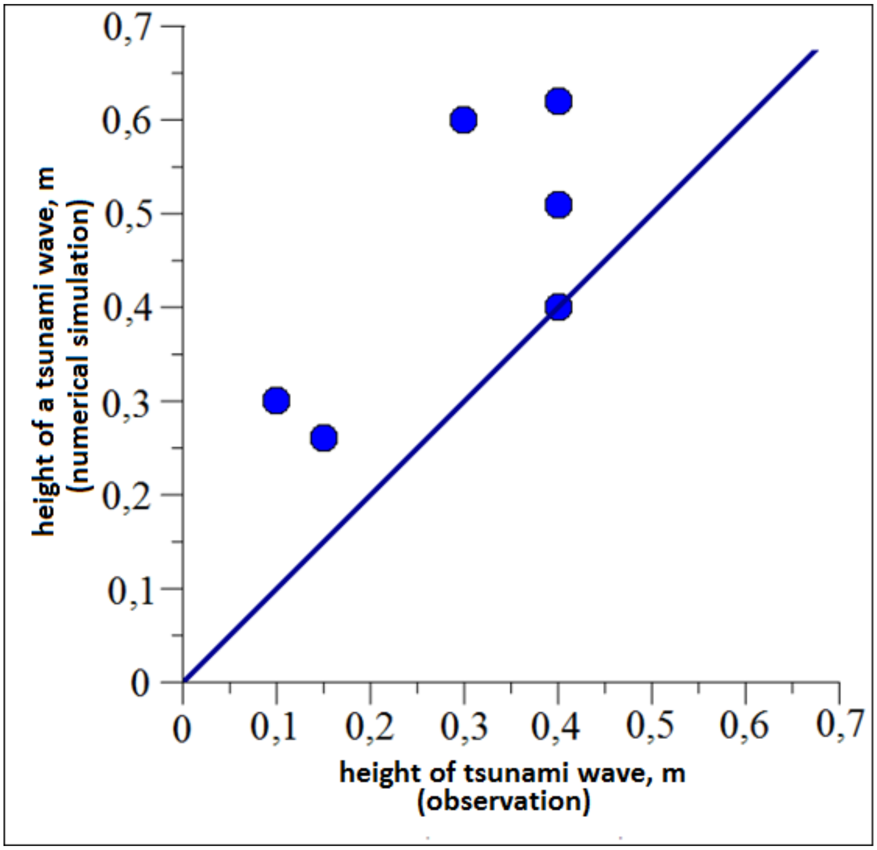

Figure 14. Comparison of the observed and computed 1963 tsunami wave heights on Sakhalin

6. CONCLUSION

About 30 tsunami events have been recorded on the island of Sakhalin, located in the Sea of Okhotsk, for the whole history of observations [Zaytsev et al, 2017]. The strongest impact on Sakhalin was made by the tsunami caused by the earthquake of October 13, 1963 at 05:17:51 GMT in the area of Urup (the Kuril Islands).The magnitude of this earthquake is 8.1 (according to some data, Mw = 8.5). Its location near the Kuril large straits Vries and Bussol contributed to a greater tsunami wave penetration into the Sea of Okhotsk, and, in particular to Sakhalin Island. The tsunami wave heights on Sakhalin did not exceed 0.4 m, while in the source they were 4-5 m high. This article summarizes tsunami instrumental observation data on Sakhalin.

Tsunami propagation numerical modeling in the framework of nonlinear shallow water theory has also been performed. The earthquake source described in [Ioki and Tanioka, 2008] was chosen. The tsunami source is calculated with the help of Okada’s solution [1985].

The computed results are verified by the observation data on the Kuril Islands. Tsunami characteristics on the Coast of Sakhalin Island are also computed. Numerical modeling allowed us to explain the observations of the 1963 Urup tsunami, confirm the chosen earthquake model, and also to estimate the tsunami heights in the places where observations were not conducted.

ACKNOWLEDGEMENTS

This study was initiated in the framework of the state task programme in the sphere of scientific activity of the Ministry of Education and Science of the Russian Federation (projects No. 5.4568.2017/6.7 and No. 5.5176.2017/8.9), grant of the President of the Russian Federation NSh-6637.2016.5 and RFBR grants 16-55-52019 and 17-05-00067.

BIBLIOGRAPHY

1. Baranova, N.A., Kurkin, A.A., Mazova, R., and Pararas-Carayannis, G. Comparative numerical simulation of the Tohoku 2011 tsunami. Science of Tsunami Hazards, 2015, vol. 34, No. 4, 212-230.
2. Dilmen, D. I., Kemec, S., Yalciner, A. C., Duzgun, S., and Zaytsev, A. Development of a tsunami inundation map in detecting tsunami risk in Gulf of Fethiye, Turkey. Pure and Applied Geophysics, 2015, vol. 172, 921-929.
3. Iida, K., D.C. Cox, and Pararas--Carayannis, G., Preliminary Catalog of Tsunamis Occurring in the Pacific Ocean. Data Report No. 5. Honolulu: Hawaii Inst. Geophys. Aug. 1967.
4. Imamura, F. Tsunami Numerical Simulation with the staggered leap-frog scheme (Numerical code of TUNAMI-N1). School of Civil Engineering, Asian Inst. Tech. and Disaster Control Research Center, Tohoku University. 1989
5. Ioki, K., and Tanioka, Y. Tsunami waveform analyses of the 1963 Kurile Islands earthquake. American Geophysical Union, Fall Meeting 2008, abstract #OS43D-1319. 2008.
6. Kaistrenko, V., Razjigaeva, N., Kharlamov, A., and Shishkin, A. Manifestation of the 2011 Great Tohoku tsunami on the coast of the Kuril Islands: A tsunami with ice. Pure and Applied Geophysics, 2013, vol. 170, 1103-1114.
7. Kostenko, I., Yalciner, A., Kurkin, A., Pelinovsky, E., and Zaytsev, A. Tsunamis in the Sea of Okhotsk: facts and modelling. Proc. Twelfth Int. Conf. on the Mediterranean Coastal Environment Medcoast -2015 (06-10 October 2015, Varna, Bulgaria). Ed. E. Ozhan. 869-880.
8. Kostenko, I.S., Kurkin, A.A., Pelinovsky, E.N., and Yalciner, A. The influence of the Kuril Islands on the penetration of tsunamis into the Sea of Okhotsk (on the example of the Japan tsunami on March 11, 2011). Izvestiya, Atmospheric and Ocean Physics, 2016, vol. 52, No. 1, 89-100.
9. Kurkin, A.A., Pelinovsky, E.N., Choi, B.H., and Lee, J.S. A comparative estimation of the tsunami hazard for the Russian coast of the Sea of Japan based on numerical simulation. Oceanology, 2004, vol. 44, No. 2, 163-172.
10. Levin, B.V., and Nosov, M.A. Physics of Tsunami. Springer, 2016
11. Okada, Y. Surface deformation due to shear and tensile faults in a half-space. Bulletin of the Seismological Society of America. 1985, vol. 75(4), 1135-1154.

12. Ozer,, C.S., Yalciner, A.C., and Zaytsev, A. Investigation of tsunami hydrodynamic parameters in inundation zones with different structural layouts. Pure and Applied Geophysics, 2015, vol. 172, 931-952.
13. Pararas-Carayannis, G., Catalog of Tsunamis in the Hawaiian Islands. World Data Center A-Tsunami U.S. Dept. of Commerce Environmental Science Service Administration Coast and Geodetic Survey, May 1969. Data Report Hawaii Inst.Geophys. Jan. 1968.
14. Pararas-Carayannis, G. The November 4, 1952 Kamchatks Earthquake and Tsunami. (Excerpts from the archives to the Catalogs of Tsunami in the Hawaiian Islands. World Data Center A- Tsunami U.S. Dept. of Commerce Environmental Science Service Administration Coast and Geodetic Survey, 1969.
15. Pararas-Carayannis, G. and Calebaugh P.J., Catalog of Tsunamis in Hawaii, Revised and Updated , World Data Center A for Solid Earth Geophysics, NOAA, 78 p., March 1977.
16. Pararas-Carayannis, G. The Earthquake and Tsunami of October 4, 1994 in the Kuril Islands (Tectonic Setting of the Northern Japan/Kuril Island Region), 1994. http://www.drgeorgepc.com/Tsunami1994RussiaKurils.html
17. Pararas-Carayannis, G. The Earthquake and Tsunami of 15 November 2006 in the Kuril Islands. 2006. http://www.drgeorgepc.com/Tsunami2006Kurils.html
18. Pelinovsky, E.N. Tsunami Wave Hydrodynamics. Institute Applied Physics Press, Nizhny Novgorod. 1996 (in Russian).
19. Schetnikov, N.A. Tsunami. Moscow: Nauka, 1981 (in Russian).
20. Schetnikov, N.A. Tsunami on the coast of Sakhalin and the Kuril Islands according to the tide gauge data of 1952-1968. – Vladivostok: FEB RAS, 1990 (in Russian).
21. Shevchenko, G.V., Ivelskaya, T.N., Kovalev, P.D., Kovalev, D.P., Kurkin, A.A., Levin, B.V., Likhacheva, O.N., Chernov, A.G., and Shishkin, A.A. New data about tsunami evidence on Russia's Pacific coast based on instrumental measurements for 2009-2010. Doklady Earth Sciences, 2011, vol. 438, No. 2, 893-898.
22. Shevchenko, G.V., Ivelskaya, T.N., and Kaistrenko, V.M. Tsunami on the Kuril Islands. Features of manifestation and measures to reduce risk. - Yuzhno-Sakhalinsk: IMGiG FEB RAS, 2012 (in Russian).
23. Shuto, N., Goto, C., and Imamura, F. Numerical simulation as a means of warning for near field tsunamis. Coastal. Engineering in Japan, 1990, vol. 33, No. 2, 173-193.
24. Solovyev, S.L. Earthquakes and tsunami on October 13 and 20, 1963 on the Kuril Islands. Yuzhno-Sakhalinsk – SakhKNII, 1965 (in Russian).
25. Solovyev, S.L. Basic data on the tsunami on the Pacific coast of the USSR, 1737-1976. In: The study of the tsunami in the open ocean. Moscow: Nauka, 1978, 61-136 (in Russian).
26. Yalciner, A.C., Pelinovsky, E., Zaytsev, A., Kurkin, A., Ozer, C., Karakus, H., and Ozyurt, G. Modeling and Visualizations of tsunamis: Mediterranean Examples. Tsunami and Nonlinear Waves // (Ed: Anjan Kundu), Springer. 2007. P. 2731-2839.
27. Yalciner, A., Zahibo, N., Insel, I., Dilmen, D.I., Zaytsev, A., Chernov, A., Ozer, C., and Pelinovsky, E. Understanding the possible effect near far field tsunamis on Lesser Antilles by numerical modelling. The Open Oceanography Journal, 2010, № 4, 50-57.

28. Zaitsev, A.I., Kovalev, D.P., Kurkin, A.A., Levin, B.W., Pelinovsky, E.N., Chernov, A.G., and Yalciner, A. The Nevelsk tsunami on August 2, 2007: Instrumental data and numerical modelling. Doklady Earth Sciences, 2008, vol. 421, No. 1, 867-870.
29. Zaitsev, A.I., Kovalev D.P., Kurkin, A.A., Levin B.V., Pelinovskii E.N., Chernov A.G., and Yalciner A. The tsunami on Sakhalin on August 2, 2007: Mareograph evidence and numerical simulation. Russian J Pacific Geology, 2009, vol. 3, No. 5, 437 – 442.
30. Zaitsev, A.I., Kurkin, A.A., Levin, B.V., Pelinovsky, E.N., Yalciner, A., Troitskaya, Yu.I., and Ermakov, S.A. Numerical simulation of catastrophic tsunami propagation in the Indian Ocean. Doklady Earth Sciences, 2005, vol. 402, No. 4, 614-618.
31. Zaytsev, A.I., Pelinovsky, E.N., Kurkin, A.A., Kostenko, I.S., and Yalciner, A. The possibility of tsunami in the Sea of Okhotsk caused by deep-focus earthquakes. Izvestiya, Atmospheric and Ocean Physics, 2016, vol. 52, No. 2, 217-224.
32. Zaytsev, A.I., Kostenko, I.S., Kurkin, A.A., and Pelinovsky, E.N. Tsunami on Sakhalin Island: observations and numerical modeling. – Yuzhno-Sakhalinsk: NNGTU, 2017. 121 p (in Russian).

ISSN 8755-6839

SCIENCE OF TSUNAMI HAZARDS

Journal of Tsunami Society International

Volume 36 Number 3 2017

COMPARISON OF METHODS FOR SIMULATING TSUNAMI RUN-UP THROUGH COASTAL FORESTS

Benazir[1], Radianta Triatmadja[2*], Adam Pamudji Rahardjo[2], and Nur Yuwono[2]

[1]Ph.D Student at Department of Civil and Environmental Engineering, Faculty of Engineering Universitas Gadjah Mada, Indonesia.
[2]Department of Civil and Environmental Engineering, Faculty of Engineering Universitas Gadjah Mada, Indonesia.
*Corresponding author: radianta@ugm.ac.id, Kompleks Yadara V/12 Babarsari Yogyakarta, Indonesia, 55281.

ABSTRACT

The research is aimed at reviewing two numerical methods for modeling the effect of coastal forest on tsunami run-up and to propose an alternative approach. Two methods for modeling the effect of coastal forest namely the Constant Roughness Model (CRM) and Equivalent Roughness Model (ERM) simulate the effect of the forest by using an artificial Manning roughness coefficient. An alternative approach that simulates each of the trees as a vertical square column is introduced. Simulations were carried out with variations of forest density and layout pattern of the trees. The numerical model was validated using an existing data series of tsunami run-up without forest protection. The study indicated that the alternative method is in good agreement with ERM method for low forest density. At higher density and when the trees were planted in a zigzag pattern, the ERM produced significantly higher run-up. For a zigzag pattern and at 50% forest densities which represents a water tight wall, both the ERM and CRM methods produced relatively high run-up which should not happen theoretically. The alternative method, on the other hand, reflected the entire tsunami. In reality, housing complex can be considered and simulated as forest with various size and layout of obstacles where the alternative approach is applicable. The alternative method is more accurate than the existing methods for simulating a coastal forest for tsunami mitigation but consumes considerably more computational time.

Keywords: modeling; long wave; vegetation; greenbelt; density; layout; dam break.

1 INTRODUCTION

Indonesia has suffered from many tsunami disasters, especially in Sumatera Island. After the destructive tsunami attacked at Aceh and Nias Island in 2004, several mitigation methods have been implemented such as the development of evacuation routes, construction of escape buildings, relocation of victim houses, and the utilization of buffer zones along the coastal areas. The buffer zone with relatively densely populated vegetation may be classified as a permeable structure prevention. Nowadays, this method is widely implemented at vulnerable tsunami regions due to its relatively low cost and ease of maintenance.

A sustainable buffer zone (coastal forest) requires suitable vegetation for tsunami prevention system. Mangrove as a natural barrier against tsunami is not suitable for sandy beaches and it grows only in the estuary area (Hiraishi & Harada, 2003). On the contrary, the *Casuarina Equisetifolia* species has been proven suitable for sandy beach type such as along Pacitan Bay in southern Java Island (Muhari, Muck, Diposaptono, & Spahn, 2012). A similar buffer zone can be found along Geureute Valley in Aceh Jaya District as shown in Figure 1. Another type of coastal vegetation is *Cocos Nucifera* (coconut palm) which is commonly grown in tropical areas.

Figure 1. Coastal vegetation at Aceh Jaya District (Source: Google Earth captured on September 29th, 2015)

The devastating tsunami power depends on the height and the surge velocity, whilst the coastal morphology affects the extent of such power on land. A mild slope beach allows the tsunami to propagate further inland and may create great damage. The land use, especially with relatively dense vegetation, has also an important role in protecting the beach against run-up and inundation. The degree of such protection depends on tsunami scale. A large scale of tsunami attack such as the Indian Ocean Tsunami 2004 at Banda Aceh, was capable of uprooting a lot of coastal vegetation resulting in further inland inundation. During Tsunami 2004 disaster, the maximum tsunami run-up was recorded at Leupung Beach, Aceh Besar District. Shibayama et al. (The December 26, 2004 Sumatra Earthquake Tsunami, Tsunami Field Survey in Banda Aceh of Indonesia, 2005) reported that the highest run-up reached 49.43 m in Ritieng Hill. This event was verified by Lavigne et al. (Reconstruction of Tsunami Inland Propagation on December 26, 2004 in Banda Aceh, Indonesia, Through Field Investigation, 2009) where their post-survey yielded 51 m at the same location. In the absence of forest protection, the tsunami could have been even more severe.

Forbes & Broadhead (The Role of Coastal Forest in the Mitigation of Tsunami Impact, 2007) mentioned that the effectiveness of tsunami mitigation offered by various types of coastal forests depends on a number of parameters including forest width, tree density, age, tree diameter, tree height, and species composition. Therefore, a quantitative evaluation of coastal forest effectiveness against tsunami, especially in term of run-up and inundation, is required for mitigation purposes. This can be done by using numerical simulation.

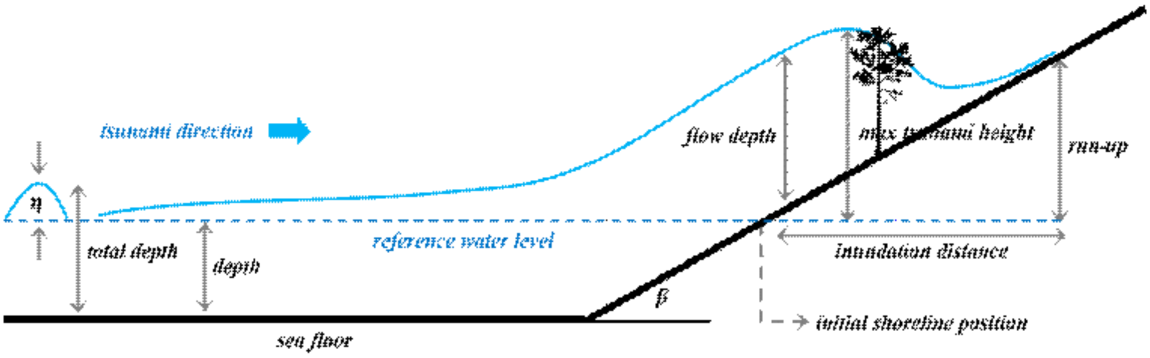

Figure 2. Sketch of tsunami run-up climbing up a sloping beach (the terminology is based on UNESCO-IOC)

Run-up is the maximum vertical elevation of a point located on initially dry land that is inundated by the waves Synolakis et al. (The Megatsunami of December 26, 2004, 2005) as illustrated in Figure 2 and is the essential parameter of tsunami hazards that directly related to inland destructions. Synolakis (The Runup of Solitary Waves, 1987) used the shallow water wave equations to solve run-up problem on a sloping beach. He derived a run-up law based on the physical model as shown in Eq. (1).

$$Rd=2.831\cot\beta Hd1.25 \qquad (1)$$

In Eq. (1), R refers to run-up, d is the undisturbed water depth, H is wave height at the shore, and β stands the slope angle. Eq. (1) may be used for a first approximation of tsunami run-up but a comprehensive run-up study involving coastal land use such as the existence of coastal forest using numerical simulation is required to determine more accurate run-up. A number of tsunami run-up against coastal forests have been carried out for example by Harada & Kawata (Study on the Effect of Coastal Forest to Tsunami Reduction, 2004) and Yanagisawa et al. (The Reduction Effects of Mangrove Forest on a Tsunami based on Field Surveys at Pakarang Cape, Thailand and Numerical Analysis, 2009). Basically, the effect of the forest was represented by using the Manning roughness coefficient. Higher roughness coefficient represents higher density of the forest. Despite their usefulness and efficiency in term of computer time, representing a forest barrier by Manning roughness coefficient seems to have a drawback. The effect of the trees layout within the forest and the effect of reflection may not be properly simulated which in turn may result in significantly different run-up patterns and height. In this paper, an alternative method of modeling coastal forest or similar barrier against tsunami run-up is proposed. The performance of the method is compared with the other existing methods i.e. CRM and ERM methods.

2 TSUNAMI PROPAGATION THROUGH A FOREST

Mathematical models based on a set of Nonlinear Shallow Water Equation (NSWE) has been widely used for tsunami simulation. A notable program that used second-order explicit leap-frog finite difference scheme to discretize a set of NSWE was developed by Goto et al. (Numerical Method of Tsunami Simulation with Leap-Frog Scheme, 1997) and Imamura et al. (Tsunami Modelling Manual (TUNAMI Model), 2006). We rewrote the program in Visual Basic .Net where some additional input-output facilities were added for convenience. The shallow water equations in Cartesian coordinate are as follows Imamura et al. (Tsunami Modelling Manual (TUNAMI Model), 2006).

$$\partial\eta\partial t+\partial M\partial x+\partial N\partial y=0 \qquad (2a)$$

$$\partial M\partial t+\partial\partial xM2D+\partial\partial yMND+gD\partial\eta\partial x+\tau x\rho=0 \qquad (2b)$$

$$\partial N\partial t+\partial\partial xMND+\partial\partial yN2D+gD\partial\eta\partial y+\tau y\rho=0 \qquad (2c)$$

$D=h+\eta$ represents the total water depth, where h stands for the still water depth and η denotes the sea surface elevation. M and N are the mass fluxes in the x and y-direction, respectively.

$$M=h\eta udz=uh+\eta=uD \qquad (3a)$$

$$N=h\eta v\square\square z \quad =vh+\eta=vD \qquad (3b)$$

Bottom friction in the x and y-direction are respectively represented by terms τx and τy, which is a function of friction coefficient f. This coefficient can be computed from Manning roughness $n0$ by the following relationship.

$$n0=fD1/32g \rightarrow f=n022gD1/3 \qquad (4)$$

Eq. (4) describes that the friction coefficient increases when the total water depth decreases. Manning roughness is usually chosen as a constant for a given condition of the land surface. The bottom friction terms are expressed by:

$$\tau x\rho=12fD2MM2+N2 \qquad (5a)$$

$$\tau y\rho=12fD2NM2+N2 \qquad (5b)$$

2.1 Constant Roughness Model

The Constant Roughness Model (CRM) which represents the effect of coastal forest based on Manning roughness coefficient ($n0$) is widely used. Aida (Numerical Experiment for Inundation of Tsunamis, 1977), Kotani et al. (Tsunami Run-up Simulation and Damage Estimation by Using GIS, 1998), and Latief & Hadi (Thematic paper: The Role of Forest and Trees in Protecting Coastal Areas against Tsunami, 2007) used Manning coefficients of 0.040, 0.030, and 0.048, respectively for the coastal forest. The variation of the above roughness coefficient suggests that the Manning coefficient representing coastal forest is site specific.

2.2 Equivalent Roughness Model

Petryk & Bosmajian (Analysis of Flow through Vegetation, 1975) introduced an important concept to present the Manning roughness form as hydraulic resistance. Based on their concept, Goto & Shuto (Effect of Large Obstacle on Tsunami Inundation, 1983) and Aburaya & Imamura (The Proposal of a Tsunami Run-up Simulation Using Combined Equivalent Roughness, 2002) developed the ERM method where the equivalent roughness (ne) can be defined by the following equation.

$$ne=D4/3CD2gdi\theta100-\theta+n02 \qquad (6)$$

where di and θ stand for the tree diameter and the percentage of the bottom area occupied by the trees in a grid on the numerical domain, respectively and CD as drag coefficient. USAC (Shore Protection Manual, 1984) stated that CD value is a function of Reynolds number (Re).

$$CD=1.2 \quad \text{if} \quad Re\leq2\times105 \qquad (7a)$$

$$CD=1.2-0.5Re3\times105-23 \quad \text{if} \quad 2\times105\leq Re\leq5\times105 \qquad (7b)$$

$$CD=0.7 \quad \text{if} \quad Re\geq5\times105 \qquad (7c)$$

FEMA (Coastal Construction Manual, 2003) suggested that the drag coefficient values should be between 1.25 and 2, depending on the ratio between the width of a model and the flow depth. Yanagisawa et al. (The Reduction Effects of Mangrove Forest on a Tsunami based on Field Surveys at Pakarang Cape, Thailand and Numerical Analysis, 2009) also defined the CD value in Eq. (6) based on their investigation among several species such as *Rhizophora sp*. and *Bruguiera sp*. Eq. (6)

accommodates both the resistance force due to the forest and the bottom friction to land use condition. The Equivalent Roughness Model (ERM) has been used by Harada & Imamura (Experimental Study on the Resistance by Mangrove under the Unsteady Flow, 2000) to model tsunami propagation through a forest. It uses the resistance of the coastal forest to represent the equivalent roughness. Besides that, Koshimura et al. (Developing Fragility Functions for Tsunami Damage Estimation Using Numerical Model and Post-Tsunami Data from Banda Aceh, Indonesia, 2009) and Muhari et al. (Examination of Three Practical Run-up Models for Assessing Tsunami Impact on Highly Populated Areas, 2011) also implemented this method to simulate tsunami through spaces between buildings at coastal area.

2.3 The Alternative Model for Tsunami Propagation through Forest

The effect of a forest on tsunami propagations is reflection over the trees' trunk and flow deceleration due to friction against the surface of the trees trunks, branches, and leaves. In the model, the trees can be represented using hypothetical columns for simulating the reflection. The effect of the friction against the surface of the trees' trunks can be represented by using the Manning roughness coefficient. Therefore, the proposed alternative method for simulating the propagation of tsunami through a forest is by using a Manning roughness coefficient as if there is no forest, but all the trees were simulated as vertical square columns. The size of the columns are equals to the size of the trees' trunk or slightly larger to accommodate the effect of the branches and leaves.

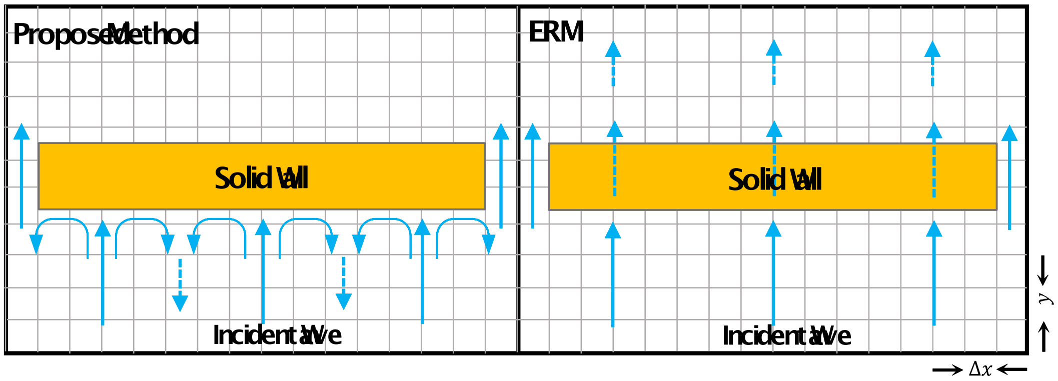

Figure 3. An extreme situation that shows the difference between the alternative method and the ERM method.

The alternative method resulted in the changes of the flow direction because of the coastal forest whereas the CRM and ERM methods reduce the flow through the coastal forest due to the use of equivalent roughness. The effect of a solid wall as illustrated in Figure 3 clearly shows the difference between the proposed alternative method and the existing methods. The figure shows that the alternative model accommodates the total reflection process without run-up downstream whilst the ERM method somehow produces run-up downstream of a solid wall.

3. RESEARCH PROCEDURE

The numerical model was applied to simulate a physical model of tsunami run-up on a 1:20 sloping beach in a flume for comparison. The flume was 15.00 m long x 0.60 m wide x 0.44 m high. The flume area was divided into two sections where the upstream part was a 4 m long reservoir (*l0)* of 0.20 m deep (*d0*) that was used as tsunami source whilst the downstream was a sloping beach model. The tsunami was generated by using a dam break system as used by Chanson (Applications of Saint-Venant Equations and Method of Characteristic to the Dam Break Wave Problem, 2005), Triatmadja & Nurhasanah (Tsunami Force on Buildings with Openings and Protection, 2012), and Triatmadja & Benazir (Simulation of Tsunami Force on Rows of Buildings In Aceh Region After Tsunami Disaster In 2004, 2014). At the downstream area, until 3 m downstream of the gate the initial depth (*d1*) was 0.10 m after which the water depth decreased due to the beach slope. Hence, the shoreline was 5 m downstream of the gate. The arrangement of the model is depicted in Figure 4.

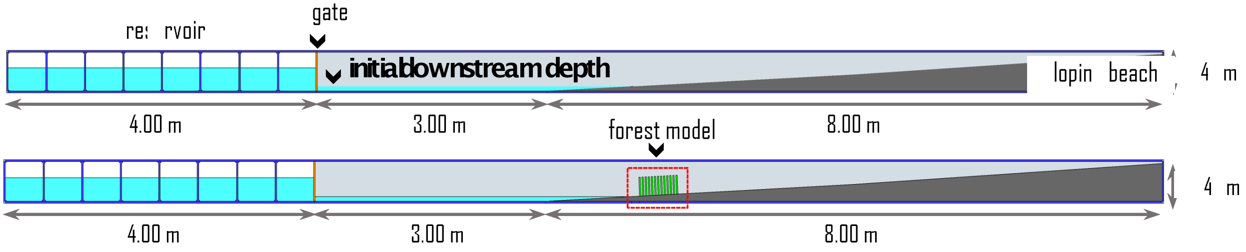

Figure 4. Arrangement of tsunami simulation

The physical model has been carried out and was reported as shown in Figure 4 in Benazir et al. (Tsunami Run-up on Sloping Beach based on Dam Break System, 2016A) and (Modeling of Tsunami Run-up onto Sloping Beach and its Interaction with Low Structure, 2016B).

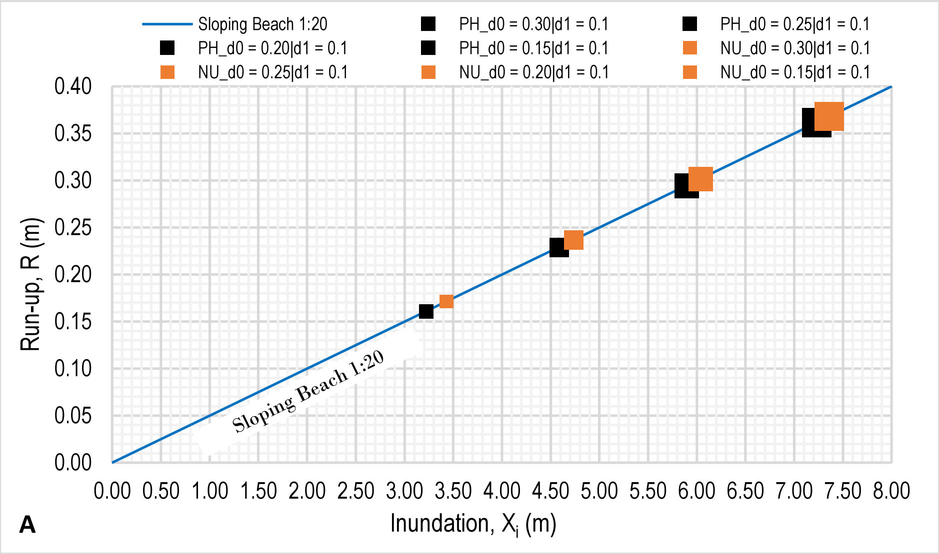

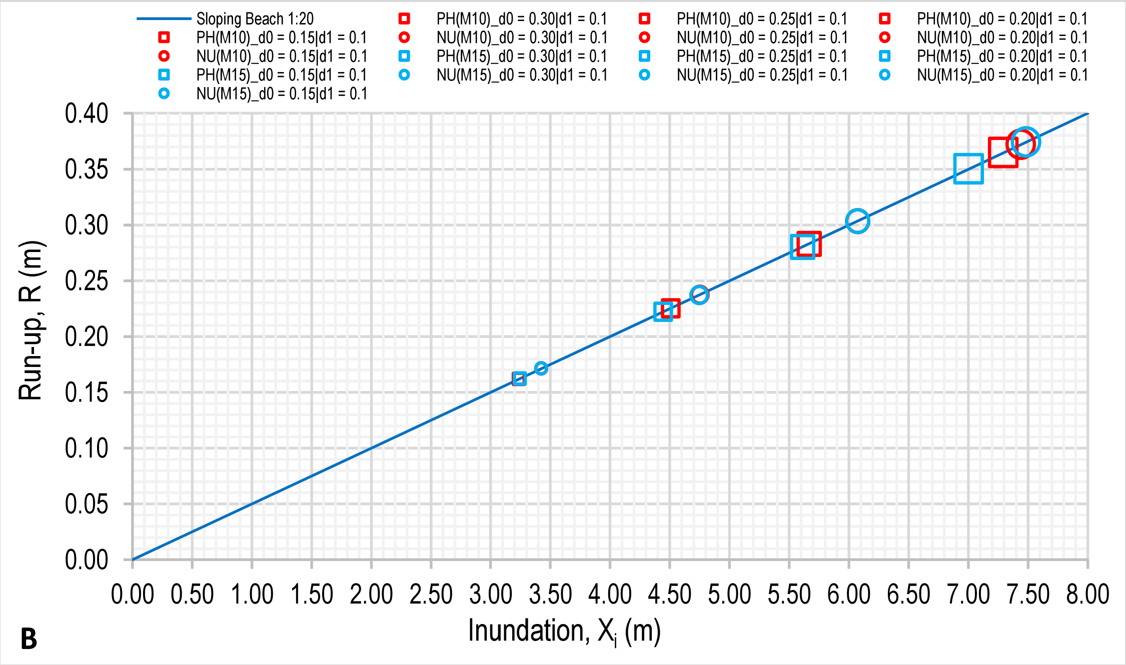

Figure 5. (A) The relation between run-up and maximum inundation and (B) the effect of the building against run-up based on the physical and numerical model. Higher *d0* and larger buildings are indicated by larger symbol (Benazir et al.(Tsunami Run-up on Sloping Beach based on Dam Break System, 2016A) and (Modeling of Tsunami Run-up onto Sloping Beach and its Interaction with Low Structure, 2016B))

These results showed that the numerical model provides fairly consistent results with the experimental data as indicated in Figure 5A. Besides that, the dimension of the square building was found to be an important factor that affected the run-up height and the distance of the inundation (Figure 5B). These findings confirmed that the numerical model results produced fairly accurate tsunami run-up with or without obstacles on a sloping beach and hence may be used with confidence to examine the tsunami run-up against the hypothetical coastal forest model.

3.1 Hypothetical Model of Coastal Forest

In order to evaluate the performance of the ERM method, CRM method and the proposed alternative method, hypothetical forests of different densities and trees layout were selected for simulations. The hypothetical forests model consisted of uniform square columns that represent the trees that were high enough and above the tsunami water surface. The dimension of the model of the tree was 0.02 m by 0.02 m. The hypothetical model layout is shown in Figure 6A. The densities of the forests depend on the total area of the trees relative to the area of the forest.

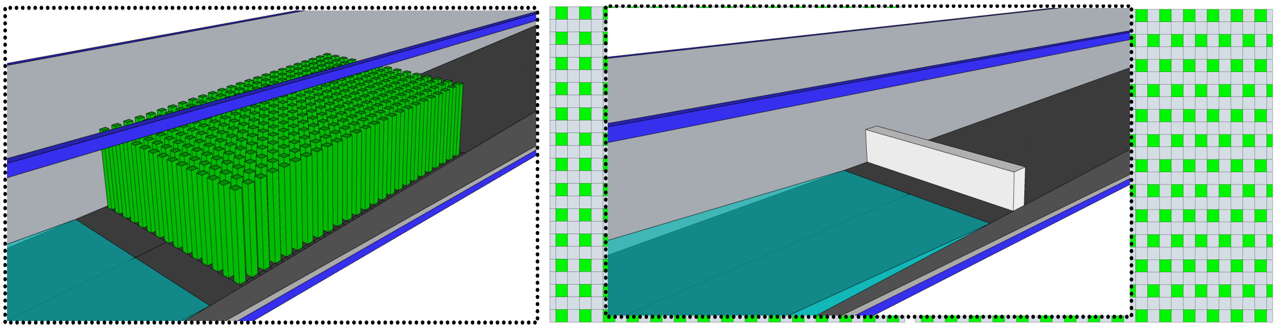

A. 3D view of Hypothetical model *B. Uniform layout* *C. Zigzag layout*

Figure 6. The hypothetical model of coastal forest and its layout variations

The parameters for the simulation were given in Table 1. During the investigation, two layout conditions were tested (Figure 6B-C). Both the uniform and the zigzag layouts have a total of 195 trees at $G=0.02$ m and 90 trees at $G=0.04$ m. The forests model front rows were at 0.10 m from the shoreline.

Table 1. The model of hypothetical coastal forest

Length (m)	Width (m)	Diameter (m)	Gap (m)	Density	Layout
0.50	0.60	0.02	0.02	25%	uniform & zigzag
0.50	0.60	0.02	0.04	11%	uniform & zigzag

4. RESULTS AND DISCUSSION

4.1 Tsunami Propagation on Sloping Beach without Forest Model

A typical tsunami heights at the shallow water region and at the land region are shown in Figure 7A. The relative tsunami height ($H/d0$) was approximately 0.22 at 1 m from the source or $Xi=-4$ m seaward from the shoreline model. Along the horizontal bottom of the flume ($Xi=-5$ m to -2 m) the tsunami height fluctuated with time as can be seen in Figure 7A. The total depth and the maximum tsunami height at certain points along the flume which occurred at different time are shown in Figure 7B. The solid line connecting each of the maximum tsunami height indicates the envelope of maximum tsunami height along the flume.

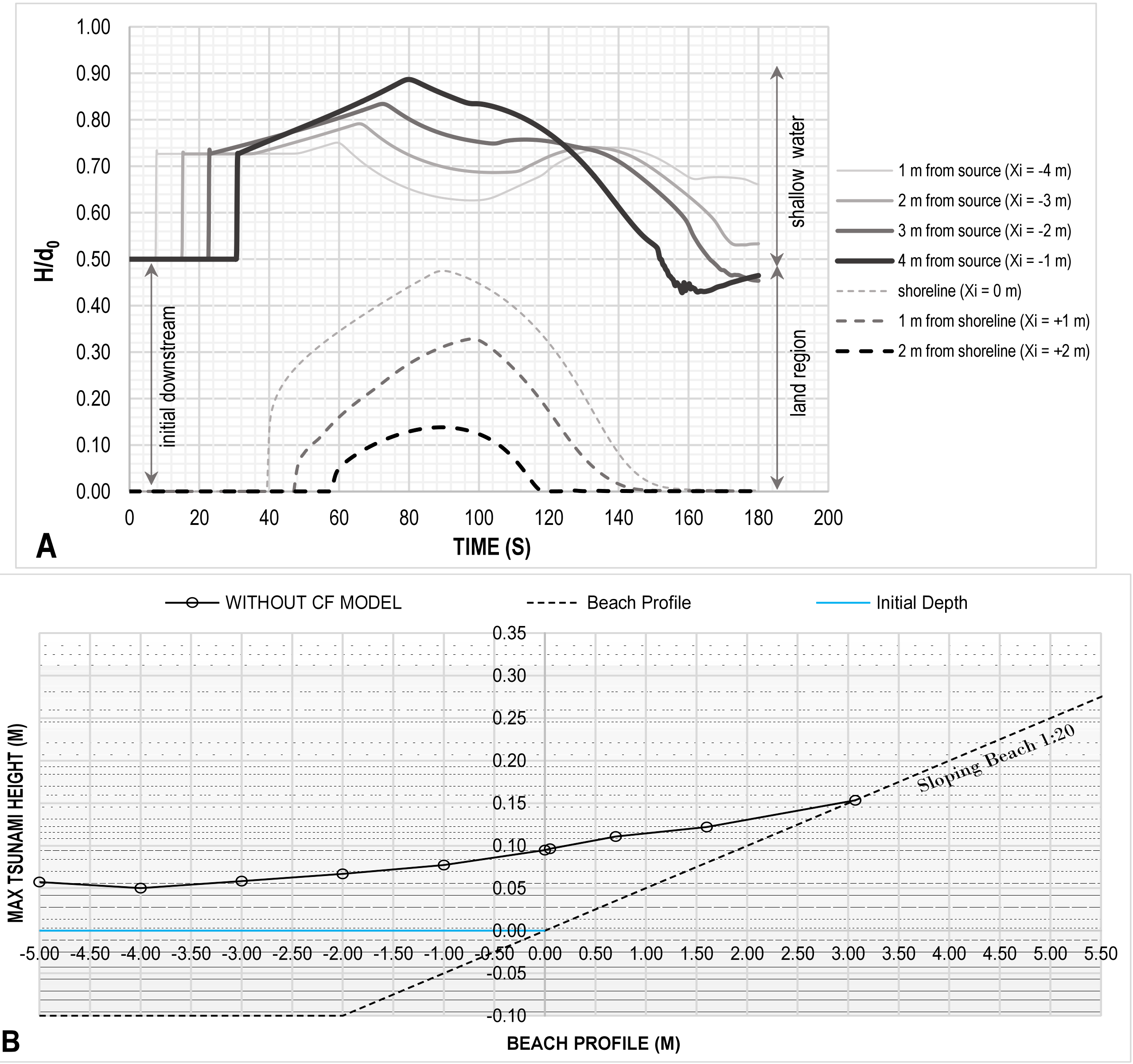

Figure 7. (A) The tsunami heights measured at various positions as a function of time and (B) the maximum tsunami height along the flume.

The performance of the methods related to the maximum run-up was tested using a variety of the reservoir depth $d0$. Figure 8 shows the corelation between the dimensionless tsunami height (H/d) and the dimensionless run-up height (R/d), where $d = 0.05$ m is the undisturb water depth at one meter distance from the shoreline model. The results match with Eq. (1), for $H/d>0.4$. This range of H/d is used for further experiment.

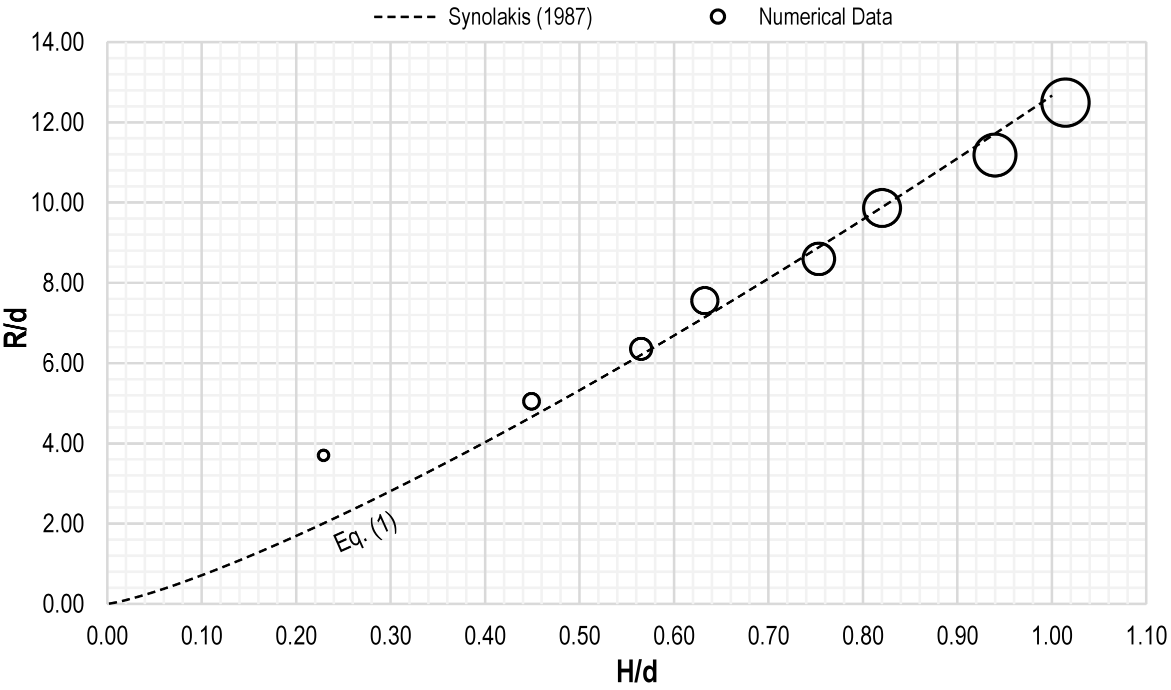

Figure 8. The relation between non-dimensional parameter R/d and H/d together with the run-up law (Eq. 1). Higher *d0* is indicated by larger symbol

4.2 The Effect of Coastal Forest on Tsunami Run-up

Forests of uniform and zigzag layouts (plantation patterns) of different densities were used to study the performance of CRM and ERM methods. The results of both methods are given in Figure 9. It is indicated in the figure that the tsunami run-ups of these models were significantly different. The ERM method produced lower run-up and hence less inundation than the CRM method. The land inundation was affected by the gap size between the trees where the smaller gap size yields lower run-up as expected. Besides that, the difference of the layouts also gives a significant effect on run-up height. Using the ERM method, the uniform layout produced higher run-up than the zigzag layout as can be seen in the figure (blue symbol). The CRM method, on the other hand, produced almost the same run-up value irrespective of the forest layout as can be seen in Figure 9.

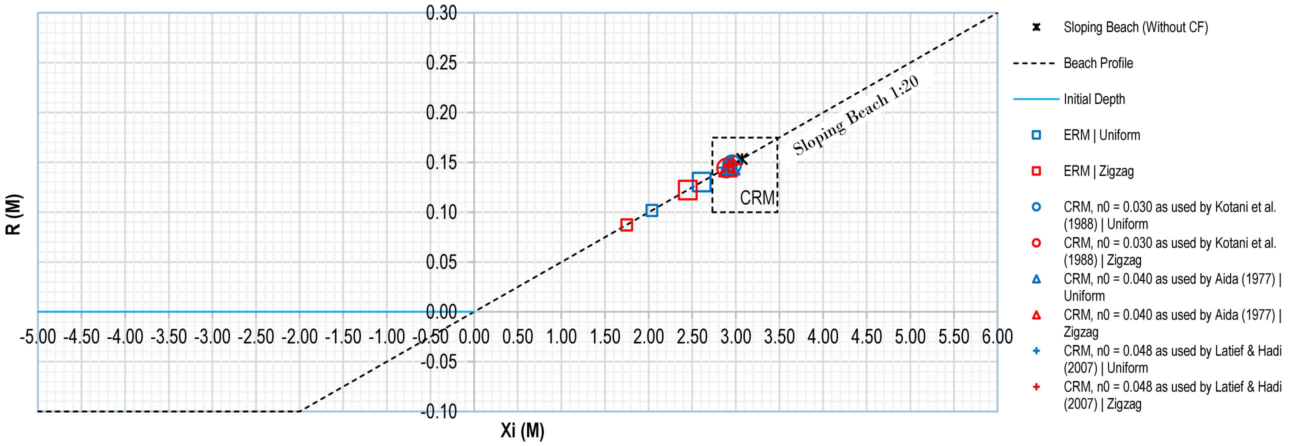

Figure 9. The run-up heights of CRM and ERM methods. Higher G is indicated by larger symbol

Theoretically, the zigzag layout may block the entire run-up path of the tsunami when there is no gap between each row of the trees. Hence, all the tsunami energy will be reflected back to the sea and no further run-up should exist behind the trees. As the gap between each row increases, the run-up behind the trees existed but at a reduced quantity. It may be concluded that in this case, the ERM is better than the CRM method in term of sensitivity against forest layout. The CRM method produced higher run-up than the ERM method for all variations of the model.

4.3 The Performance of the Alternative Method

The alternative model was tested to simulate tsunami propagation through a hypothetical coastal forest of 0.50 m long (along with the flume) and 0.60 m wide (across the flume). The tree's diameter was 0.02 m whilst the gaps were 0.02 m and 0.04 m. These models represented very dense forests which probably rarely happen. The selection of such densities was to make a clear comparison between the performances of the methods. The snapshots of the model simulation where the gap size was 0.02 m at zigzag layout are illustrated in Figure 10.

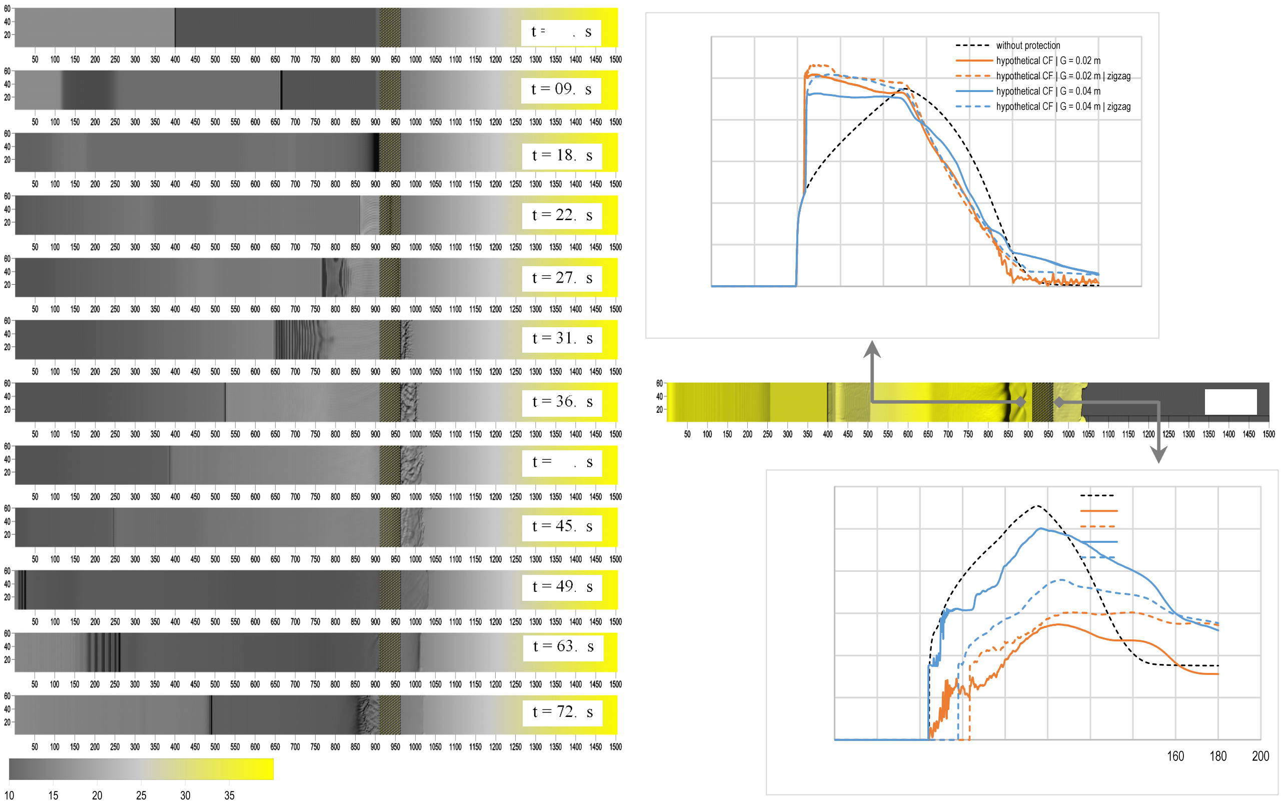

Figure 10. Snapshots of tsunami propagation along the numerical domain (left) and the water fluctuations at the upstream and the downstream of the model (right) for the case of zigzag layout with *G=0.02 m*.

The right side of Figure 10 shows that the water surface reduced over the distance of inundation incursion. Note that the water level increased in front of the forest model due to the reflection by the forest. The scale of the reflection and hence the backwater depends on the gap size and the model arrangement. It may be said that the velocity of the water at the upstream of the model decreased.

4.4 The Effect of Forest Layout against Tsunami Reduction

Figure 11 shows the tsunami water level at the maximum run-up at different layout (planting pattern) of coastal forests. In order to examine the effect of the layout, two different layouts were tested i.e. uniform and zigzag at constant gap size. The zigzag layout yields lower tsunami run-ups than the uniform layout. The reflection due to the trees plays more important role than the friction between the water and the surface trunk of the tree. Moreover, as the tsunami inundation decreased at the downstream of coastal forest, both the velocity and the energy reduced.

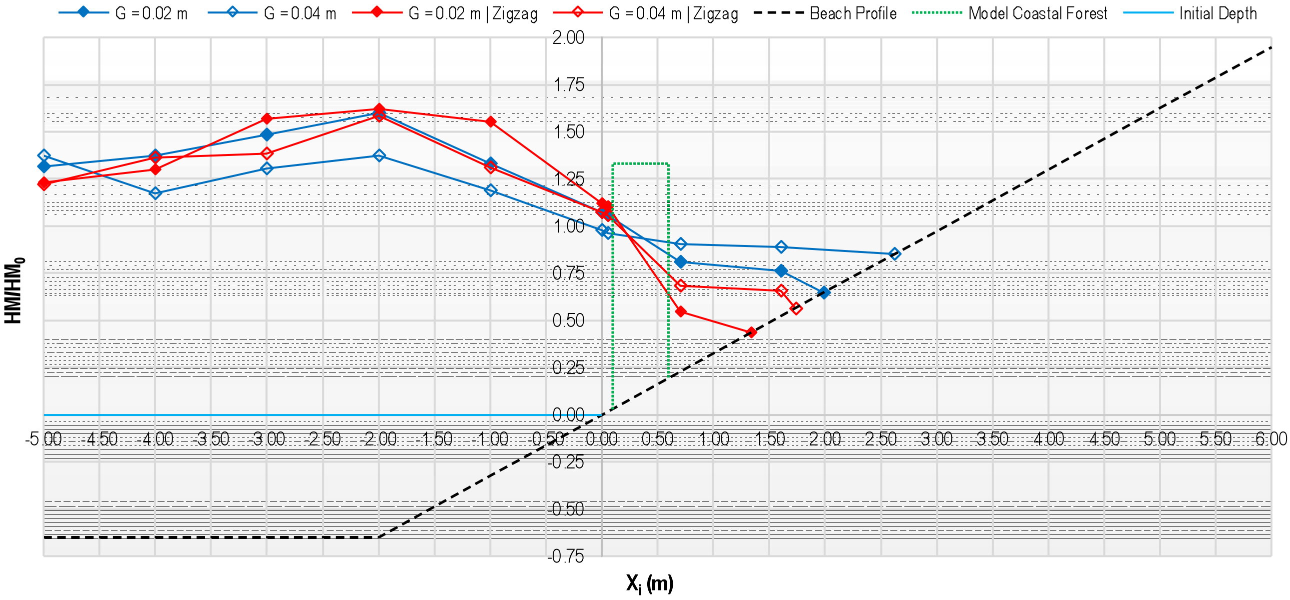

Figure 11. Distribution of maximum tsunami height near the coastline

4.5 The Effect of Forest Density against Tsunami Height

In order to examine the effectiveness of the forest density in reducing tsunami run-up, a dimensionless parameter $HMdo/HM0$ that represents the ratio between the maximum tsunami height with and without forest model, are shown in Figure 12. In this case $HMdo/HM0$ was measured at 0.10 m downstream value of Vc/V. of the forest model. In Figure 12, Vc/V represents the area of the trees relative to the total area of the forest. As Vc/V increases, $HMdo/HM0$ decreases. This means that the higher is the forest density the more effective is the forest in reducing tsunami as expected. The effectiveness of the forest density increases more significantly for zigzag layout at high high value of Vc/V.

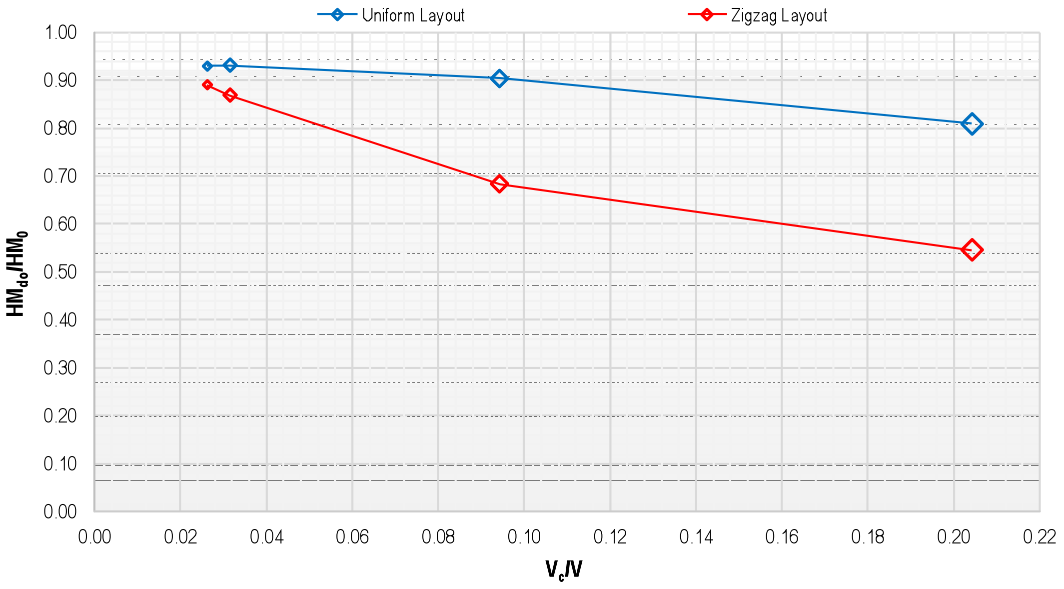

Figure 12. The effect of density variation over the maximum tsunami height behind the forest model. The higher density is indicated by larger symbol

4.6 Run-up and Inundation

The alternative method is in good agreement with the ERM method, especially for uniform layout as shown in Figure 13. The figure shows that the smaller gap size (larger forest density) produced lower run-up where more wave energy is reflected back to the sea. The alternative method resulted in lower run-up than the ERM method for the case of the zigzag layout. With the alternative method, the reflections of wave energy due to the trees were simulated better without modifying the roughness. It seems that the effect of reflection was larger than the change of roughness as simulated using ERM method as described further below.

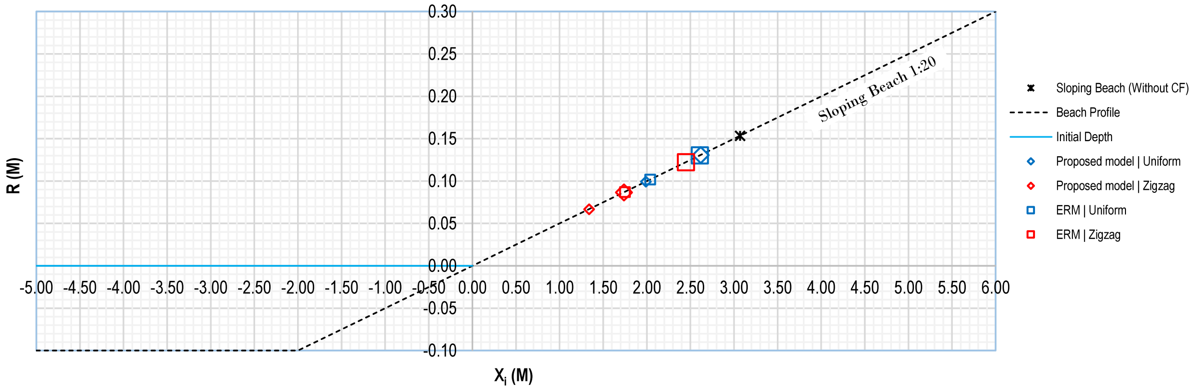

Figure 13. Tsunami run-up simulated using the alternative method and ERM method. The higher G value is indicated by larger symbol

The ERM method and the proposed method were further tested for highly dense hypothetical forest of zigzag layout. These were Case 1, Case 2, and Case 3 with 33%, 45.4%, and 50% of forest densities respectively as can be seen in Figure 14. The 50% density of forest model totally blocks the tsunami from propagating downstream as there is no space left for tsunami to flow through.

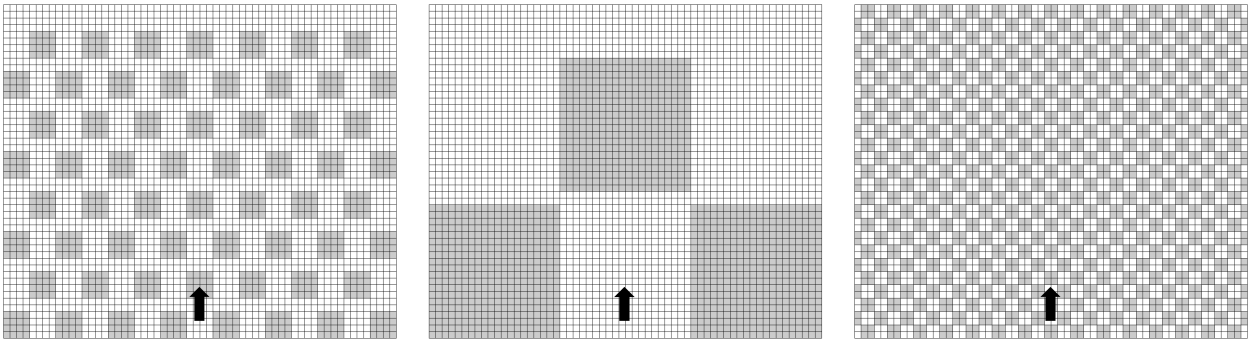

A. Zigzag Te. 1 B Zigzag Te. 2 C. Zigzag Te. 3

Figure 14. The layout of zigzag models. The arrows indicate the direction of tsunami

The result of the simulation using the ERM method indicated that the tsunami run-up through the forest of Case 1 was still relatively high as shown in Figure 15. Even with the hypothetical forest of 50% density and layout that totally blocked the space, the run-up was still relatively high. The alternative method yields more realistic result for 50% forest densities of the zigzag layout. Theoretically, such a forest represents a solid wall that is water tight. While the alternative method reflects the entire tsunami back to the sea (no run-up), the ERM method allowed for tsunami to flow through the forest and even run-up on the beach. Hence, it may be said that the alternative method performs better than both CRM and ERM methods. The drawback of the alternative method, however, is clearly the much longer computational time as smaller grids should be employed for the computation. The ERM method can be used in much larger cell grids since it requires only the bottom roughness of land use information, and the percentage of forest occupancy (see Muhari, et al. (Examination of Three Practical Run-up Models for Assessing Tsunami Impact on Highly Populated Areas, 2011)).

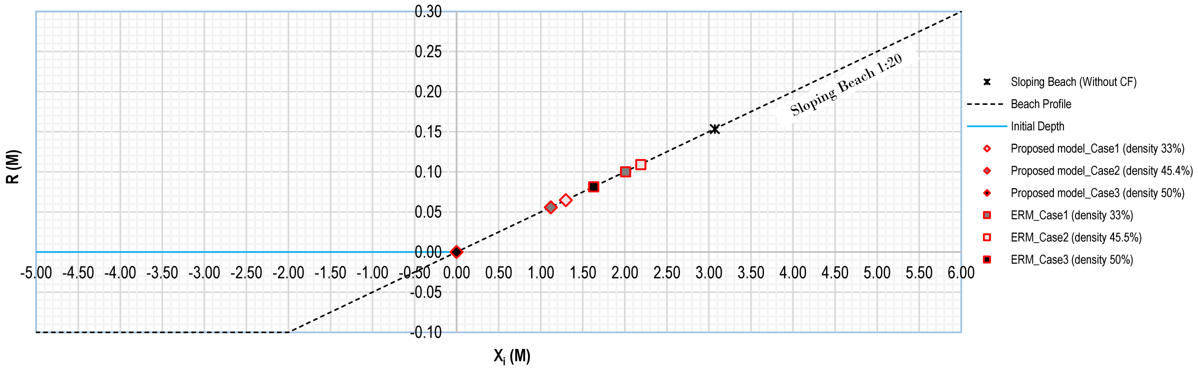

Figure 15. The relation of run-up against inundation for the zigzag case with different density

4.7 The Influence of Grid Size in Tsunami Simulation including Coastal Forest

Realizing the importance of certain variables namely gap size (G), grid size (Δx), tree diameter (D), run-up with coastal forest (R), and run-up without forest model ($R0$), a dimensional analysis was performed to group the variables into dimensionless parameters as can be seen in Figure 16. Based on the figure, it may be concluded that the performance of the alternative method depends on the ratio of grid size and the model size. A smaller grid size produces better result. However, Figure 16 indicates that the difference between run-up was less than 3% even after refinement of $\Delta x2DG$ from 1.0 to 0.01 where $\Delta x \leq D$.

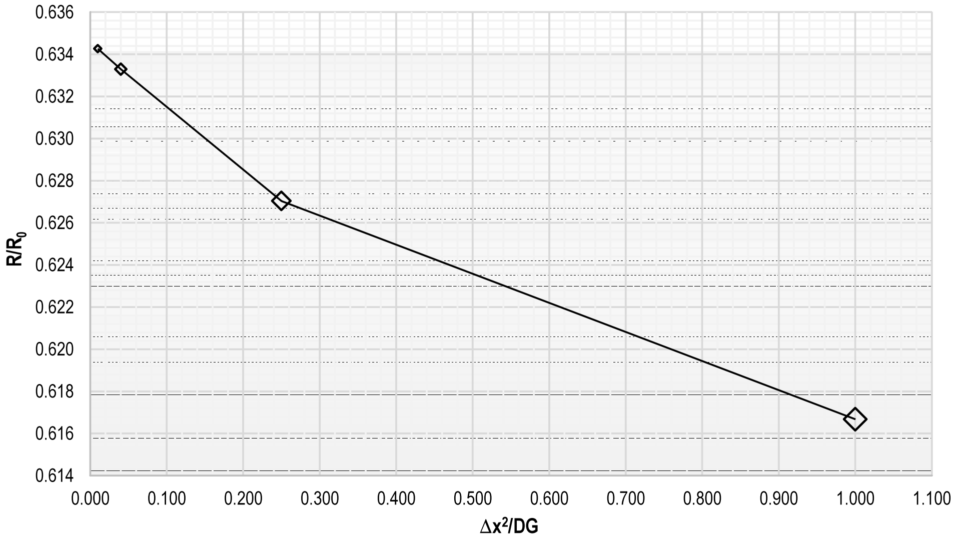

Figure 16. Correlation between the grid sizes in generating tsunami run-up based on the alternative method. The larger Δx is indicated by larger symbol

5. CONCLUSION AND RECOMMENDATION

The ERM method is better than the CRM method where the ERM somehow accommodates for different types of forest layout. The alternative method is more accurate than both the CRM and ERM methods when simulating tsunami run-up through the highly dense coastal forest. Even with moderately high density (11%), the difference between the alternative method and the ERM is significant, where the alternative method produced lower tsunami run-up. At much lower density, however, the ERM and the proposed method are expected to produce a very similar result. The alternative method is more time to consume, however, with the advancement of technology, it is hoped that in the future such alternative method will be more applicable. For relatively low forest density the ERM method is recommended.

ACKNOWLEDGEMENT

The research was fully funded by Lembaga Pengelolaan Dana Pendidikan (LPDP) Kementerian Keuangan Republik Indonesia via Scholarship of Indonesia Education (BPI). We would like to express our sincere gratitude for the funding.

REFERENCES

Aburaya, T., & Imamura, F. (2002). The Proposal of a Tsunami Run-up Simulation Using Combined Equivalent Roughness. *Annual Journal of Coastal Engineering (JSCE) , 49*, 276-280.

Aida, I. (1977). Numerical Experiment for Inundation of Tsunamis. *Bulletin of Earthquake Research Institute, University of Tokyo , 52*, 441-460.

Benazir, Triatmadja, R., Rahardjo, A. P., & Yuwono, N. (2016B). Modeling of Tsunami Run-up onto Sloping Beach and its Interaction with Low Structure. *The 4th International Conference on Sustainable Built Environment (ICSBE), 12-14 October 2016* (pp. 622-630). Yogyakarta: The 4th International Conference on Sustainable Built Environment (ICSBE), 12-14 October 2016.

Benazir, Triatmadja, R., Rahardjo, A. P., & Yuwono, N. (2016A). Tsunami Run-up on Sloping Beach based on Dam Break System. *The 5th International Seminar of HATHI, 29-31 July 2016* (pp. 565-574). Bali: The 5th International Seminar of HATHI, 29-31 July 2016.

Chanson, H. (2005). *Applications of Saint-Venant Equations and Method of Characteristic to the Dam Break Wave Problem.* Brisbane, Australia: Report CH55/05, Departement of Civil Engineering The University of Queensland.

FEMA. (2003). *Coastal Construction Manual* (Third ed.). Federal Emergency Management Agency (FEMA 55).

Forbes, K., & Broadhead, J. (2007). *The Role of Coastal Forest in the Mitigation of Tsunami Impact.* Bangkok: Food and Agriculture Organization of the United Nations.

Goto, C., & Shuto, N. (1983). Effect of Large Obstacle on Tsunami Inundation. In K. Iida, & T. Iwasaki (Eds.), *Tsunami - Their Science and Engineering* (pp. 511-525). Tokyo: Terra Scientific Publishing Company.

Goto, C., Ogawa, Y., Shuto, N., & Imamura, F. (1997). *Numerical Method of Tsunami Simulation with Leap-Frog Scheme.* IOC Manual: IUGG/IOC Time Project, UNESCO.

Harada, K., & Imamura, F. (2000). Experimental Study on the Resistance by Mangrove under the Unsteady Flow. (pp. 975-984). Proceeding of the 1st Congress of APACE.

Harada, K., & Kawata, Y. (2004). Study on the Effect of Coastal Forest to Tsunami Reduction. *Annuals of Disas. Prev. Res. Inst., Kyoto Univ.* (47C).

Hiraishi, T., & Harada, K. (2003). Greenbelt Tsunami Prevention in South-Pacific Region. *Report of the Port and Airport Research Institute , 42* (2).

Imamura, F., Yalciner, A. C., & Ozyurt, G. (2006). *Tsunami Modelling Manual (TUNAMI Model).* Sendai, Japan: Disaster Control Research Center, Tohoku University.

Koshimura, S., Oie, T., Yanagisawa, H., & Imamura, F. (2009). Developing Fragility Functions for Tsunami Damage Estimation Using Numerical Model and Post-Tsunami Data from Banda Aceh, Indonesia. *Coastal Engineering Journal , 51*, 243-273.

Kotani, M., Imamura, F., & Shuto, N. (1998). Tsunami Run-up Simulation and Damage Estimation by Using GIS. *Proc. of Coastal Eng., JSCE , 45* (1), 356-360.

Latief, H., & Hadi, S. (2007). Thematic paper: The Role of Forest and Trees in Protecting Coastal Areas against Tsunami. In *Coastal Protection in the aftermath of the Indian Ocean Tsunami. What role for forests and trees?* (pp. 5-35). Bangkok: Proceedings of the Regional Technical Workshop, FAO.

Lavigne, F., Paris, R., Grancher, D., Wassmer, P., Brunstein, D., Vautier, F., et al. (2009). Reconstruction of Tsunami Inland Propagation on December 26, 2004 in Banda Aceh, Indonesia, Through Field Investigation. *Pure and Applied Geophysics , 166*, 259-281.

Muhari, A., Imamura, F., Koshimura, S., & Post, J. (2011). Examination of Three Practical Run-up Models for Assessing Tsunami Impact on Highly Populated Areas. *Nat. Hazards Earth Syst. Sci. , 11*, 3107-3123.

Muhari, A., Muck, M., Diposaptono, S., & Spahn, H. (2012). Tsunami Mitigation Planning in Pacitan, Indonesia: A Review of Existing Effort and Ways Ahead. *Science of Tsunami Hazard , 11*, 244-267.

Petryk, S., & Bosmajian, G. (1975). Analysis of Flow through Vegetation. *Journal of Hydraulics Division , 101* (HY7), 871-884.

Shibayama, T., Okayasu, A., Sasaki, J., Suzuki, T., Matsumaru, Masimin, et al. (2005). *The December 26, 2004 Sumatra Earthquake Tsunami, Tsunami Field Survey in Banda Aceh of Indonesia.* Retrieved November 25, 2015, from http://www.cvg.ynu.ac.jp/G2/indonesia_survey_ynu_e.html

Synolakis, C. E. (1987). The Runup of Solitary Waves. *Journal of Fluid Mechanics , 185*, 523-545.

Synolakis, C., Okal, E., & Bernard, E. (2005). The Megatsunami of December 26, 2004. *The Bridge , 35 No. 2*, 26-35.

Triatmadja, R., & Benazir. (2014). Simulation of Tsunami Force on Rows of Buildings In Aceh Region After Tsunami Disaster In 2004. *Science of Tsunami Hazard , 33 No. 3*, 156-169.

Triatmadja, R., & Nurhasanah, A. (2012). Tsunami Force on Buildings with Openings and Protection. *Journal of Earthquake and Tsunami , 6 No. 4*, 1-17.

USAC. (1984). *Shore Protection Manual.* Vicksburg, Mississippi, US: Coastal Engineering Research Center.

Yanagisawa, H., Koshimura, S., Goto, K., Miyagi, T., Imamura, F., Ruangrassamee, A., et al. (2009). The Reduction Effects of Mangrove Forest on a Tsunami based on Field Surveys at Pakarang Cape, Thailand and Numerical Analysis. *Coastal and Shelf Science , 81*, 27-37.

ISSN 8755-6839

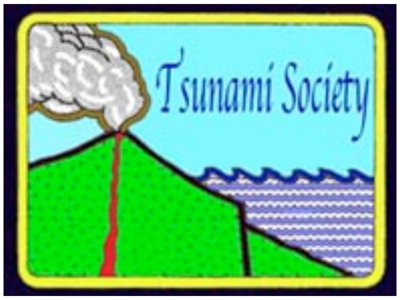

SCIENCE OF TSUNAMI HAZARDS

Journal of Tsunami Society International

Volume 36 Number 3 2017

TSUNAMI SOCIETY INTERNATIONAL, 1741 Ala Moana Blvd. #70, Honolulu, HI 96815, USA.

WWW.TSUNAMISOCIETY.ORG